DISSERTATION

DEVELOPMENT OF NOVEL MECHANICAL DIAGNOSTIC TECHNIQUES FOR EARLY PREDICTION OF BONE FRACTURE HEALING OUTCOME

Submitted by

Jakob G. Wolynski

School of Biomedical Engineering

In partial fulfillment of the requirements

For the Degree of Doctor of Philosophy

Colorado State University

Fort Collins, Colorado

Fall 2021

Doctoral Committee:

Advisor: Kirk McGilvray
Co-Advisor: Christian Puttlitz

Paul Heyliger
Susan James
Zhijie Wang

ABSTRACT

DEVELOPMENT OF NOVEL MECHANICAL DIAGNOSTIC TECHNIQUES FOR EARLY PREDICTION OF BONE FRACTURE HEALING OUTCOME

Failed bone fracture healing (nonunion) occurs in a small, but non-trivial, percentage of patients. Nonunions result in substantial morbidities to patients including increased pain, elevated medical expenditures, hindered return of normal limb function, delayed return to work, and increased use of prescription opioids. Early prediction of adverse fracture healing is vital for advising the application of early secondary intervention and advanced treatment techniques to rectify the course of healing and improve patient outcome. Despite this, diagnosis of a nonunion often requires upwards of six months post-fracture due to the lack of specificity of current clinical technologies for monitoring fracture healing, namely x-ray imaging.

The primary limitation of x-ray imaging is the dependence on calcified tissue formation to provide visual indications of fracture healing progression. However, the onset of tissue calcification is frequently delayed and does not ultimately indicate that proper fracture stabilization will occur. Novel diagnostic strategies are emerging which utilize mechanical methods to capture changes occurring at the healing fracture site prior to fracture site mineralization. The temporal progression of mechanical stiffness at the fracture site is quantifiably different for fractures trending towards nonunion versus proper union during the acute stages of healing (< 30 days). While monitoring the mechanics of the fracture provides a means to expedite the prediction of healing outcome,

quantification of fracture stiffness is technically difficult and typically requires invasive measurement techniques (i.e., transdermal wired gages).

Therefore, the comprehensive goal of this work is to develop a novel noninvasive technology to predict the healing outcome of long bone fractures using mechanical methods. Explicitly, the specific aims of this study are (1) develop a noninvasive technology which indirectly quantifies relative fracture stiffness of bone fractures treated with orthopaedic plating, (2) evaluate the efficacy of the technology developed in Specific Aim 1 in a translational comparative animal model, and (3) assess the potential for the technology developed in Specific Aims 1 & 2 to predict fracture healing outcome in clinically common fracture types using parametric finite element analysis.

This body of work reflects the inherent need for iterative technological development when producing new and complex diagnostic tools. Initial efforts developed a telemetric resonator strain gage for noninvasive measurements of implant surface strains as an indirect measurement of fracture callus stiffness, which performed satisfactorily in Specific Aim 1 but failed Specific Aim 2. Subsequent technologic redevelopment produced a coiled coaxial dipole antenna system which direct electromagnetically couples (DEC) to metallic orthopaedic implants to noninvasively measure their deflections during mechanical loading to quantify stiffness of the bone-implant construct. The initial coiled coaxial dipole antenna design demonstrated successful accomplishment of Specific Aim 1 and Specific Aim 2, but elucidated the need for miniaturized DEC antenna designs to enable methods for converting DEC data directly into measures of fracture

stiffness. To this end, an improved miniaturized Vivaldi antenna design was developed and demonstrated improved efficacy as a means to noninvasively quantify healing induced changes in fracture stiffness (Specific Aim 1).

While translational ovine fracture healing models exhibited success as a means to assess the clinical viability of the developed diagnostic technologies *in vivo* (Specific Aim 2), rigorous testing of the innumerable permutations of fracture and treatment type were neither feasible nor ethical. To this end, parametric finite element analyses were performed to directly model the pertinent biomechanics of 96 permutations of fracture and treatment type, each modeled through 17 stages of fracture healing. These *in silico* models advised the clinical scenarios best suited to DEC diagnostic measurements and further validated the theories foundational to DEC as a diagnostic predictor of bone fracture healing outcome.

The specific aims of this body of work holistically served to guide the development of a novel diagnostic technology to fundamentally improve the treatment of bone fracture healing. Research following these aims resulted in 4 full-length peer reviewed journal publications (2 remain in review at the time of writing this dissertation) and 1 U.S. patent. This dissertation details the iterative development, and rigorous testing, of three total technologies for this purpose. The diagnostic device and methodologies ultimately produced by this body of work demonstrate great promise as a clinical tool for noninvasive quantification of healing fracture stiffness, thus enabling expedited prediction of adverse fracture healing. While appreciable work remains prior to clinical

implementation, this body of work has produced technology which may enable clinicians to improve bone fracture healing outcome and reduce patient suffering.

ACKNOWLEDGMEMENTS

I sincerely thank Dr. Jeremiah Easley, Dr. Holly Stewart, Katie Bisazza, Cat Hersh, Lisa Mangin, Erin McCready, Meaghan Monahan, & Izzy Olaes for their considerable contributions to conducting *in vivo* biomechanics studies.

Thank you to Dr. Milan Ilić, Dr. Kevin Labus, & Dr. Branislav Notaroš for their collaboration and contributions to the development of the electromagnetic devices central to this body of work.

DEDICATION

This collective body of work is dedicated to Hannah Mikelson, Lisa Hanson, Arlo Hanson, Glenn Wolynski & Jordan Wolynski. All that I have, and all that I have done, would not be possible without your continued love, support, sacrifice, & patience.

TABLE OF CONTENTS

CHAPTER 1: BACKGROUND

1.1 Significance

Bone fracture annual incidence rates in the United States are estimated to be 4,017 per 100,000 individuals, representing approximately 13 million people per year [1]. While many bone fractures achieve proper union, an appreciable population experiences adverse healing in the form of delayed union or nonunion. Incidence rates of nonunions vary by fracture type [2], location [3, 4], trauma severity [5, 6], treatment type [3], and patient comorbidities [4, 6-8]. These numerous influencers on bone healing outcomes contribute to the high variability in reported incidence rates of nonunions [3, 9]. Interestingly, rates are reportedly highest in long bones, specifically in the lower leg where over 9% of fractures fail to heal properly [10].

While the factors contributing to failed fracture healing are poorly understood, the resultant negative impact on patients is well documented. Nonunion has been shown to cause the need for additional orthopaedic surgeries, increased inpatient care, extended use of prescription opioid drugs, increased strength of opioid use [11], worsened mental health, and long term pain and disability [6, 12]. Adverse fracture healing results in inflation to medical costs [4, 9, 11, 13, 14], with median direct care costs increasing by 118% [11] and additional costs being associated with a delayed return to work [9].

Early intervention treatment of nonunions offers the potential to reduce patient suffering and medical expenditures [9, 15]; however, this necessitates early and accurate prediction of nonunion

in order to determine the appropriate level of care. Despite this, clinical diagnosis of nonunion remains a slow process, with diagnosis occurring 6.2 months post fracture, on average [16]. The current work thus aims to develop a novel, clinically viable, diagnostic tool for early prediction of fracture healing outcome.

1.2 Fracture Healing Pathways

Bone is a relatively unique tissue due to its ability to self-repair without the formation of chronic scar tissues. The fracture healing process can be generally described as consisting of three overlapping phases of inflammation, repair, and remodeling (Figure 1.1) [17, 18]. The inflammatory phase begins at bone fracture, which ruptures blood vessels thus inducing inflammatory physiological cascades ultimately resulting in hematoma formation at the fracture site [17, 19]. The hematoma functions to provide initial mechanical support to the fracture site in addition to providing the initial spatial framework for future repair by chondrocytes and osteoblasts. Following the inflammatory phase, bone repair occurs through intramembranous ossification and/or endochondral ossification.

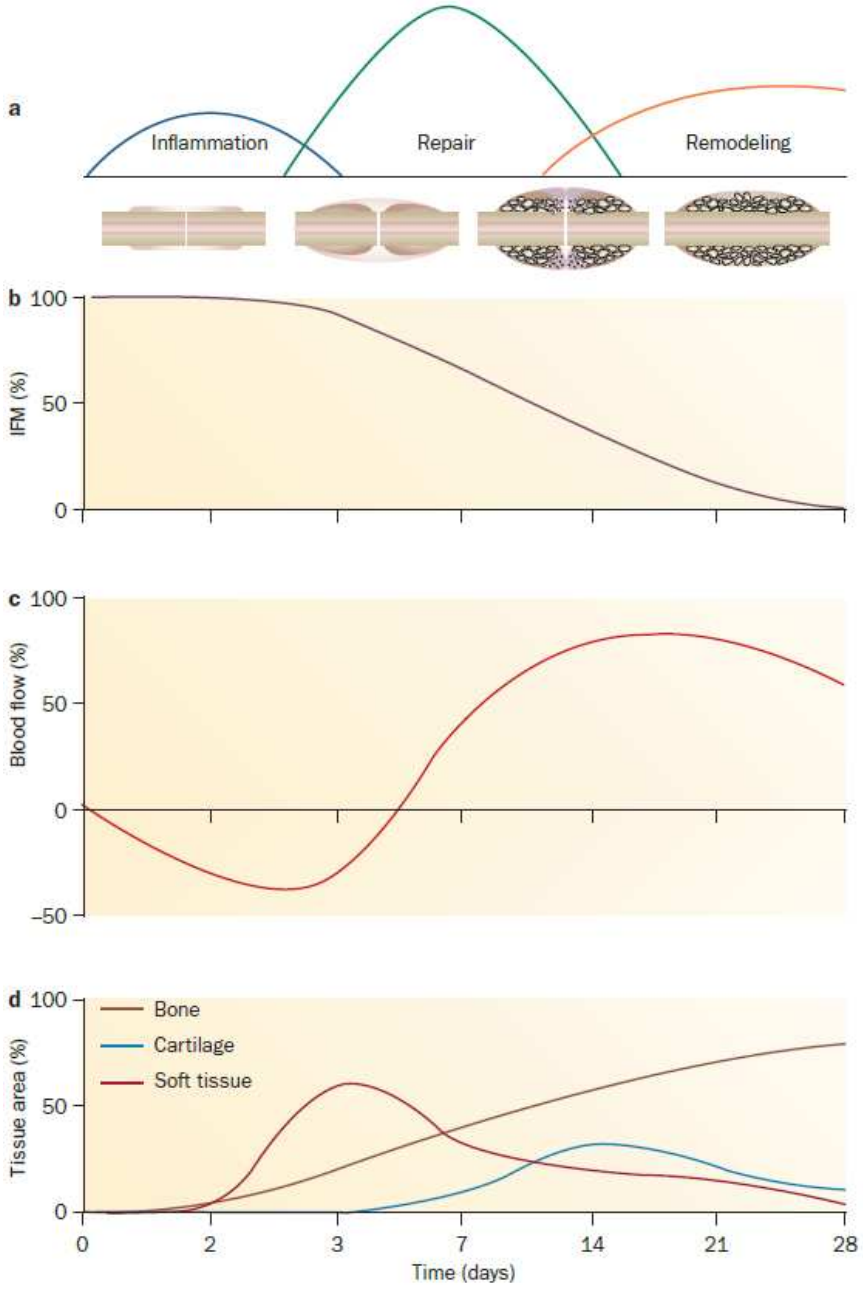

Figure 1.1: Time course of fracture healing for a rat fracture model. A) Fracture healing can be divided into three overlapping phases which begin at initial fracture and can last until many months or even years until bone is ultimately remodeled to its original form. B) Interfragmentary motion of the bone fracture segments reduces as fracture site mechanical integrity is restored over the course of proper bone fracture healing. C) Blood flow to the fracture site is reduced during the initial inflammatory phase, but increases throughout fracture repair. D) Tissue composition at the fracture site varies throughout the healing process (endochondral ossification is shown), and characteristically involves initial formation of a soft tissue callus which is subsequently converted to cartilage and finally bone in the later stages of healing. (Reprinted by permission from Springer Nature Customer Service Centre GmbH: Springer Nature, Nature Reviews Rheumatology, [17] Claes et al., 2012).

Intramembranous ossification, also known as primary bone formation, tends to occur in rigidly stabilized fractures with full or compressed reduction [20], resulting in small strains [21] and minimal interfragmentary motion at the fracture site [17]. Primary bone formation involves the direct formation of woven bone by osteoblasts to bridge the fracture gap. Thus, a hard callus is directly formed at the fracture site without the formation of an intermediate soft callus.

Endochondral ossification, also known as secondary bone formation, takes place in instances of less stable fracture stabilization [20] when the fracture site is subjected to increased levels of strain [21] or interfragmentary motion [17]. Endochondral ossification is characterized by the formation of an intermediate soft callus composed of cartilaginous and granular tissues. The soft callus is ultimately calcified then resorbed [22] after bridging of the fracture gap causes sufficient reduction in interfragmentary motion [17] (Figure 1.1).

Bone remodeling follows the repair phase of fracture healing. During this phase periosteal hard callus is removed and woven bone is replaced by lamellar bone to produce a continuous cortical structure resembling that of the bone prior to fracture. This process typically takes place over the course of several years after clinical fracture union has occurred [17].

1.3 Nonunions

Nonunions represent failed fracture healing and are loosely defined as cessation of biological healing at the fracture site prior to bone bridging the fracture gap [23]. While diagnosis typically involves the use of radiographic imaging, there is little consensus among orthopaedic surgeons

regarding exact criteria for diagnosing nonunion [24]. For example, in a survey of over 400 orthopaedic surgeons the reported time required to diagnose nonunion ranged between 2 and 12 months [16]. Some of this diagnostic difficulty can be attributed to the possibility of delayed fracture healing, known as delayed union, leading to hesitation in application of invasive secondary treatment methods for facilitating proper union. These difficulties are further exacerbated by inherent differences in the time required for healing of different fracture types [24].

1.3.1 Categories of Nonunions

Nonunions can be classified according to their radiographic appearance, and generally fall into one of four categories: hypertrophic nonunion, atrophic nonunion, oligotrophic nonunion, or septic nonunion (Figure 1.2) [25]. Hypertrophic cases are indicative of sufficient blood supply but poor mechanical stability and are typically characterized by large radiographic appearance of callus without bone bridging the fracture cortices. Atrophic cases present with the opposite radiographic appearance, with little to no callus formation. These cases generally indicate one or more of the following issues: inadequate blood flow, poor biological response, or inadequate fracture fixation. Oligotrophic nonunions represent aspects of both of the previous categories and present radiographically by a partial, but incomplete, fracture callus. This pattern is indicative of adequate biological factors for healing, but insufficient fracture reduction. Septic nonunions occur in cases where the fracture site becomes infected [15, 25-27].

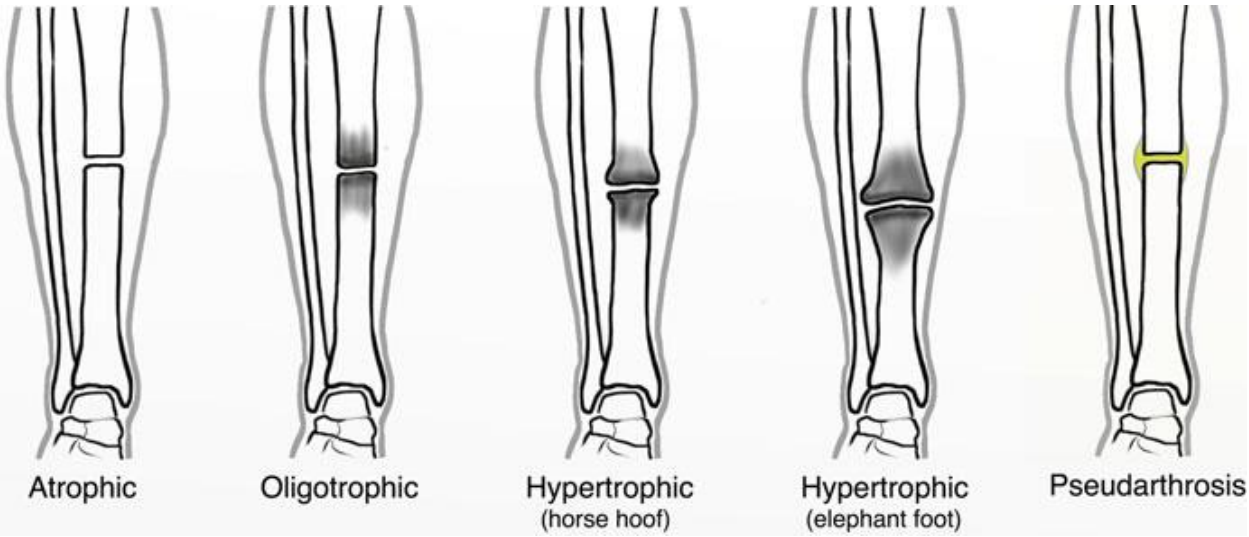

Figure 1.2: Graphical representation of the radiographic appearance of nonunions. Atrophic nonunions are indicative of insufficient biological activity or blood flow, hypertrophic nonunions indicate insufficient mechanical stability at the fracture site, and oligotrophic nonunions are an intermediate combination of deficiency in biological and mechanical environment. Pseudarthrosis represents a form of hypertrophic nonunion in which fluid becomes trapped within the cartilaginous soft callus. (Reprinted by permission from Springer Nature Customer Service Centre GmbH: Springer Nature, Trauma and Orthopaedic Classifications: A Comprehensive Overview (Chapter 119) by [25] Giannoudis & Kanakaris, 2015).

1.3.2 Causes of Nonunions

The source of any failed fracture healing can be attributed to deficiency in one or more of four key factors contributing to bone healing: mechanical environment, presence of growth factors, presence of osteogenic cells, and presence of osteoconductive scaffolds [28, 29]. The importance of these four factors highlights the complicated nature of fracture healing and further emphasizes the amount of critical influences on fracture healing which remain outside of orthopaedic surgeons' direct control. It is important to note that while callus presentation provides sufficient information to categorize nonunion type, thus hinting at the cause of failed fracture healing, this is a *post-hoc* analysis, and thus does not enable surgeons to effect improved treatment during the initial stages of fracture healing. Consequently, patients at high risk of aberrant bone healing, such as those with known comorbidities, can be broadly identified at the time of initial orthopaedic surgery, but *a*

priori certainty of clinical outcome during the early stages of healing is not feasible with current clinical diagnostic standards [30].

1.3.3 Treatment of Nonunions

Much of the variance in clinicians' diagnosis time for nonunions can be attributed to the radiographic indistinguishability of delayed unions and nonunions during the early stages of healing. While nonunions often require secondary surgical treatments [26], delayed unions may proceed to clinical union without invasive intervention [11]. Consequently, nonunions and delayed unions typically receive the same noninvasive therapies during the initial onset of adverse healing in order to avert unnecessary surgical intervention of delayed unions. Upon the eventual diagnosis of nonunion, the source of healing deficiency can be identified as mechanical or biological according to the nonunion category. Despite these insights, surgical intervention is inevitable [11], with treatment type augmented to address the suspected healing deficit [26].

The gold standard treatment for instances suspected of biological insufficiency incorporates autologous bone grafts and/or bone marrow aspirate at the nonunion site as surgical intervention is performed to replace fracture fixation hardware. The autologous tissue, ordinarily harvested from the patient's iliac crest, contains osteogenic, osteoinductive, and osteoconductive cells/factors to encourage proper healing [31-33]. Cases of suspected mechanical instability are treated by either replacing the initial fracture fixation hardware with a more rigid device, or by augmenting the initial device by introducing additional hardware [32].

1.4 Improving Clinical Outcome

Treatment of nonunions is a highly invasive and costly procedure, but there are minimally invasive means to encourage the resumption of bone healing if proactively administered. Application of low intensity pulsed ultrasound (LIPUS) to the fracture sight of mechanically stable hypertrophic nonunions has demonstrated the ability to produce proper union with greater than 80% success rate, with earlier implementation of this therapy (< 6 months post-fracture) associated with improved clinical results [34]. Hypertrophic nonunions have also shown positive response to nail dynamization – a procedure in which some of the transverse pins used to lock an intramedullary nail (IMN) in place are removed to facilitate increased compression at the fracture site. Union resulting from nail dynamization offers a $10,000 reduction in direct medical costs [35] and has shown success in more than 80% of cases when implemented between 10-24 weeks post-surgery [36]. Fractures trending towards nonunion due to insufficient biological activity can be augmented with localized and systematic administration of biological factors including parathyroid hormone (PTH), bone morphogenic proteins (BMP), platelet derived growth factor (PDGF), and fibroblast growth factor (FGF) [31].

1.5 Clinical Standards in Diagnosing Fracture Healing

1.5.1 X-Ray Imaging

Fracture healing progress is standardly diagnosed through serial use of planar and/or bi-planar radiographic images [37, 38]. Radiographic imaging functions on the premise of x-rays being attenuated according to the amount of mineralized tissue between the beam emitter and receiver, thus serial x-ray images elucidate temporal progress in fracture site calcification [37]. The exact criteria of fracture union are subjective and varies among clinicians [39, 40], but typically involves

radiographic evidence of cortical continuity, disappearance of the fracture line, and sufficient callus size [16, 41]. This ambiguity has contributed to high interphysician variability [42] and accuracy as low as 50% [30] when attempting to diagnose the state of fracture healing. Consequently, x-ray imaging has exhibited poor performance as a tool for early prediction of adverse bone healing [42, 43].

Scoring methods have been developed as an attempt to create a more standardized method of diagnosing fracture healing. The Radiographic Union Score for Tibial fractures (RUST) is one such scoring method and is based upon the number of cortices which exhibit visible bone bridging [41]. Scoring methods have shown promise in improving intraobserver diagnostic variability, likely due to the establishment of definitive diagnostic parameters, but still perform poorly in predicting union state [42].

In addition to x-ray imaging's limitations from inter- and intraobserver variability, this diagnostic modality performs poorly in predicting the mechanical properties of the healing fracture site. It has been shown that radiographic imaging alone is insufficient to predict fracture callus strength [44, 45] or stiffness [23, 40]. This is particularly problematic for fractures of the lower limb where there is additional concern regarding when the fracture is of sufficient mechanical strength for safe patient weight-bearing. Discrepancy between x-ray imaging and mechanical properties of the healing fracture site can likely be attributed to changes in tissue composition which do not include the formation of calcified tissue. For example, chondrogenesis occurring during early stages of endochondral ossification ostensibly improve mechanical state of the healing fracture site, but

cause little to no change in local x-ray attenuation. Improved quantitative measurements of bone mineral data can be achieved through the use of dual energy x-ray absorptiometry (DEXA) [37], although this imaging technique still cannot capture changes occurring prior to tissue calcification.

1.5.2 Computed Tomography

Computed tomography (CT) imaging is another radiographic imaging modality that has seen increasing use in diagnosing fracture state, especially in cases suspected of trending towards nonunion [38]. CT imaging uses a spatial series of planar x-ray images measured in multiple orthogonal planes which can then be reconstructed into three-dimensional images. The three-dimensional rendering enables quantitative volumetric analysis which cannot be performed using standard planar x-ray images [24]. CT data provides a better indication of fracture mechanical properties [46], but is clinically limited due to high costs and increased patient radiation exposure [24, 47]. CT scanning is further limited due to physical phenomena, such as beam hardening and photon starving, which occur when CT scans are performed on tissues containing metallic materials such as those used in orthopaedic fixation devices. These phenomena cause severe imaging artifacts which prevent reliable quantitative measurements in the areas adjacent to orthopaedic devices, which often includes the fracture site [48].

1.5.3 Ultrasound

Ultrasound imaging of the healing fracture site is a positive alternative to x-ray imaging, DEXA, and CT scanning due to its low cost, lack of ionizing radiation, and ability to visualize non-mineralized tissue formation during the early stages of healing [37]. While this technique has

shown diagnostic aptitude, it presently exhibits severe limitations resulting from differences in operator technique, sensitivity to soft tissue overlaying the fracture site [47], and inability to penetrate hard tissue to image subcortical spaces and areas obfuscated by periosteal callus formation [24]. This can be problematic in cases of hypertrophic nonunion where there is abundant callus formation, but absence of bone bridging the fracture gap.

1.6 Fracture Healing Mechanics as a Diagnostic Modality

Mechanical state of the callus is known to be an important indicator of healing progression [49] and provides an objective benchmark for safe weight-bearing [50]. This has been standardly assessed in a clinical setting through use of manual palpation of the fracture site. However, this qualitative technique is subjective and mostly ineffective at predicting the mechanical state of the healing fracture [51]. While not in current use clinically, a variety of technologies for quantification of fracture stiffness have been developed and studied in research settings [52].

Fracture stiffness can be measured through either direct or indirect techniques. Direct measurement techniques require the controlled application of known mechanical loads to the fractured bone while measuring the resultant spatial or angular deflections of the bone fragments and/or implantation hardware. Indirect techniques frequently leverage the principle of implant load sharing to elucidate relative changes in fracture callus stiffness. This principle is characterized by mechanical load transmission across the fracture gap being distributed between the callus tissues and orthopaedic fixation hardware, where the fraction of load supported by each of these two components is dictated by their relative stiffness [53]. Thus, as healing produces increasing

fracture site stiffness, the proportion of mechanical load is increased in the fracture tissues and consequently decreased in the fixation hardware (Figure 1.3). Utilizing this principle enables indirect quantification of transient changes in fracture site stiffness by monitor the proportion of load supported by the fixation hardware. This technique has been implemented for diagnostic purposes using both external and internal fracture fixation hardware types.

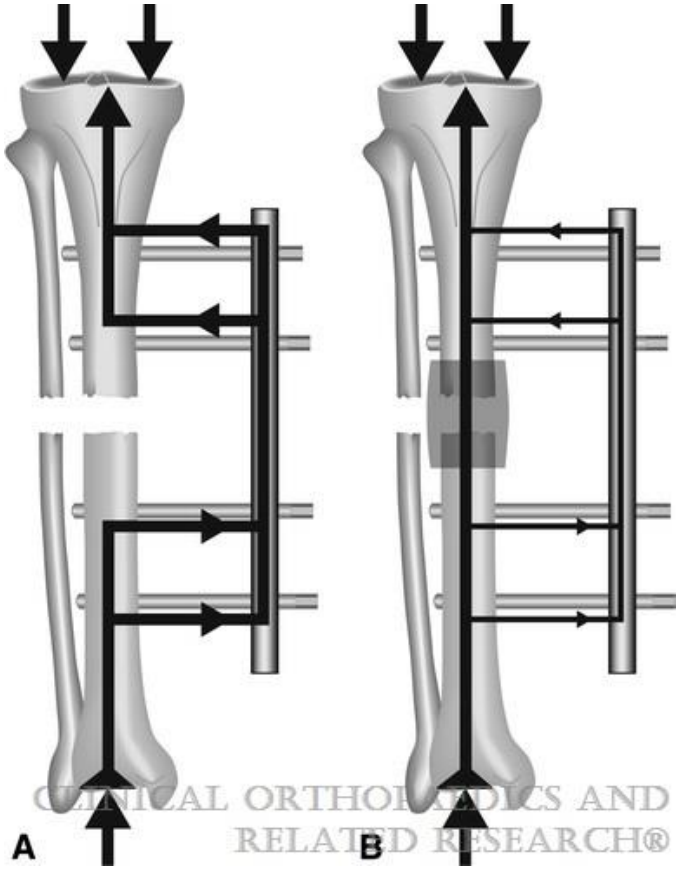

Figure 1.3: The principle of implant load sharing for a healing tibial fracture. A) At initial fracture, there is a lack of tissue at the fracture site to support weight-bearing, thus all mechanical load is carried by the fixation hardware. B) As healing occurs and fracture site stiffness increases, the proportion of mechanical load is increased in the fracture tissues and consequently decreased in the fixation hardware. (Reprinted by permission from Wolters Kluwer Health, Inc., [53] Claes, L.E. and J.L. Cunningham, *Monitoring the mechanical properties of healing bone.* Clin Orthop Relat Res, 2009. **467**(8): p. 1964-71).

1.6.1 External Fixation

A common approach to quantifying the rigidity of the healing fracture site is through the use of instrumented external fixators. External fixators largely refer to a category of fracture fixation devices in which fractures are supported by structures external to the body, which are anchored to the fractured bone via pins traversing through the overlaying soft tissue [54-56]. In cases of long bone fractures, external fixator treatment commonly utilize structural members placed in parallel to the axis of the fractured bone (Figure 1.4A) [55, 56]. With the structural member placed parallel to the fractured bone, the combined bone-fixator system can be thought of as a single composite beam with combined stiffness equal to the sum of the fracture site and external fixator stiffness [57]. The structural properties are known and temporally invariant for the fixator portion of the system, while the structural properties of the fractured bone are transient with healing. Accordingly, load is distributed between the fixator and healing fracture site based on their relative structural properties. In theory, temporal quantification of the load in the external member, relative to a known load applied to the fractured limb, provides insight to the mechanical state of the fracture site (Figure 1.4B). Cases trending towards proper healing are identified by transient reduction in the relative load share of the external fixator, while healing cessation can be predicted when temporal invariance in the fixator load share is observed [53, 58, 59].

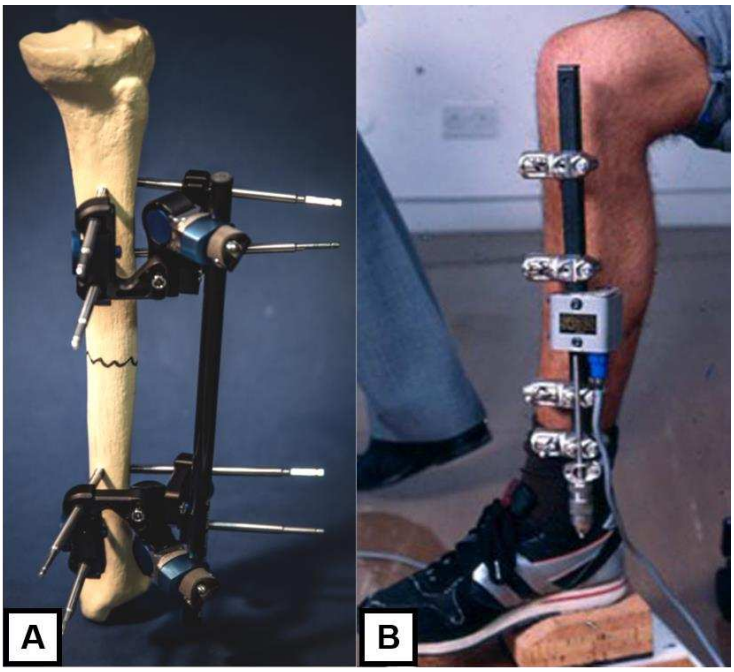

Figure 1.4: A) An example of external fixation hardware applied to a tibial fracture. In a clinical implementation, the pins attaching from the external structure to the bone transverse through skin and other overlaying soft tissues. (Reprinted from Injury, 50 Suppl 1, Bliven, E.K., et al., *External fixation of the lower extremities: Biomechanical perspective and recent innovations*, p. S10-S17, 2019, with permission from Elsevier [56]). B) An instrumented external fixator quantifies changes fracture stiffness by measuring fixator load share via wired strain gages. (Reprinted by permission from Wolters Kluwer Health, Inc., [53] Claes, L.E. and J.L. Cunningham, *Monitoring the mechanical properties of healing bone.* Clin Orthop Relat Res, 2009. 467(8): p. 1964-71).

Previous research groups have examined the feasibility of this technique using strain gauge measurement of external fixators (Figure 1.4B) [57, 60-63], as well as more advanced methods such as integrating load cells into the external fixator architecture [64, 65] or direct measurement of external member's linear [66, 67] or angular deflections under load [62, 68]. These studies have shown generally promising results with fracture stiffness measurements being a quantifiable early indicator of healing state [49, 62], as exhibited by an improved diagnosis time of 2.5 weeks relative to radiographic techniques [67]. However, this diagnostic exhibits technical limitations in instances of pin loosening which contributes to high rates of quantitative error [58, 61, 62, 64, 69]. These methods are further limited by their inability to be applied to fractures treated by internal

fixation, such as orthopaedic plates or IMNs. These alternate fracture stabilization techniques are frequently implemented due to clinical concerns with infection and soft tissue damage resulting from the transdermal pins necessary to external fixation [54, 55, 70, 71].

1.6.2 Internal Fixation

The principles behind use of composite stiffness as a diagnostic for externally fixated fractures holds true for cases treated by other means of surgical fixation such as orthopaedic plating and intramedullary nailing (Figure 1.5). Orthopaedic plating involves anchoring a metal plate to the cortices of the fractured bone using screws spanning from the plate through the bone fragments. There exist a myriad of variations to this technique which all holistically serve the same overall function of maintaining rigid alignment of the bone fragments to facilitate healing [72, 73]. Intramedullary nailing entails operative implantation of a rod within the intramedullary canal of fractured long bones, where the rod is anchored to the bone fragments by pins transversely spanning to the bone cortices. As with plate fixation, this a broad simplification of a varied and nuanced surgical technique, but the general function remains the same as that of orthopaedic plating and external fixation [74].

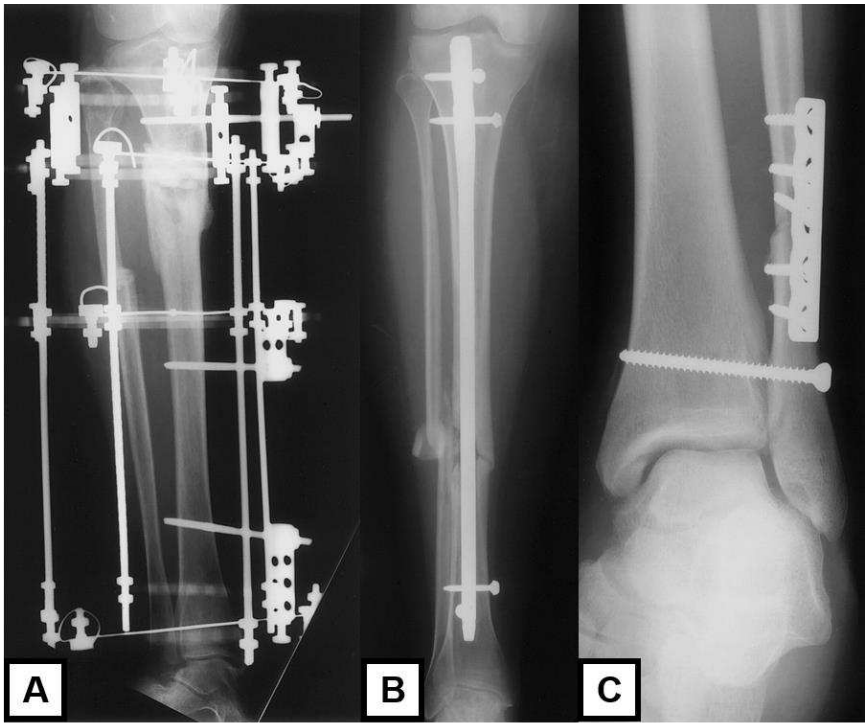

Figure 1.5: X-ray imaging comparison of lower leg fractures treated by A) external fixation, B) intramedullary nailing, and C) plating fixation techniques. (Reprinted with permission from Radiological Society of North America, [73] Taljanovic, M.S., et al., Fracture Fixation. RadioGraphics, 2003. 23(6): p. 1569-1590).

The appeal of using external fixators for quantifying healing fracture stiffness can be attributed to the accessibility of hardware measurement sites outside of the body. Consequently, strain gauges, load cells, and/or goniometric sensors can be implemented based off of their technical performance without consideration for their biocompatibility or other biological factors. Orthopaedic plating and intramedullary nailing are both forms of internal fixation, in which all orthopaedic hardware is contained within the body. Consequently, all hardware instrumentation must be particularly concerned with biocompatibility and infection prevention; clinical implementation of instrumented internal fixation devices must therefore overcome strict regulatory hurdles. Efforts have been made, nonetheless, to quantify healing fracture stiffness using instrumented internal fixation hardware.

Previous studies have implemented orthopaedic plates instrumented with wired strain gauges as the primary [75] or secondary [76] fixation technique in ovine osteotomy fracture models, where surface strain at the plate midspan was measured during walking via transdermal wires. Both studies demonstrated that plate surface strains tended to peak within the first 2-3 weeks post fracture and then continually decreased to a minimum value at fracture union [75, 76]. While neither of the aforementioned studies sought to utilize strain data for diagnostic purposes, the findings nonetheless support the theory that implant strain provides a quantifiable measure of fracture healing progress.

1.6.3 Telemetric Techniques

To assuage challenges associated with collecting data from internal fixation techniques, there has been a recent push to develop telemetric sensors which are capable of wirelessly reporting implant surface strain [77]. While this technique must still consider biocompatibility of the telemetric sensors, the lack of an interface spanning from the fracture site to the external environment significantly reduces the likelihood of infection. Furthermore, there exists biocompatible sensor encapsulation materials which alleviates design restrictions pertaining to sensor material selection.

In a previous study, Kienast et. al. designed a custom fixation plate featuring a telemetric strain gauge at the plate midspan for use in treating femoral fractures (Figure 1.6). The custom plate was designed such that plate surface strain could be wirelessly recorded by a telemetry module located outside of the body, where strain was measured during limb weight-bearing on a load platform. The custom implant was used for revision surgery in 39 patients suffering from femoral nonunion.

By performing repeated measurements throughout the healing process, this device was able to identify four distinct healing outcomes according to their temporal progression of fracture stiffness: fast healing, slow healing, plateau followed by healing, and non-healing [78].

Figure 1.6: Instrumented titanium internal fixator plate for telemetric assessment of fracture healing (Republished with permission of British Editorial Society of Bone & Joint Surgery from, [69] *Telemetric assessment of bone healing with an instrumented internal fixator: a preliminary study*, Seide, K., et al., **94**(3), 2012; permission conveyed through Copyright Clearance Center, Inc).

These findings were further supported in a follow up study with additional human femoral nonunion patients, with this study demonstrating quantifiable changes in fracture site mechanics during the initial weeks post-surgery, well before radiographic indications of healing [69]. The temporal profiles of implant strain from fast healing cases from these studies closely resembled the profiles measured by studies using wired strain gauges [75, 76]. Initial findings from this technology mark great improvement towards the development of a quantifiable diagnostic of fracture healing outcome, but expectations must be tempered by the limitations inherent to a rigid

sensor, regardless of telemetric ability. For proper measurement of implant surface strain, it is imperative that the implant contains a flat surface of sufficient footprint to accommodate the telemetric strain gauge, thus restricting the application of these sensors to custom designed plates of very specific geometric design. Furthermore, measurements are susceptible to interpatient variations resulting from muscular induced loading [78] and diagnostic ability can be indefinitely compromised or lost when sensors loosen from the fracture plate [69].

Mixed results have been obtained when using instrumented IMNs. In one study, telemetric measurements obtained from instrumented femoral IMNs exhibited a similar temporal decrease in implant strain, with strain values markedly decreasing prior to the appearance of radiopacity at the fracture site [79]. A similar technology, in an ovine model, established IMN forces to be unchanging over time in instances trending to nonunion; however, this study demonstrated difficulties associated with the surgical implantation of an instrumented nail and with performing telemetric data collection through large amounts of soft tissue [80].

1.6.4 Challenges to Telemetrically Instrumented Internal Fixators

Prior studies have established the efficacy of temporal measurement of implant surface strain as an early predictor of fracture healing outcome, but there remain large technical obstacles to be surmounted prior to clinical implementation. Namely, telemetric circuits for direct measurement of implant strain involve multiple components which must be integrated into the fixation hardware, such as the strain gage, amplifier, signal conditioner, and means to transmit the signal. Designs which do not utilize inductive powering must further consider the size and longevity concerns

associated with batteries or implement energy harvesting techniques [81]. The complexity of these circuits causes telemetric sensors to occupy appreciable space, thus orthopaedic hardware must be physically modified to accommodate telemetric sensor systems. Such modifications can be difficult to achieve in a safe and effective manner as small modifications to implant design can dramatically change the hardware's stiffness or strength [79], thus reducing its safety or propensity to encourage proper healing.

The push to implement microelectromechanical sensors (MEMS) has enabled the minimization of telemetric sensor footprints, but reduction of sensor areas are associated with elevated operating frequencies (gigahertz range) [82, 83]. The higher frequencies associated with MEMS devices can be deleterious to telemetric readings as signal attenuation through biological tissue is inversely proportional to signal frequency [84]. Issues pertaining to telemetric signal loss through soft tissue has been previously observed [80].

1.6.5 Resonant Biomechanical Diagnostics

Resonator based sensors offer an alternative to true telemetric implant sensors. Resonators broadly refers to a class of sensors which do not require a power source, supporting circuitry, or telemetric data transfer. Instead, these sensors resonate at a specific and quantifiable frequency when exposed to an electromagnetic field. These sensors are designed such that changes in their physical state, such as those incurred by mechanical strain, alters their electromagnetic properties to produce a shift in resonant frequency as measured by an antenna [81]. The simple design of these sensors facilitates a small footprint to better accommodate unmodified orthopaedic hardware geometries

[85, 86] while further allowing antenna-sensor resonance ranges to be tuned to lower frequencies where tissue attenuation is less problematic [87].

Despite several attempts to develop resonance strain sensors for use in fracture fixation diagnostics [86, 88-91], there is very little published literature on clinical or pre-clinical implementation of this technique. Our research group has previously developed a rigid implantable resonator strain sensor (bioMEMS) for use in fracture healing prediction and diagnosis (Figure 1.7) [82, 83, 87, 92-95], which was then implemented in a preclinical comparative ovine fracture model. This study demonstrated positive results by quantifying differences in temporal implant strain profiles to successfully predict fracture healing outcome as early as 21 days post-fracture [96]. However, the rigid design of this sensor design fails to obviate the need to modify orthopaedic hardware to produce a flat surface for sensor adherence, and is limited to reporting implant mechanics at a single location.

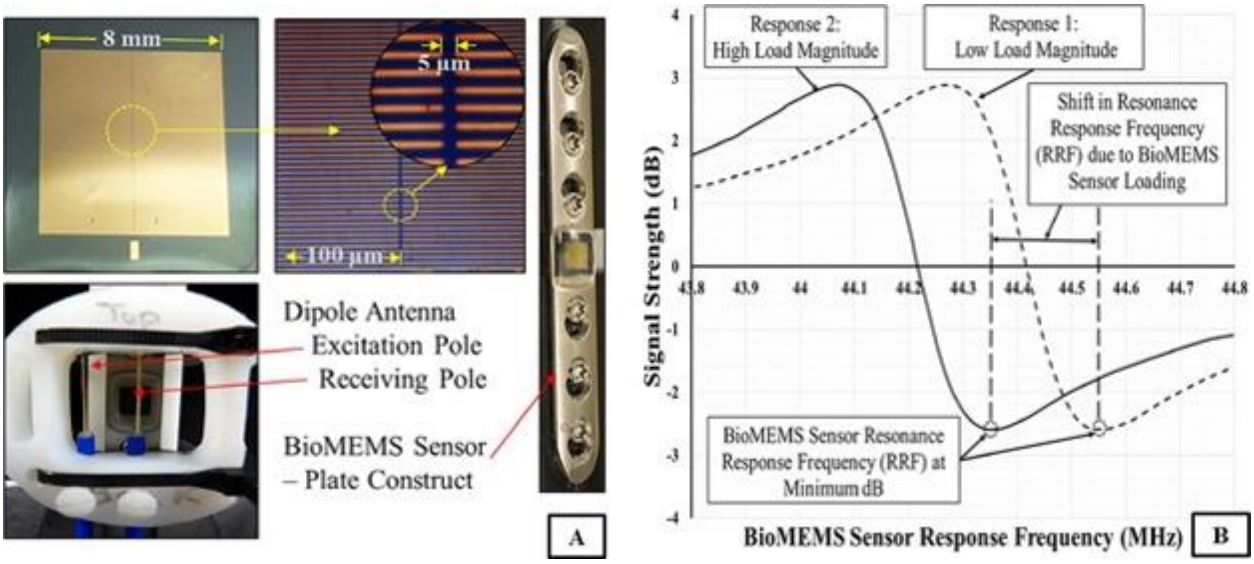

Figure 1.7: A) Microscope images of the bioMEMS sensor exhibit the split ring resonator structure which changes the electromagnetic properties (total capacitance) of the sensor when subjected to implant surface strains. B) Antenna measurements of the sensor produces characteristic curves with a resonant radio frequency (RRF, minimum of frequency-dB data). Mechanical strain on the sensor causes the RRF of the sensor to shift. (Republished with permission from John Wiley and Sons, [96] McGilvray, K.C., et al., *Implantable microelectromechanical sensors for diagnostic monitoring and post-surgical prediction of bone fracture healing.* J Orthop Res, 2015. **33**(10): p. 1439-46).

1.6.6 Direct Electromagnetic Coupling (DEC)

While characterizing the bioMEMS sensors, it was observed that antennas aimed towards metallic orthopaedic hardware were still capable of producing repeatable resonant frequency shifts after removal of all sensors. This phenomenon was later attributed to direct electromagnetic coupling (DEC) of the antenna to the metallic hardware which created a resonant frequency which varied according to the distance between the two coupled members. Labus et al. went on to develop DEC antennas for the specific application of sensing orthopaedic implant deflections [97]. As a diagnostic tool, DEC performs as a hybrid of the "direct" and "indirect" measurement techniques described on page 11. A known mechanical load is applied to the fractured limb to produce a resultant deflection of the metallic orthopaedic fixation hardware. Hardware deflections produce

a quantifiable shift in the resonant frequency of the DEC antenna, where shift magnitude is proportionate to the magnitude of implant deflections. In turn, implant deflections vary according to fracture callus stiffness given that the bone-implant behaves as a composite structure. Thus, deflections for a known mechanical load are indirectly, and noninvasively, measured via the DEC system, therefore providing a relative measurement of fracture stiffness. While this technique cannot directly capture implant strains or direct measurements of fracture stiffness, it is highly advantageous due to its presumed validity for any off-the-shelf metallic orthopaedic implant, thus maximizing its applicability and simultaneously minimizing regulatory barriers to clinical implementation.

1.7 Summary

Despite a thorough understanding of the biology and mechanics pertinent to bone fracture healing, adverse healing remains difficult for clinicians to predict at initial surgical fixation or during the early stages of healing. Studies have shown that early diagnosis of fracture healing outcome may reduce patient medical costs, suffering, and offers the potential for improved clinical outcome by early application of appropriate noninvasive therapeutics. The ability to effect these positive changes is hindered by the inefficacy of the current standard diagnostic modality, x-ray imaging. X-ray imaging is slow at providing insight to the state of healing due to its dependence on calcified tissue formation. Thus, it is imperative to develop new diagnostic modalities capable of predicting fracture healing outcome during the initial stages of healing.

While tissue calcification typically does not occur until the latter stages of healing, there a number of morphological changes which occur early during the healing cascade, which result in changes to the structural properties of the healing fracture tissues. Previous studies have demonstrated that indirect quantification of the fracture stiffness can be achieved by measuring the surface strains of orthopaedic fixation hardware due to the behavior of the bone-hardware system as a composite structure. Existing technologies have utilized this principle to successfully predict fracture healing outcome in the initial stages of healing and have been used to distinguish delayed unions from nonunions to avoid unnecessary secondary surgical interventions. Despite the success of previous studied technologies, current techniques remain limited to external fixators or internal fixators with heavily modified geometries which frequently compromises their safety and efficacy.

The purpose of this work was thus to develop a novel diagnostic tool which may be used with un- or minimally-modified internal fixators for noninvasive early prediction of long bone fracture healing outcome by quantification of healing fracture stiffness.

CHAPTER 2: SPECIFIC AIMS

The ensuing Specific Aims have been identified as steps for completing the aforementioned goal. It should be noted that the development of new technologies is an inherently iterative process and identification of technological improvements are inevitable during progression through these Specific Aims. As such, the technology which initiated this research (i.e., fsBioMEMS sensors) endeavor exhibited promising results during Specific Aim 1, but unsatisfactory performance during Specific Aim 2. An improved technology (i.e., coiled coaxial DEC antenna) was thus implemented and revaluated within the context of Specific Aims 1 & 2. Despite the success of this second iteration, potential improvements were identified and implemented in a third technological iteration (i.e., miniaturized Vivaldi DEC antenna). The efficacy and clinical applicability of the final design were explored within the context of Specific Aims 1 & 3. This body of work concludes by recommending additional improvements to be made in future technological iterations.

2.1 Specific Aim 1

Develop a noninvasive technology which indirectly quantifies relative fracture stiffness of bone fractures treated by internal fixation.

Benchtop studies were performed to identify clinically feasible and robust sensors, sensing technologies, and mechanical loading procedures for quantifying temporal changes in the relative stiffness of healing fractures. A series of experiments were performed to evaluate the ability of resonant strain sensors to detect changes in the structural integrity of simulated fracture healing using benchtop and *in vitro* methods. Following technological redevelopments, this process was

repeated for two novel technologies utilizing direct electromagnetic coupling for sensing orthopaedic hardware deflection resulting from limb loading.

2.2 Specific Aim 2

Evaluate the efficacy of the technology developed in Specific Aim 1 in a translational comparative animal model.

The efficacy of the technologies characterized in Specific Aim 1 were characterized using an ovine osteotomy fracture model. Diagnostic data was collected weekly to determine the ability of the technology to predict fracture healing outcome relative to standard radiographic images. Post-mortem analyses included histomorphometry to quantify bone, four-point bending to calculate final bone fracture stiffness, and micro computed tomography imaging to compute final bone formation at the fracture site. Results of this study advised technological redevelopments, which were subsequently evaluated to meet the needs of Specific Aim 1.

2.3 Specific Aim 3

Interrogate the potential for the technology developed in Specific Aims 1 & 2 to predict fracture healing outcome in clinically common fracture types using finite element analysis.

A custom finite element model was developed to simulate an ovine osteotomy fracture treated by orthopaedic fixation. Implant mechanics as a function of fracture healing, fracture size, implant type, implant design, and implant material were parametrically analyzed and validated by numerical modeling, mesh convergence, and *in vitro* biomechanical testing. This parametric finite element analyses explored pertinent mechanics for clinically relevant permutations of fracture and

treatment, which cannot be tested through exhaustive *in vivo* methods. Results informed the efficacy and applicability of the technology developed in Specific Aim 1.

CHAPTER 3: BIOMEMS RESONANTOR STRAIN GAUGES (SPECIFIC AIM 1 & SPECIFIC AIM 2)[1]

Chapter 3.1 details Specific Aim 1 using fsBioMEMS technology, and have been published a peer-reviewed full length research article [98]. Chapter 3.2 details application of this technology to Specific Aim 2. The findings of Chapter 3.2 are not published, but were utilized to advise the requisite progression to the technology detail in Chapter 4, which in turn lead to the development of the technology detailed in subsequent chapters.

3.1 Specific Aim 1

3.1.1 Introduction

During the normal reparative process of orthopaedic fractures, the mechanical stability of the fracture site increases as the injury progresses through the stages of healing [21, 53, 60, 67, 75, 76, 99, 100]. It has been shown through the use of wired strain gauges that bone and the healing callus support an increasing fraction of external loads during the healing process, while load fraction is temporally decreased in the implanted surgical hardware [60, 75]. In the case of abnormal healing, leading to delayed or non-union, this temporal load sharing profile is significantly altered [96]. Reported incidence rates of delayed and non-union demonstrate large variability [9, 101-103], reaching values as high as 38% [101], and are dependent upon the location, severity, and treatment method of the fracture [9] [3, 6, 14, 104]. In spite of this, it has been shown that implant stability and loading is critically related to bony healing [21, 75, 76, 99, 100, 105-107]. Failed primary

[1] Chapter 3.1 has been published in *The Journal of Orthopaedic Research* (DOI: 10.1002/jor.24325) [98]. All contents have been republished with permission from John Wiley and Sons: Wolynski, J.G., et al., *Utilizing Multiple BioMEMS Sensors to Monitor Orthopaedic Strain and Predict Bone Fracture Healing.* J Orthop Res, 2019. **37**(9): p. 1873-1880.

operations are often revised via surgical intervention, with the clinical result of these revision procedures being negatively correlated with the time interval between the first and second surgeries due to aggregation of fibrous tissue within the fracture gap [108]. Furthermore, prior studies have suggested a substantial reduction in financial burden when early intervention is implemented to prevent delayed union [9, 13], thus driving the need for early diagnostic modalities with high sensing fidelity/resolution.

Early fracture healing observation remains a difficult and qualitative process for clinicians [16, 45, 109], which has been identified as an area necessitating diagnostic improvement [14, 39, 42]. Bone healing is typically monitored through the usage of planar radiographic imaging or manual manipulation of the fracture site. However, physical manipulation is prone to subjective interpretation by the clinician [51], and radiographs are prone to similar analysis inaccuracies leading to high inter-physician variability [16, 39, 42]. Additionally, early radiographic analysis has shown limited success in predicting callus stiffness [44] and likelihood of delayed and non-unions [42, 43]. Radiographs are also limited as an early diagnostic tool as they do not indicate healing until sufficient callus calcification, 6-8 weeks post-fracture [110], thus leading to a 50% probability of correctly predicting union stage [30]. Quantified fracture stiffness, however, elucidates the healing status as much as 2.5 weeks before this information is revealed via radiographic analysis [67].

There is a current lack of noninvasive diagnostic measures to determine callus strength, a metric which is crucial in diagnosing the state of bone healing and the patient's ability to bear weight [37,

42, 67]. Previous studies have shown success in the use of sensors to telemetrically quantify construct mechanical environment [82, 83, 87, 92, 93, 95, 111]. Use of a single wireless, biocompatible, microelectromechanical system (BioMEMS) sensor has previously utilized the bone-implant load sharing principle to successfully detect statistically significant differences in normal and delayed healing in an ovine animal model as early as 21 days post-fracture [96]. This study demonstrated that by monitoring hardware stain, via the BioMEMS sensor in an area adjacent to the fracture site, it was possible to detect the healing cascade pathway (i.e., union versus nonunion) in the critically important early healing time (i.e., prior to radiographic evidence of union versus nonunion) [96]. While the BioMEMS sensor showed effectiveness as a single sensor in orthopaedic plating applications, the rigid substrate of this sensor restricts its clinical applicability to hardware containing regions of flat surface geometry. Furthermore, use of a single sensor limits this technology to providing diagnostic information with regards to the load-sharing between the hardware and healing bone at a single hardware location.

Intra-implant strain on surgical nails and plates differ by over 200% [112, 113]; consequently, substantial variations in the location of implant failure have been reported due to stress rising features such as screw holes [114-116]. Despite the vast quantity of literature analyzing the relationships between orthopaedic implant design and fracture healing, there is a lack of definitive consensus on optimum treatment techniques. Use of excessively stiff implants leads to increased rates of non-union, while excessively compliant implants can result in hardware failure [117]. This suggests a potential for an optimum intermediate implant design which could feasibly be patient specific. A better understanding of implant temporal and geometric strain profiles presents a potential tool to improve orthopaedic hardware design; however, to our knowledge, there is no

current technology which allows for noninvasive *in vivo* measurements of implant strain at multiple locations. Accordingly, it is theorized that *in vivo* measurements of implant strain along the length of orthopaedic implants (i.e., at multiple locations) could have a significant impact on fracture fixation hardware design to substantially improve clinical outcome. To address this need, and the current limitations of the BioMEMS sensor, we have developed an antenna array and a flexible substrate BioMEMS (fsBioMEMS) sensor which allows multiple telemetric sensors to be applied along contoured surfaces of orthopaedic hardware, such as intramedullary nails (IMN) and fracture fixation plates, to simultaneously determine the mechanical environment at multiple discrete locations.

3.1.2 Materials & Methods

3.1.2.1 fsBioMEMS Fabrication

Our group has performed a series of experimental and analytical investigations of increasing complexity upon MEMS-based telemetric measurements of local fracture mechanics by observing shifts in the sensor's resonance response frequency (RRF) using computational models, prototype fabrication, *ex vivo* simulations, and *in vivo* animal models [82, 83, 87, 92, 93, 95, 96, 111]. The current system is composed of a multi-sensor fsBioMEMS sensor-implant construct and an external excitation/receiving apparatus consisting of a multi-antenna array and a network analyzer (Figure 3.1). The multi-antenna array is designed with five evenly spaced antennae, allowing for simultaneous excitation/receiving of RRF signals from five independent fsBioMEMS sensors. Each antenna emits an electromagnetic wave with a unique frequency inducing a differential current and associated resonance within each fsBioMEMS sensor. The particular resonance within each sensor is dependent upon its architectural features. Deformation of the sensor's split ring

architecture, due to physical loading, induces changes to the sensor's capacitance [111]. Changes in capacitance resulting from external loading produces a shift to the sensor's spectral RRF. The sensor architecture is designed to ensure that the RRF shifts linearly with the sensor's principal strain [111].

The sensors are fabricated with standard MEMS fabrication methods utilizing a polyimide tape substrate (Kapton HN, DuPont, Wilmington, DE), gold metal layering, and a Si_3N_4 dielectric layer [82, 83]. These materials were selected to ensure enhanced sensor performance, while maintaining the requisite biocompatibility [96]. The sensor dimension is a square with 8 mm sides and 0.8 mm thickness (Figure 3.1). Sensor and antenna architectures were designed such that each of the five antenna-sensor combinations yield deep and sharp dips in the spectral RRF at sub-GHz frequencies, as described in the proceeding section. The specific fabrication details for the MEMS architecture can be found in previous studies by McGilvray et al. [96] and Melik et al. [92]. The only fundamental change within the BioMEMS fabrication process previously described was to replace the rigid silicon substrate with a flexible polyimide substrate.

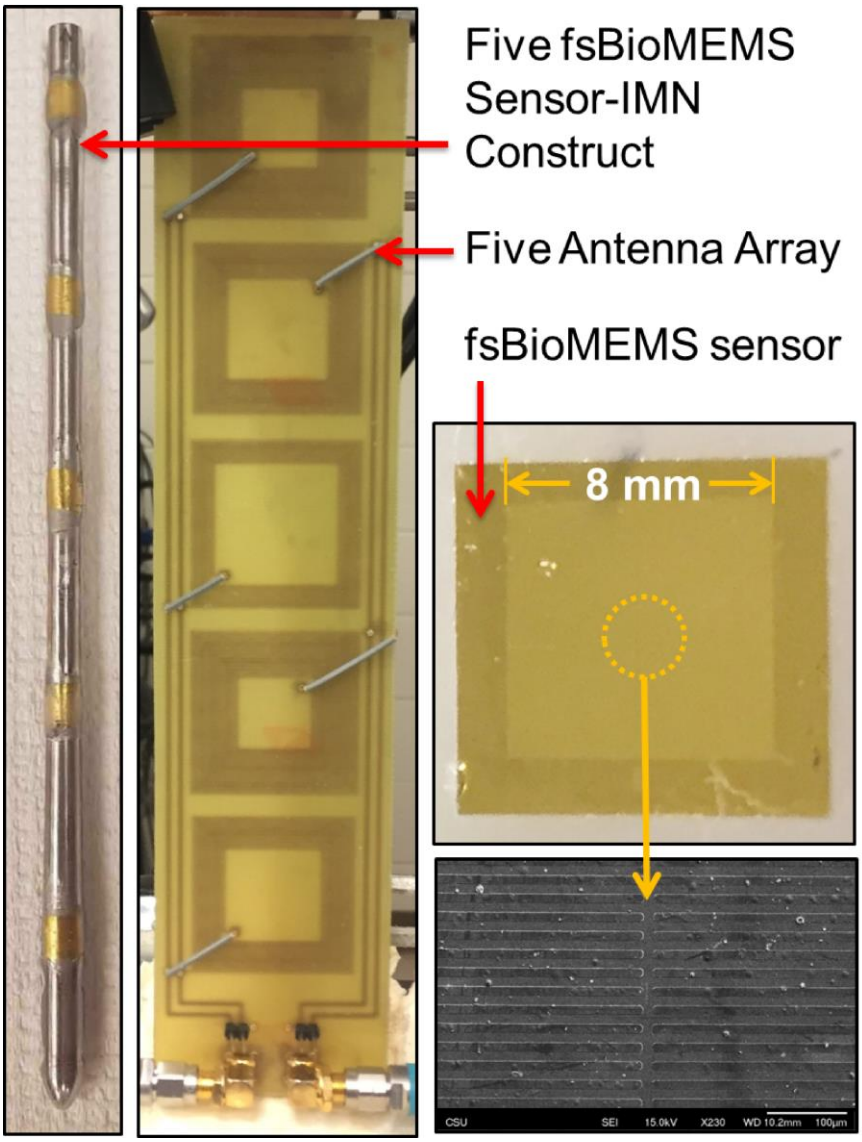

Figure 3.1: Macro and scanning electron microscopy digital images of a single fsBioMEMS sensor, digital image of the sensor-IMN construct containing five evenly space fsBioMEMS sensors, and a digital image of the five antenna array used for measuring resonant radio frequency (RRF) of the fsBioMEMS sensors.

To create the fsBioMEMS sensor-IMN construct used within this study, five fsBioMEMS sensors were rigidly attached to an 8 mm diameter by 197 mm length IMN (Biomedtrics I-Loc IM Fixator, Whippany, NJ) at evenly spaced distances of 40.64 mm (based upon the placement of sensor 3 at the IMN mid-span) using cyanoacrylate (Locktite, Düsseldorf, Germany) before coating with

layers of two-part high tensile strength epoxy (2 Ton Clear Epoxy, Devcon, Danvers, MA) and medical-grade polyurethane (Master Bond, Inc. Hackensack, NJ).

3.1.2.2 Antenna Array

The use of a multiple antenna array, as opposed to utilizing multiple sensors with varied architecture, has a number of advantages: (1) elimination of the need to trace the implant location of each specific sensor architecture, (2) utilization of identical sensors, from the same batch, reduces fabrication-induced discrepancies between sensors, (3) system redesigns can be implemented to the antennae, thus allowing for continued improvements after *in vivo* sensor implantation. The multi-antenna array was designed to reduce data collection time, minimize cross-talk between sensor-antenna pairs, and to concurrently evaluate all sensors. This is achieved through parallel antenna connection to a two port network analyzer which simultaneously collects the ratio of reflected signal to input signal (reflection coefficient) at each network port (S_{11} and S_{22} parameter data).

Computational simulations were performed to determine prospective antennae designs which were then selected for prototype fabrication (Figure 3.2). Benchtop collection of the prototype antennae's RRF data (S_{11} parameter frequency and gain) was performed to determine the operating spectral ranges and quality factors (Q-factor) of the antennae.

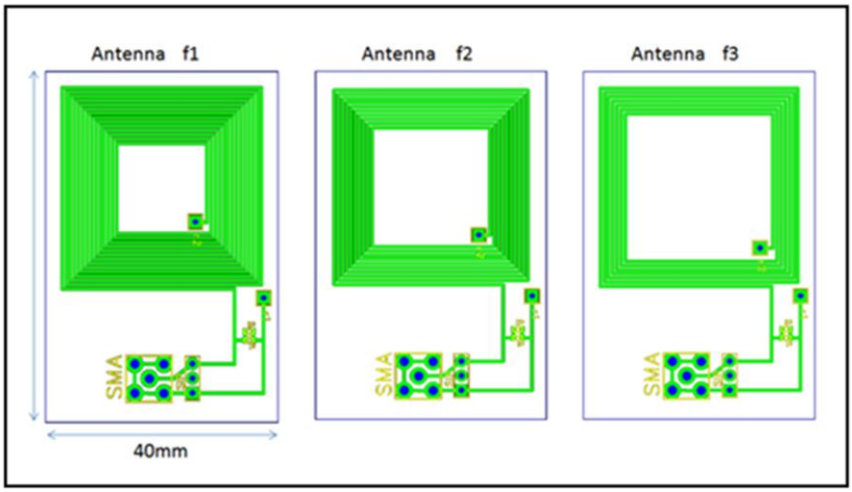

Figure 3.2: Schematic of the antennae designed to produce non-overlapping RF responses.

Utilization of unique architecture resulted in three feasible antenna designs for prototype analysis. The resulting RRF spectra of these antennae, when coupled to fsBioMEMS sensors, produced discrete, non-overlapping RF spectra (Figure 3.3). The Q-factor associated with the antennae demonstrated Q-factor values of 71, 35, and 25 for the v2_f1, v2_f2, and v2_f3 antenna designs; respectively. Parallel deployment of these three architectures while recording two network ports (S_{11} and S_{22}) allows for simultaneous data collection from up to six fsBioMEMS sensors.

Despite each antenna array being designed to contain unique and discrete resonance frequencies, the possibility existed for individual antenna to be effected by multiple sensors; thus, experiments were performed to quantify the relationship between sensor spacing and sensor cross-talk. A sensor was aligned beneath a single antenna while RRF data were collected as a second sensor was moved discrete unidirectional distances from the first sensor (minimum and maximum sensor spacing distances of 10 mm and 40 mm, respectively). The findings from these experiments were used to

produce an antenna array with minimized sensor cross-talk (Figure A.1 - Figure A.3, located in Appendix A).

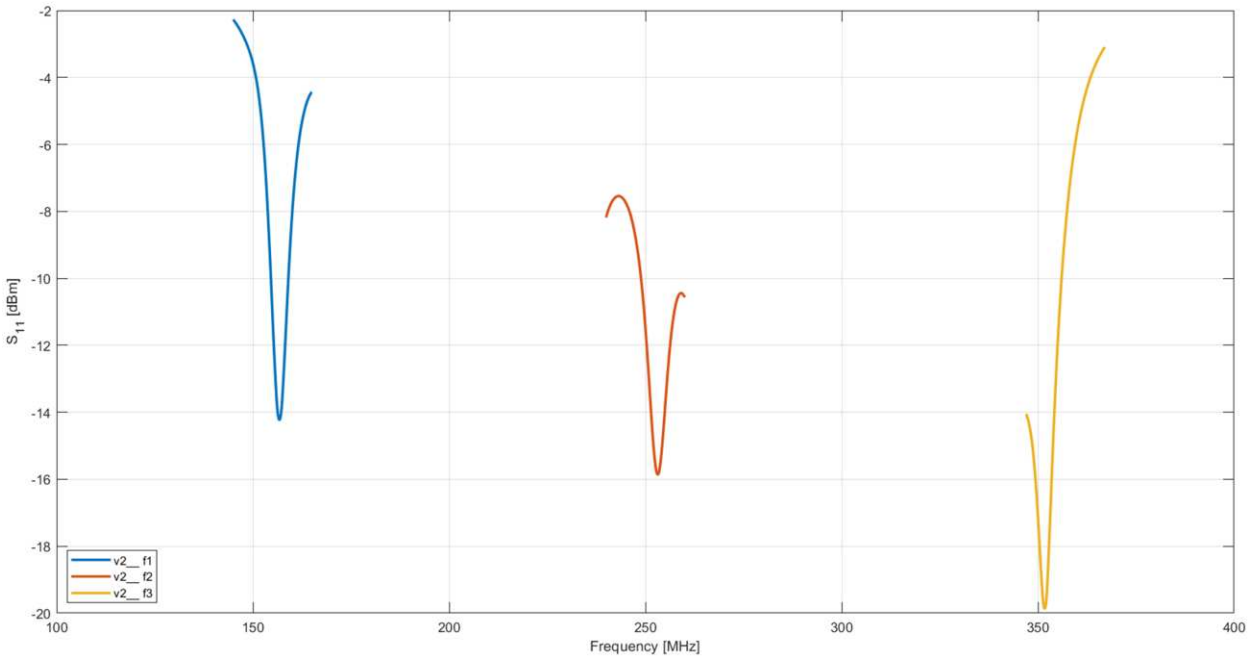

Figure 3.3: RRF responses measured for the original and prototype antenna designs.

3.1.2.3 Tissue Attenuation

In order to ensure *in vivo* feasibility of the sensor-IMN construct, parametric studies were performed to investigate the effect of soft tissue thickness and/or composition on RRF measurements from the fsBioMEMS sensors [96]. A sensor-IMN construct was placed in a custom loading fixture which allowed for IMN rod bending and unidirectional movement of the antenna array relative to the construct (Figure 3.4). Bending was induced (1 - 4 N-m in 1 N-m increments, n = 5 loading cycles per data collection period) by the addition of weights to the cantilever arm while RRF changes in each sensor were measured by the antenna array and network analyzer (R&S ZVB4, Rhode & Schwarz, Munich, Germany). The bending moment was measured with a 6

degree-of-freedom (DOF) load cell (AMTI MC3A-100, AMTI, Watertown, MA). The distance between the antenna and IMN-construct was progressively increased as the intervening space was filled with a homogenous composition of cadaveric ovine tissue; this was repeated for multiple tissue types (i.e. muscle, fat, or skin). Tissues for this experiment were collected from unrelated studies. Soft tissue thickness was increased until signal strength was determined to be fully attenuated, as indicated when the average total sensor RRF shift magnitudes diminished to approximately 15% of their initial values (relative to the smallest tissue thickness).

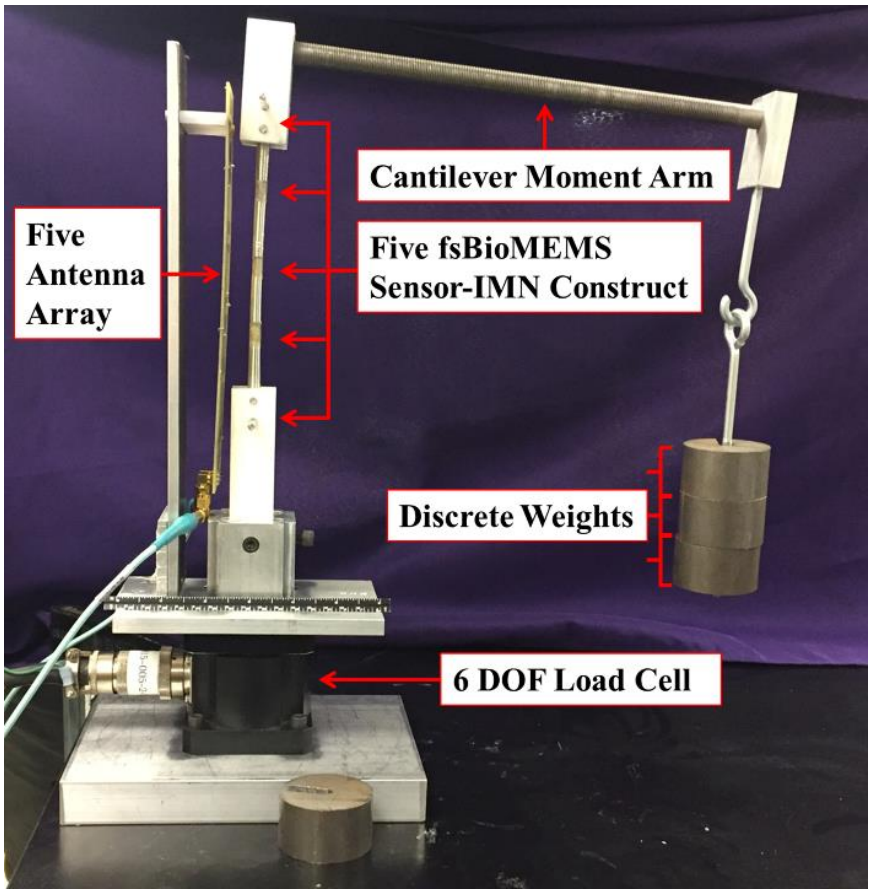

Figure 3.4: Custom cantilever fixture applying bending moments to a fsBioMEMS sensor-IMN construct while a five antenna array measures the sensors' RRF. The fixture design allows for consistent placement of the sensor-IMN construct, relative to the antenna array, during tissue attenuation analysis.

3.1.2.4 fsBioMEMS Sensor Temporal Sensitivity

To simulate the temporal shift of callus tissue stiffness during normal healing, an *ex vivo* ovine osteotomy model stabilized by locking IMN was performed [96]. Cadaveric tibae from ovine hind limbs, euthanized for unrelated studies (n = 9 hindlimbs), were dissected to remove soft tissue and then fixed with a five sensor-IMN construct. All tibiae were tested using the same sensor-IMN composite to eliminate effects due to differences in sensor placement. Mechanical testing for all tibiae was repeated at three osteotomy states. The osteotomies were produced by a bone saw cut to reduce cortical bone thickness by half or full thickness near the height of the middle sensor ipsilateral to the bending-induced compression (i.e., opposite the antenna and sensors). In this way, the tibia construct was tested at fully intact, half osteotomy, and full osteotomy states (Figure 3.5B).

The ends of each limb were potted in two-part hard cast resin (SmoothCast 321, Smooth-On, Macungie, PA) to ensure proper mechanical fixation. A servo-hydraulic testing system (858 MiniBionix, MTS Systems Corp, Eden Prairie, MN) was used to apply compressive loads (100-700 N in 100 N increments; n=5 cyclic tests per sample per fracture state) to the potted construct while measuring the RRF spectrum of each sensor using the antenna array and network analyzer (Figure 3.5). The testing set-up was designed to apply combined compression and bending loading, while further allowing for consistent placement of the antenna array relative to the tibia across all fracture states. Sensor sensitivity was calculated as the mean slope of a linear fit trend line to each cycle's load-RRF data.

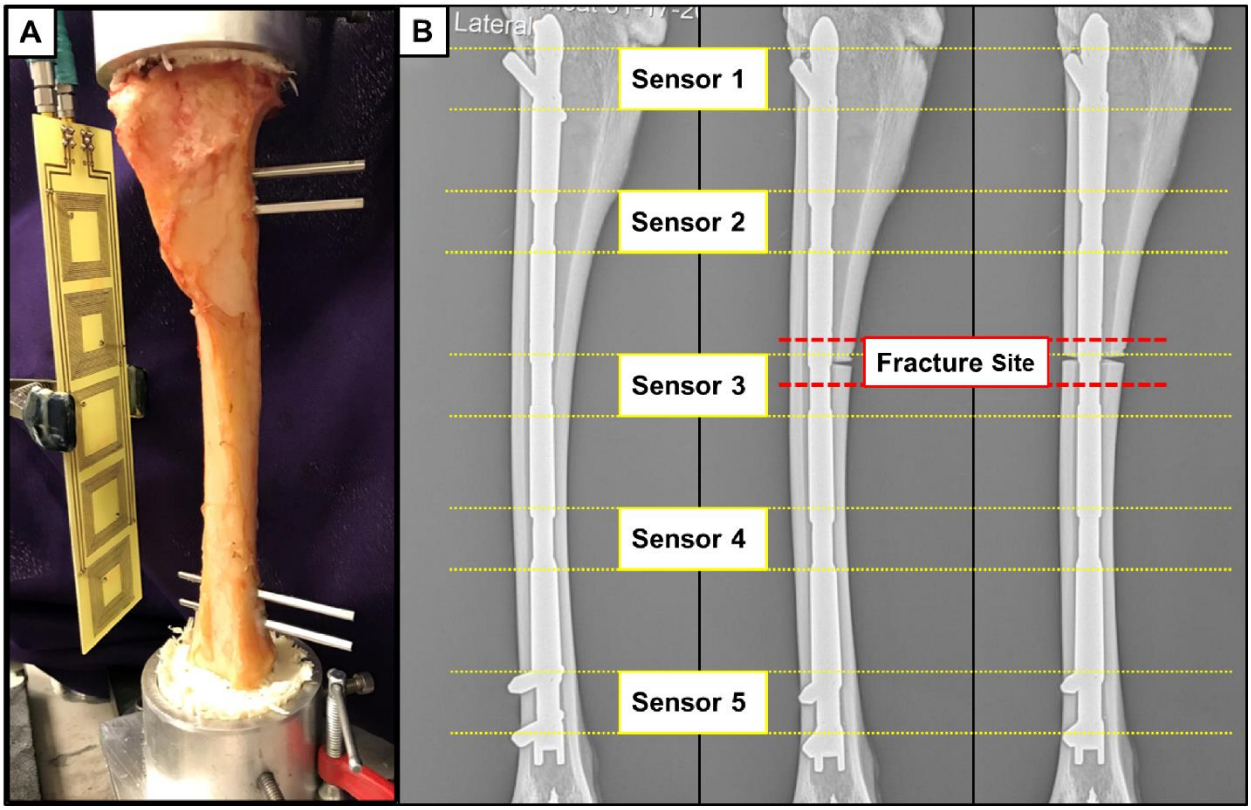

Figure 3.5: (A) Dissected ovine tibia, fixed via fsBioMEMS sensor-IMN construct, undergoing complex loading (compression and bending) while a five antenna array measures the RRF of the five fsBioMEMS sensors. (B) Radiographs demonstrating the five fsBioMEMS sensor locations and osteotomy states used to simulate the temporally increasing bone stiffness of a healing fracture: fully intact, half osteotomy, full osteotomy (from left to right).

3.1.2.5 Statistical Analyses

All data were analyzed for normality before statistical differences were determined using a one-way analysis of variance (ANOVA). When statistical differences between groups were indicated by the ANOVA, specific statistical significances were determined by a *post hoc* Tukey test (Minitab, State College, PA). Non-normally distributed data was evaluated for statistical significance using a Kruskal-Wallis test and *post hoc* Dunn's test. P-values less than 0.05 were considered statistically significant.

3.1.3 Results

3.1.3.1 Tissue Attenuation

Signal attenuation experiments demonstrated that RRF signal changes could be measured through as much as 90 mm of muscle, 50 mm of fat, or 30 mm of skin. Measurements of signal through an unobstructed air gap established a loss of measurable RRF signal change after 10 mm (Figure 3.6).

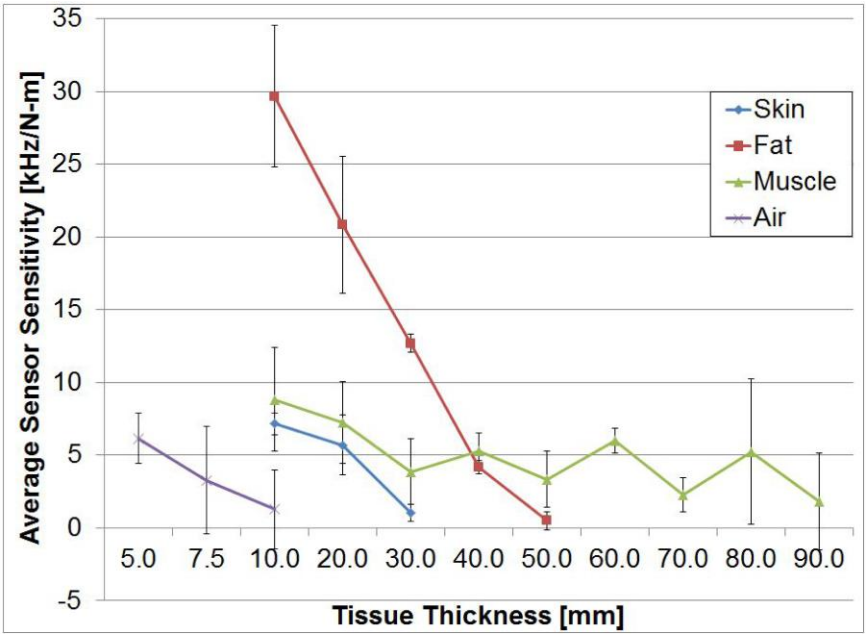

Figure 3.6: Comparison of the effects of intervening ovine cadaveric tissue type and thickness on sensor sensitivity. Sensor sensitivity through 30 mm of skin differed significantly from 10 mm ($p = 0.002$) and 20 mm of skin ($p = 0.028$). Within fat, sensitivity at 10 mm thickness was significantly different from 40 mm ($p = 0.001$) and 50 mm ($p < 0.001$), and 20 mm thickness exhibited significantly higher sensitivity than 50 mm ($p = 0.001$). Sensitivity through 10 mm of muscle differed significantly from 70 mm ($p = 0.015$) and 90 mm of muscle ($p = 0.009$).

3.1.3.2 fsBioMEMS Sensor Temporal Sensitivity

An *ex vivo* ovine tibia fracture model, surgically stabilized by sensor-IMN constructs, indicated it was possible to correlate changes in sensor RRF response to construct loading under compression-bending complex loads. When grouping all samples, the average sensor sensitivities decreased as

the amount of bone at the osteotomy site increased, with the exception of sensor 5 from the full osteotomy to half osteotomy models which increased from 81.5 Hz/N to 83.5 Hz/N, an increase of 2.4% (Figure 3.7A). For sensors 1 – 4, the sensitivities from the full osteotomy to half osteotomy states decreased by 44.8%, 35.4%, 34.4%, and 50.8%; respectively (Figure 3.7A). Similarly, sensitivities from half osteotomy to fully intact states decreased by 36.3%, 32.5%, 39.5%, 45.7%, and 25.0% for sensors 1 - 5, respectively (Figure 3.7A).

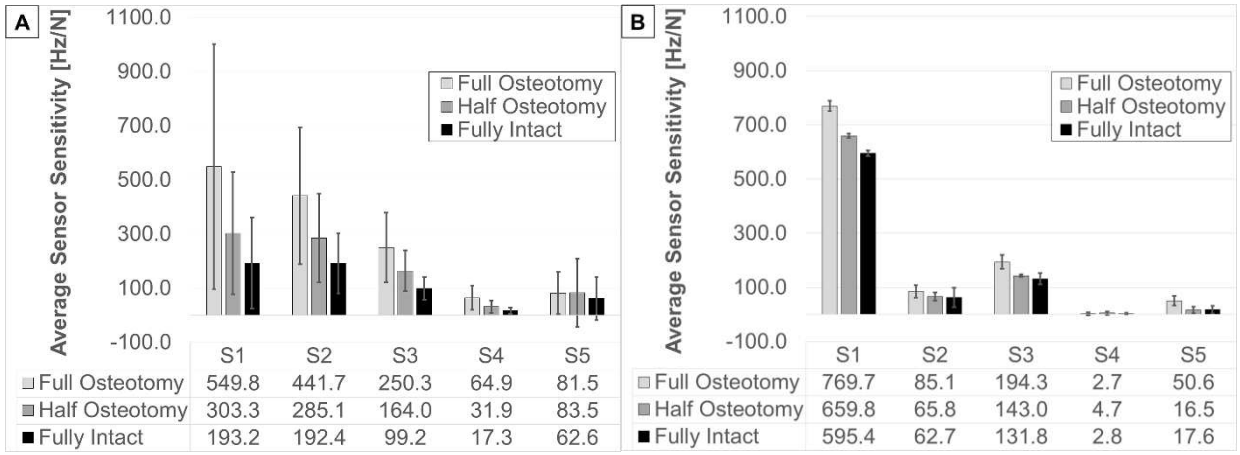

Figure 3.7: (A) Average compiled (n = 9) sensor sensitivities for a five fsBioMEMS sensor-IMN construct during ex vivo simulated bone healing of ovine tibia. The sensors are numbered from proximal (S1) to distal (S5), with S3 located at the IMN mid-span. Based upon an ANOVA with Tukey pairwise comparisons ($\alpha = 0.05$), the full osteotomy state differs significantly from the half osteotomy and intact states ($p = 0.004$) and the mean sensitivity of sensor 1 differs significantly from sensors 3 and 4 ($p = 0.001$). (B) Average sensor sensitivities for a single ovine tibia (n = 5 cycles per fracture state).

An ANOVA statistical test ($\alpha = 0.05$) of the compiled sample averages, indicated statistically significant differences associated with sensor location ($p = 0.001$) and fracture state ($p = 0.004$). Tukey pairwise comparisons ($\alpha = 0.05$) specified the average sensitivity of sensor 1 as significantly different than sensors 3, 4, and 5 ($p = 0.034$, $p = 0.001$, and $p = 0.017$; respectively), while the full osteotomy state showed statistically significant differences from the half osteotomy and intact

states ($p = 0.044$ and $p = 0.004$, respectively). The large variability in grouped sensor sensitivities (Figure 3.7A) was not indicative of the sensitivities observed within single samples (Figure 3.7B).

3.1.4 Discussion

A multi-antenna array was developed which produces antenna-sensor pair RRF responses in discrete, non-overlapping spectral ranges. By utilizing parallel antenna connectivity, and simultaneous measurement of S_{11} (from sensors 1, 3, and 5) and S_{22} (from sensors 2 and 4) data, this array allowed for concurrent measurement of RRF behavior of five antenna-sensor pairs. In addition to increasing the number of fsBioMEMS sensors which can be placed on a single implant, this measurement technique has the auxiliary benefit of reducing the data collection period by 50% without reduction of resolution. The spectra of the new antenna design feature substantially increased Q-factors (relative to the original antenna design) thus allowing for data noise reduction. Enhanced Q-factors are the result of deep and sharp RRF peaks, which has the added benefit of decreasing the total frequency range which must be analyzed for a five-sensor construct. Reducing this range decreases the burden on the network analyzer, enabling further increased data acquisition times which more closely approach real-time measurement.

Analysis of cross-talk indicated deleterious effects induced by the presence of multiple sensors within close proximity to a single antenna. These effects diminished considerably once the second sensor was displaced outside of the projection area of a given antenna. Cross-talk was further observed between two adjacent antennae. Once again, effects were greatest while the antennae projection areas overlapped. Cross-talk effects appeared to be exacerbated in instances of the

antennae having similar operating frequencies. The results of this analysis were utilized to develop an antenna array which focused upon the geometric and spectral relationship between adjacent antenna, with specific regards to eliminating overlap in the projection areas and maximizing the difference in operating frequencies.

Sensor repeatability and tissue attenuation data indicated plausibility in the ability to measure RRF spectra of the sensor-IMN construct *in vivo*; however, the performance of this diagnostic measure could foreseeably vary among certain patients where excessive amounts of tissue intervene between the skin and implant. Tissue attenuation data further highlighted the importance of close proximity between the tissue and antenna during data acquisition due to the high degree of signal attenuation within air.

Measurements from the present study suggest a decrease in load share experienced by implant hardware as fracture stiffness increases. Previous studies have exhibited similar trends through a variety of testing methods including the use of wired external fixators in humans [53] and sheep [60], wired strain gauges on fixation plates in sheep [75], and telemetric assessment of femoral IMN's in humans [69]. These findings are further supported by a previous study by our group, through the use of a single BioMEMS sensor on fixation plates in sheep, which found decreasing implant strain throughout the healing process. Differences in healing types were detectable with this method during early phases of healing [96]. The data of the present study advocate that multi-sensor fsBioMEMS constructs contain the same diagnostic abilities, with the addition of applicability towards contoured implants at multiple locations.

Current clinical early diagnostic tools are limited in their ability to predict the course of fracture healing [30, 37, 39, 42-44, 51]. Healing is typically monitored through the use of temporal radiographs after surgical intervention. However, radiographic imaging suffers from a number of disadvantages, including limited fidelity and patient exposure to ionizing radiation [37]. When interpreted by experienced clinicians, there is a great deal of inter-observer variability in estimating the progress of healing [16, 39, 42]. Furthermore, early radiographs have demonstrated an inadequate ability to properly predict the course of healing [30, 42-44]. Previous studies have aimed to decrease the subjectivity of this diagnostic modality through the use of scoring methods [48] and automated image processing algorithms [118], but these neglect to address the low temporal fidelity of radiographs. Prior studies have established the appearance of calcified tissue (during secondary bone formation) to present radiographically several weeks after healing is indicated by quantifiable changes in the temporal mechanical properties of the periosteal callus [67, 69]. Moreover, radiographic imaging presents little temporal changes in the case of primary bone healing, where healing is slow and no periosteal callus is formed [14]. The need for quantification of the mechanical environment of the fracture implant is motivated by increased temporal fidelity (relative to standard imaging modalities) and the associated dependency between implant loading and fracture healing [21, 60, 75, 99, 100].

3.1.5 Conclusion

The use of fsBioMEMS sensors present clinical potential due to a number of advantageous features, including: their small and flexible nature which allows for efficacious placement on orthopaedic hardware, inductive power allowing for long-term use without the need for power source implantation, and wireless transmission allowing for noninvasive measurements. An added

benefit is derived through the use of sensors on multiple locations of orthopaedic implants. Improvements to the sensing technology to obviate differences in inter-sensor measurement sensitivities would allow for direct comparison of strain at several locations, thus creating a temporal strain profile along the length of the implant. These data could be leveraged as a development tool for the creation of orthopaedic hardware in order to optimize the mechanical environment for bone healing.

3.2 Specific Aim 2

3.2.1 Introduction

The findings of Section 3.1 established the feasibility of fsBioMEMS as a means to noninvasively quantify implant surface strains to indirectly predict fracture stiffness, and thus predict fracture healing outcome. These findings were limited by benchtop and *ex vivo* techniques, thus neglecting many challenges inherent to clinical implementation of new diagnostic tools. Accordingly, two *in vivo* fracture healing pilot studies were initiated to evaluate the efficacy of this technology in a comparative animal model.

3.2.2 Pilot 1: Materials & Methods

3.2.2.1 Fixation Hardware Instrumentation

A 316L stainless steel IMN of 8 mm diameter and 197 mm length (Biomedtrics I-Loc IM Fixator, Whippany, NJ) was utilized for this study to ensure fixation hardware selection consistent with those used in benchtop sensor characterization (Section 3.1). *Ex vivo* pilot studies indicated that during surgical implantation, shear forces are produced on the surface of the IMN as it passes along

the cortical walls of the intramedullary canal; thus, it is necessary that sensors affixed to the IMN be recessed from the surface to prevent their unintended removal during nail insertion. Accordingly, 0.5 mm depth circumferential recesses were machined in the IMN surface to enable fsBioMEMS and biocompatible coatings to be located below the surface of the nail. fsBioMEMS were adhered by cyanoacrylate (Locktite, Düsseldorf, Germany) at even increments of 40.5mm distances along the length of the nail (based upon the placement of sensor 3 at the IMN mid-span), and coated with biocompatible medical grade polyurethane (Master Bond, Inc. Hackensack, NJ) (Figure 3.8). Pilot studies were performed to ensure fsBioMEMS would remain viable after being subjected to standard surgical sterilization techniques.

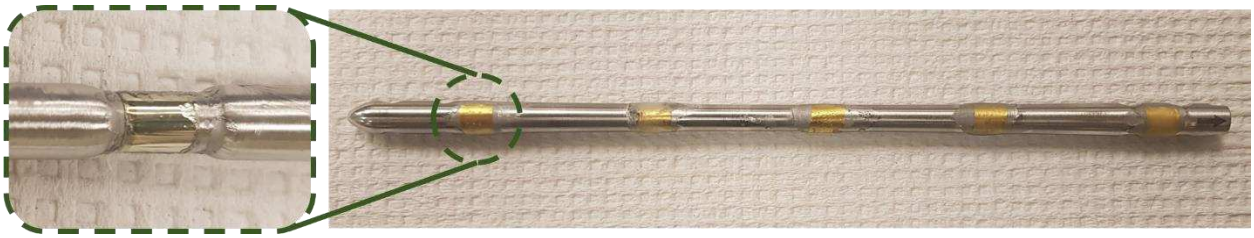

Figure 3.8: Intramedullary nail with five fsBioMEMS adhered to surface. Callout depicts the 0.5mm circumferential recess machined at each sensor location to allow sensors to be positioned below the implant's surface to prevent shear removal during nail insertion.

3.2.2.2 Surgical Model

Two skeletally mature sheep (Rambouillet cross, female, > 3 years of age) were selected for the first pilot study (IACUC approval #19-8990A). Sheep were selected for this experimental model due to their similarity to humans in several facets pertinent to the study of bone healing: body weight, bone macrostructure [119], bone mineral composition, cortical bone microarchitecture, and bone healing rates [120].

According to standard surgical methods, the animals were anesthetized and the surgical site was shorn and sterilized. An incision was made at the anterior aspect of the hoc joint to provide access to the tibial plateau, where a hole was drilled into the tibial intramedullary canal at the central axis of the bone. The proximal aspect of the intramedullary canal was then reamed and the instrumented IMN was inserted such that the middle sensor was located at the diaphyseal midspan of the tibia, and the sensors' orientation pointed to the posterior of the limb. An aiming jig arm was utilized to guide the insertion of two transverse locking bolts to anchor the IMN at its proximal and distal ends (four total bolts) using standard orthopaedic techniques. An incision and osteotomy were then created at the diaphyseal midspan by removing an approximately 10 mm length of bone by an oscillating bone saw (Figure 3.9). 10 mm was selected for this pilot study as previous studies have shown this osteotomy size to result in nonunion in ovine fracture models [96]. Skin and soft tissue were then sutured closed according to standard surgical techniques. The animals were not casted and allowed free ambulation upon recovery. All animals were sacrificed after 12 weeks post-surgery, at first sign of hardware failure, or upon radiographic appearance of boney union; whichever event first occurred.

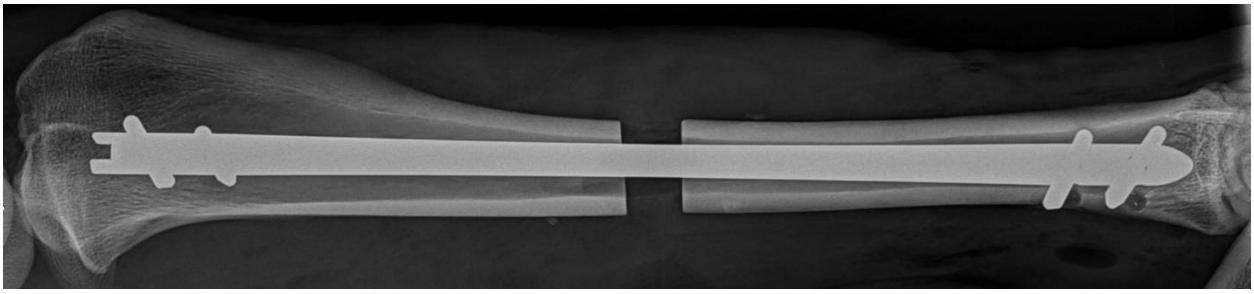

Figure 3.9: Medial-lateral planar x-ray image of the ovine tibial osteotomy fracture model treated by an intramedullary nail instrumented with five fsBioMEMS. A 10 mm mid-diaphyseal osteotomy was surgically induced to create a nonunion fracture healing model.

3.2.2.3 In Vivo Data Collection

Animal testing was composed of weekly biplanar radiographic imaging and twice-weekly biomechanical analysis. Biomechanical analysis consisted of measuring fsBioMEMS RRF shifts as the limb was subjected to four-point bending. Four-point bending was selected as the loading procedure as this obviates the need to apply loads directly to the healing osteotomy site (Figure 3.10A) and induces constant bending moment, without shear forces (Figure 3.10B), when the fracture site is located between the inner bending points. The mechanical advantage inherent to this loading method ensures that implant bending strains are developed while minimizing the compressive forces which must be applied to the fractured bone (Figure 3.10C).

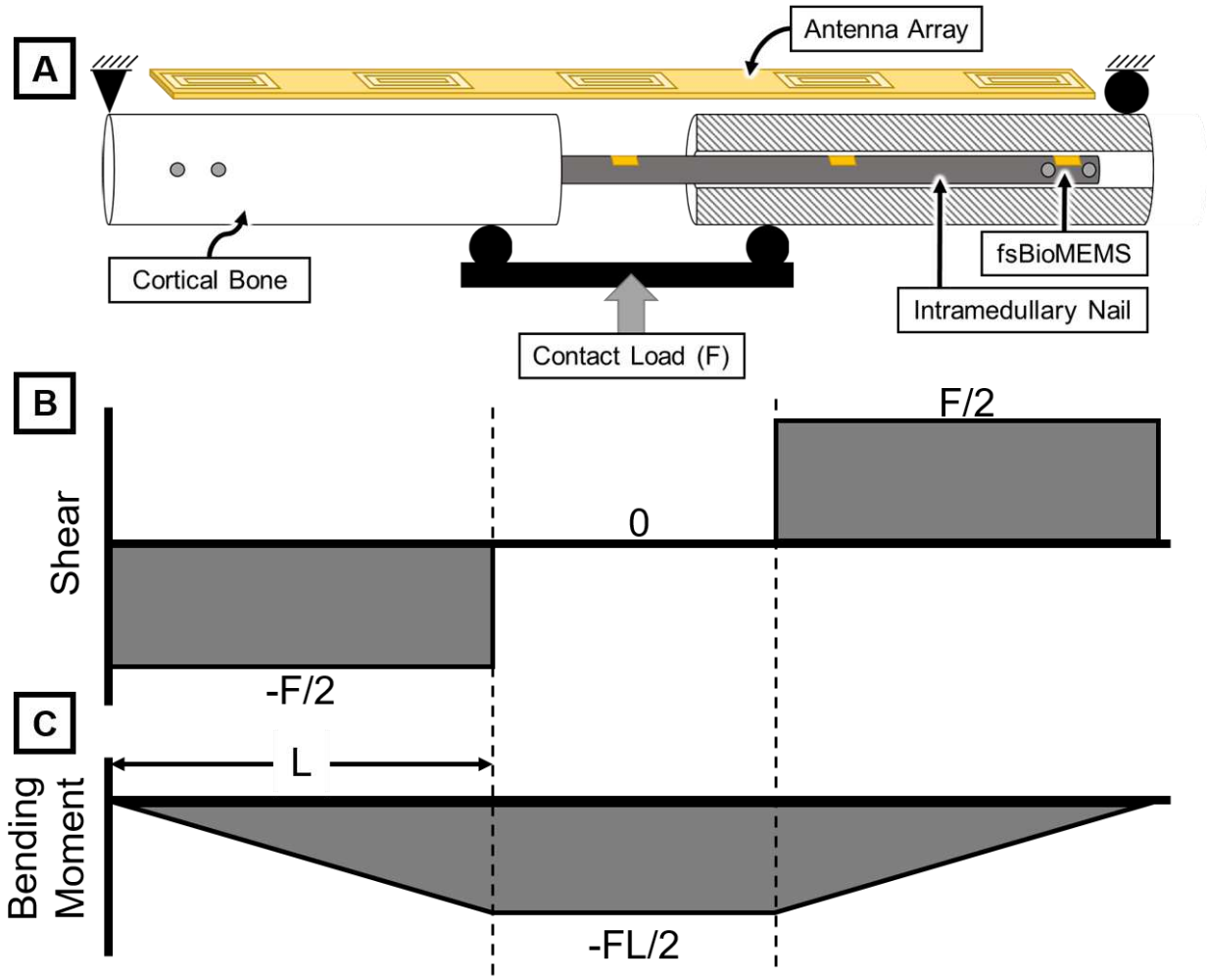

Figure 3.10: A) Graphical representation of the symmetric four-point bending methods employed to produce implant surface strains, measured by fsBioMEMS sensors, without direct load application to the osteotomy fracture gap. B) Four-point bending ensures minimal shear loading within the fracture tissues when the inner bending contact points are positioned on opposite sides of the fracture gap. C) Bending moment is constant within the fracture gap (i.e., between the inner bending points). The distance between the outer and inner bending contact points (L) provides mechanical advantage to produce increased bending strains while minimizing the necessary compressive contact load (F).

A custom loading fixture was designed to apply four point bending via manual operation of a lead screw actuator while simultaneously positioning the five antenna array (see Chapter 3.1 for antenna development) aligned with the fsBioMEMS on the tensile side of bending. Contact force generated by the lead screw actuator was measured via 6 DOF load cell (AMTI MC3A-100; AMTI; Watertown, MA), which was used to calculate the induced bending moment according to

the geometry of the loading fixture (Figure 3.10C). Data was collected by positioning the animals in lateral recumbency while placing the four-point loading-antenna construct on the treated tibia such that the fracture site was centered between the inner two bending points and the antennae array was aligned with the fsBioMEMS sensors on the posterior aspect of the limb (Figure 3.11).

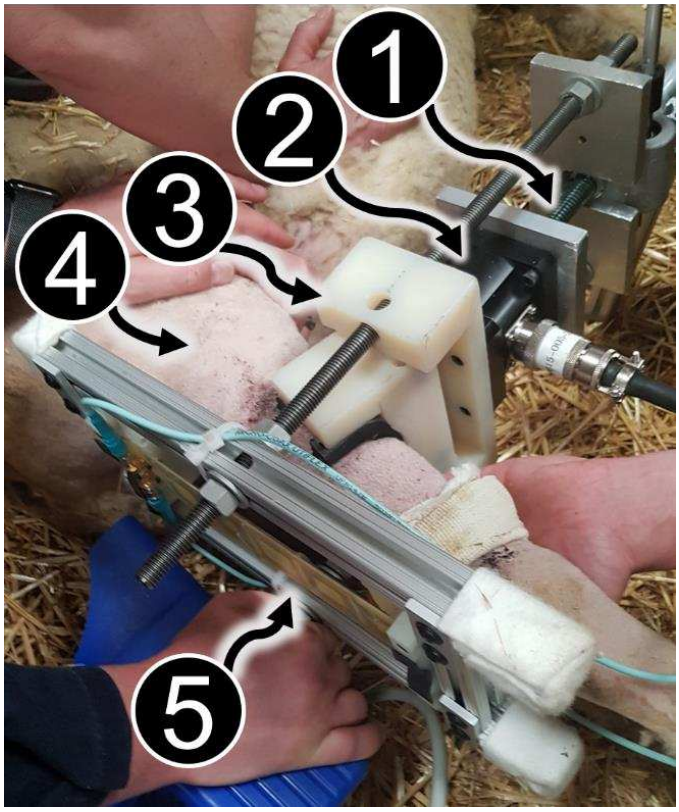

Figure 3.11: Custom loading fixture designed for inducing four-point bending and positioning antenna array. 1) Manual lead screw actuator for creating contact forces. 2) Load cell measures applied contact forces. 3) Load is applied to pivoting middle two bending points to ensure even contact thus preventing accidental application of three-point bending. The fracture site is located between the inner bending points. 4) Tibia with mid-diaphyseal osteotomy treated by fsBioMEMS instrumented IMN. 5) Five antennae array aligned with the internal fsBioMEMS.

Bending moments were cyclically applied to the limb (0.5-1.5 N-mm, in 0.25 N-mm increments) as RRF shift versus load was collected. To minimize effects from soft tissue compliance, the limbs received five preconditioning loading cycles followed by five cycles in which data was collected.

Data collection was repeated for loading cycles in which the animal moved the treated limb during testing. Linear regressions were applied to the RRF shift-load curves for each test and antenna; the sensitivity for each antenna was calculated as the average slope for all loading cycles during the testing session. Antenna sensitivity rate of change during the initial stages of healing was calculated as the slope of a linear fit applied to the antenna sensitivities during the first 30 days post-fracture.

3.2.3 Pilot 1: Results

Premature implant failure occurred in both animals within the first two weeks post-fracture, thus resulting in early study termination and prevention of meaningful *in vivo* biomechanical data collection.

3.2.4 Pilot 2: Materials & Methods

The IMN utilized in the previous pilot study has frequently been implemented in comparable fracture models without hardware failure; therefore, it was concluded that the small reduction to the IMN diameter was responsible for the implant failure. A second pilot study was later initiated with methods modified for risk mitigation. IMN were instrumented with fsBioMEMS according to the methods described in Section 3.2.2.1, however the IMN surface was not machined for this study. Consequently, the surface of the instrumented IMN was non-uniform due to the presence of the polyurethane coated sensors (Figure 3.12) which generated the risk of inadvertent sensor removal during insertion of the nail into the intramedullary canal. This likelihood was reduced by over-reaming the intramedullary canal prior to nail insertion. Possibility of hardware failure was

further reduced by placing a hard sleeve cast over the treated limb post-operatively to protect the limb from lateral trauma. The cast was used for the first three weeks post-surgery, but was temporarily removed while performing weekly data collection. Excluding the amendments noted in this section, all methods pertaining to hardware instrumentation, surgical model, and *in vivo* data collection remained the same as first pilot study (Section 3.2.2).

Figure 3.12: Structurally unmodified IMN instrumented with five fsBioMEMS. The lack of surface modifications caused polyurethane coated sensors to protrude from the implant's surface.

3.2.5 Pilot 2: Results

Pilot Animal 1 was sacrificed at seven weeks post-fracture upon indications of potential bolt hardware loosening. There were no radiographic indications of fracture site calcified tissue formation at animal sacrifice (Figure 3.13). Pilot Animal 2 was sacrificed at 12 weeks post-fracture and exhibited visual radiographic indications of initial callus formation without achieving full fracture union (Figure 3.13).

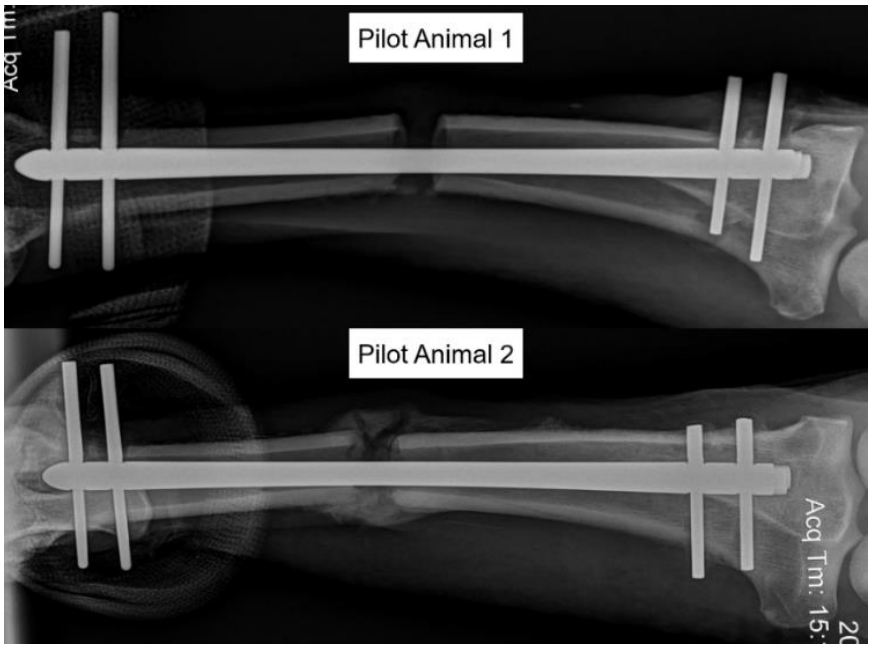

Figure 3.13: Cranial-caudal planar radiographic of fracture healing progress at animal sacrifice. Pilot Animal 1 was sacrificed at seven weeks post-surgery to mitigate potential traumatic hardware failure due to indications of loosening at proximal locking bolts. Pilot Animal 2 was sacrificed at study termination, 12 weeks post-fracture.

The temporal profiles for each antenna, as measured for both pilot animals, are provided in Figure 3.14. For Pilot Animal 1, antenna sensitivity rate of change during the initial stages of healing (i.e., the slope of a linear regression applied to data within the first 30 days of Figure 3.14) were -0.02, -0.03, -1.06, 0.01, and 0.09 MHz/N-m per day; for Antenna 1 through Antenna 5, respectively (Figure 3.14A). Pearson's correlation coefficients (R^2) for these linear regressions were 0.03, 0.19, 0.26, 0.07, and 0.03; respectively. For Pilot Animal 2, Antenna 1 through Antenna 5 antenna sensitivity rate of change during the initial stages of healing were -0.26, -0.04, -0.09, -0.05, -0.38 MHz/N-m per day; respectively (Figure 3.14B). Pearson's correlation coefficients for these linear regressions were 0.02, 0.02, 0.12, 0.26, and 0.19; respectively.

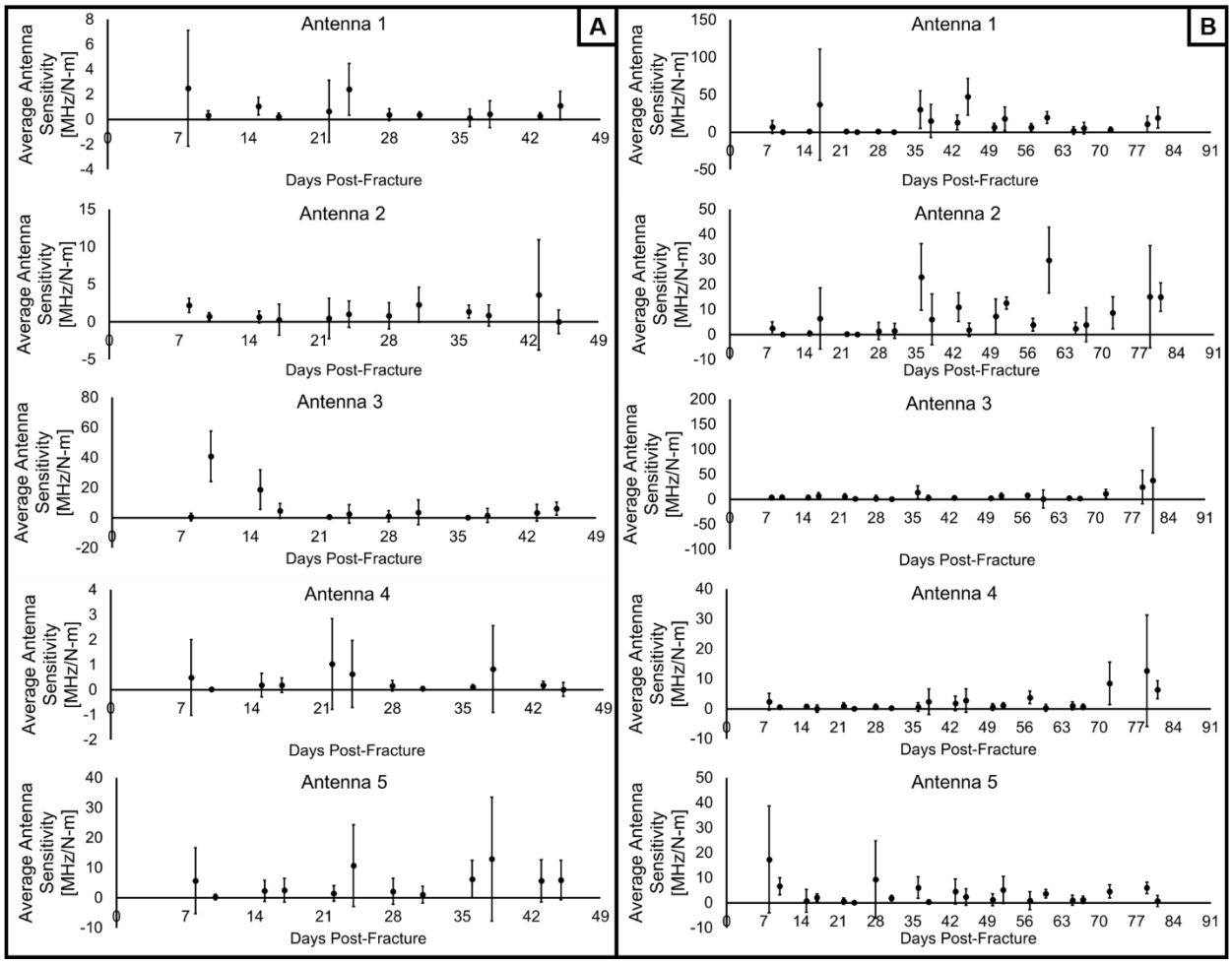

Figure 3.14: Temporal antenna sensitivity profiles for A) Pilot Animal 1 & B) Pilot Animal 2. Error bars represent the standard deviation of each testing session's replicate antenna sensitivity measurements (n = 5 tests performed per testing session). Antennas 1 and 5 correspond to the fsBioMEMS located between the proximal and distal locking bolts, respectively, while antenna 3 corresponds to the fsBioMEMS located at the osteotomy fracture site.

3.2.6 Discussion

Visual inspection of the radiographic data indicate that Pilot Animal 2 progressed through sufficient fracture healing to form a soft callus and small amounts of calcified bone, while Pilot Animal 1 exhibited no radiographic indications of healing (Figure 3.13). The fracture stiffness of Pilot Animal 2 is thus hypothesized to have decreased throughout the study, while Pilot Animal 1 remained relatively constant. By extension, it is anticipated that the IMN surface strains for these animals would have decreased and remained elevated; respectively. The antenna sensitivities for

both pilot animals did not present clear temporal progression during the early stages of healing as evidenced by poor agreement between linear regressions and experimental data within the first 30 days of fracture healing (mean $R^2 = 0.12 \pm 0.09$). These findings do not agree with previous studies in which temporal progression of rigid substrate BioMEMS' sensitivities were highly linear during the early stages of healing for both proper and aberrant fracture models, as demonstrated by observed Pearson's correlation coefficients exceeding 0.95 [96]. Temporal reduction in implant surface strains throughout fracture healing have been well established in previous studies [69, 78, 96], thus the lack of temporal progression in the present data are indicative of poor performance of the fsBioMEMS rather than issues with the underlying assumption that implant surface strain indicate healing state.

For the five replicate measurements within a single *in vivo* biomechanics testing session, the standard deviation of measured antenna sensitivities exceeded their mean value in 81.6% and 49.0% of cases for Pilot Animal 1 and Pilot Animal 2, respectively. These large daily variances observed in the data are indicative of poor signal connection between the antennas and the fsBioMEMS. Post sacrifice removal of the IMN indicated several sensors to have become loose from the hardware. Data quality could have been further degraded by the muscular effects observed in previous studies where the volume of muscle [80] and their application of forces to the fractured bone [78] had deleterious effects on data collection.

Challenges associated with low testing repeatability and the absence of temporal patterns in BioMEMS data during early healing were not observed in previous *in vivo* implementation of

plates instrumented with rigid substrate BioMEMS for treatment of metatarsal factures [96]. This advocates two theories: the rigid substrate provides a better medium for conversion of mechanical strain to quantifiable electromagnetic resonance properties, or differences in the fracture and/or testing methods of the two studies (i.e., plated metatarsal versus IM nailing of tibiae) somehow reduce the efficacy of BioMEMS sensors. The bone selection for this fracture model presented substantial challenges due to anatomical differences in the tibia of sheep versus humans. Unlike humans, sheep tibia are positioned close to their abdomen which makes it difficult to apply bending loads to the bone without manually extending the limb at the stifle joint (Figure 3.11). This tended to agitate the animal leading to muscle contractions and movement during data collections. Furthermore, this close positioning of the limb relative to the abdomen prevented optimal positioning of the loading fixture and antenna array which ultimately created a relatively large distance between the antenna array and the limb. Suboptimal antenna positioning ostensibly had deleterious effects on antenna-sensor coupling based on the findings of previous studies which have shown the signal from fsBioMEMS to be highly attenuated through large air gaps (Chapter 3.1.3.1).

Additional challenges with this fracture model can be attributed to the use of intramedullary nails. Despite repeated successful implementations of the selected IMN in previous unrelated studies of comparable fracture type, the slight modifications to the nail geometry produced hardware failures resulting from reduction of mechanical integrity and introduction of stress concentrations. While this may be attributable to non-existent patient compliance in an ovine model leading to postoperative over-loading events, the outcome is unacceptable and must be diligently avoided. Similar trauma has been observed in human clinical trials using fixation plates modified for

telemetric instrumentation [69]. For this study, implementation of modified IMN with improved structural properties (i.e., using IMN of larger diameter) was precluded by the narrow intramedullary canal and the varus bowing profile of ovine tibiae; however, changing the IMN material selection from 316L stainless steel to another orthopaedic alloy, such as titanium Ti-6Al-4V, would offer an improvement in yield strength [121] and comparable fatigue resistance [122]. The results of this study therefore suggest that modified IMN cannot be implemented in this fracture model due to severe safety concerns, but unmodified IMN are equally as infeasible due to the severe risk of inadvertent sensor removal during implantation.

3.2.7 Conclusion

The data from these initial pilot studies indicate substantial obstacles which fsBioMEMS must surmount prior to further studies for Specific Aim 2, let alone clinical implementation. The current fracture and treatment model necessitate hardware modification or considerable risk of incidental sensor removal during surgical hardware implantation. None of these options are favorable as hardware modification and over-reaming of the intramedullary canal exhibit increased likelihood of traumatic implant failure, and sensor removal during implantation represents subsequent loss of data and biocompatibility risk from sensor migration. Furthermore, the current fracture model presented additional complications to *in vivo* biomechanical evaluation due to inherent differences in the tibial anatomy of sheep relative to humans. Thus, the findings of this pilot study indicate that use fsBioMEMS on IMN, especially in the ovine tibia, is not feasible. This conclusion advises returning to the plated metatarsal fracture model; however, this model may be equal as problematic for simultaneous of testing multiple fsBioMEMS sensors. While the flexible substrate of the fsBioMEMS allow their application to contoured topographies, they must be applied directly to

the implant surface and thus cannot be placed over the screw holes of a plate. Custom plate designs would thus be necessary to accommodate multiple fsBioMEMS sensors. The short length of the ovine metatarsal ensures that a metatarsal fracture plate would only accommodate an appreciably reduced number of screws after modifications were made to house multiple fsBioMEMS sensors. Such a design would reduce clinical safety due to the high risk of traumatic implant failure resulting from a single screw loosening or failure event. In conclusion, the findings of this chapter advise a technology redesign to establish a new means to quantify healing fracture stiffness without the need for implant modification or instrumentation.

CHAPTER 4: COILED COAXIAL DEC ANTENNA DEVELOPMENT (SPECIFIC AIM 1 & SPECIFIC AIM 2)[2]

The severe limitations of the fsBioMEMS observed in Chapter 3.2 suggested the need for considerable improvement to the fracture model and diagnostic technology to account for challenges associated with failure of modified implant hardware and unintended sensor removal during hardware implantation. Incidentally, work by Labus et al. at this time was beginning to suggest that orthopaedic hardware deflections produced by mechanical loading could also be quantified using noninvasive electromagnetic measurement techniques [97]. This chapter details the development of an initial design iteration of this technology to address Specific Aim 1 and Specific Aim 2. The findings of this chapter have been published [123] and were subsequently used to advise additional technological iteration, as detailed in Chapter 5 and Chapter 6.

4.1 Introduction

Failed bone fracture healing (nonunion) yields substantially harmful effects on patients' wellbeing including the need for additional orthopaedic surgeries, increased duration of outpatient physical therapy, onset of chronic pain, extended opioid therapy duration, increased likelihood of strong opioid prescription, and 118% increase in reported treatment costs [11, 12]. Reported rates of nonunion vary according to fracture location, severity, treatment type, and patient-specific risk factors; however, nonunions are especially prevalent among long bone fractures such as the tibia where up to 12% of fractures are reported to experience nonunion [11]. Early diagnosis of aberrant

[2] This chapter has been published in *Annals of Translational Medicine* (DOI: 10.21037/atm-21-1853) [123]. All contents are publically available via Creative Commons, but have been republished with permission from Copyright Clearance Center, Inc.: Wolynski, J.G., et al., *Diagnostic prediction of ovine fracture healing outcomes via a novel multi-location direct electromagnetic coupling antenna.* Annals of Translational Medicine, 2021. **9**(15).

fracture healing is imperative as early intervention will allow clinicians to implement adjunct therapies much earlier in the healing cascade to meaningfully reduce patient suffering and the associated economic burden [9, 13].

Bone is an exceptionally resilient tissue owing to its ability to repair without the formation of chronic scar tissues. Fracture healing is generally characterized by overlapping phases of inflammation, repair, and remodeling [17, 18]. The inflammatory phase begins at the onset of bone fracture which causes blood vessel rupture ultimately leading to the formation of a hematoma at the fracture site [17, 19]. Following inflammation, fracture repair occurs through endochondral and/or intramembranous ossification, depending on the mechanical environment of the fracture site [17] which is influenced by clinical fixation [124] and rehabilitation techniques [125]. Intramembranous ossification is characterized by direct formation of woven bone to bridge the fracture gap, and tends to be limited to rigidly stabilized reduced fractures [20] experiencing small magnitudes of strain [21] and interfragmentary motion [17]. Alternatively, endochondral ossification occurs when the fracture site is subjected to moderate strains [21] and interfragmentary motion [17]. Endochondral ossification involves the formation of intermediate soft callus tissues, composed of cartilaginous and granular tissues, which are subsequently resorbed after becoming calcified [22]. Fracture nonunion occurs when a cessation of this biological progression occurs prior to successful boney bridging of the fracture gap [23], and can result from infection or deficiency in the mechanical or biological environment of the fracture site [25, 28, 29]. The complex biomechanical regulation of fracture healing [126, 127] and numerous patient comorbidities which may inhibit fracturing healing [128] makes clinical prediction of fracture repair outcome and arduous task.

Clinical diagnosis of nonunion remains a slow process, requiring on average 6.2 months to diagnose with current clinical approaches [16]. Much of this delay can be attributed to the standard diagnostic use of planar x-ray imaging which remains highly qualitative and subjective [14, 16, 40, 45, 109], thus increasing the difficulty to predict fracture union state during the early stages of healing (< 30 days). This results in a 50% probability of x-ray imaging correctly diagnosing the correct stage of fracture healing [30] and facilitates restricted ability to forecast the occurrence of delayed- and non-unions [42, 43]. Furthermore, x-ray imaging has exhibited poor performance as a means to predict the mechanical stiffness of the healing fracture [42, 45, 67], which is a vital metric for patients' safe weight-bearing and return to normal daily activity. Fracture stiffness is often addressed by manual manipulation of the fracture site to qualitatively determine fracture stability; however, this technique remains subjective and thus is limited by clinician interpretation [51].

Despite the inability to be quantified by x-ray imaging, fracture stiffness shows promise as an effective means to diagnose and predict fracture healing outcome [23, 58, 61, 75, 96]. Previous studies have shown that mechanical load is temporally shifted from orthopaedic fixation hardware (i.e., plates, intramedullary rods, or external fixation) to the bone [23, 58, 60, 61, 75, 76, 96] as healing progresses. Due to morphologic changes at the fracture site (i.e., the formation and remodeling of the fracture callus) which precede tissue mineralization, quantification of fracture site stiffness has shown the ability to accurately predict healing outcome prior to radiographic diagnosis [75, 96]. Studies have also shown that during acute healing (< 30 days) fractures progressing to proper union will exhibit progressive improvement of mechanical strength, while

this progression of increased fracture site stiffness is arrested and/or delayed in fractures trending towards nonunion [96].

While biomechanical quantification of fracture site stiffness has shown capacity as an early diagnostic of fracture healing outcome, there are currently no noninvasive techniques to perform this measurement in a clinical setting. Previous research groups have performed this analysis using wired strain gages on orthopaedic plates [75, 76], instrumented external fixators [53, 60, 61, 64, 66, 68], and plates instrumented with telemetric sensors [69]; however, these techniques are respectively limited by the potential for infection, limited hardware application, and long-term biocompatibility concerns. To address this clinical deficit, our research group previously developed wireless implantable microelectromechanical sensors (bioMEMS) capable of quantifying, via external antenna, temporal changes to the mechanical strain on implanted orthopaedic hardware [82, 83, 87, 92-96, 98, 111]. In a previous study, temporally repeated bioMEMS measurements detected statistically significant differences in normal and aberrant bone healing in an ovine fracture model in as few as 21 days post-fracture [96], and use of flexible bioMEMS enabled sensor application to most types of orthopaedic hardware [98]. Despite the demonstrated promise of these bioMEMS technologies, clinical translation of these sensors remains challenging as their implementation required implant modification to attach and protect the sensors during surgical implantation. These implant modifications, while minor, resulted in associated additional regulatory hurdles to achieve clinical applicability.

To address these limitations, our research group has developed a diagnostic system capable of measuring temporal changes in the relative fracture callus stiffness for any fracture treated with standard off-the-shelf orthopaedic hardware stabilization devices, without the need to modify

existing hardware design [129]. This diagnostic relies upon fractures with orthopaedic implant fixation behaving as a composite structure, where stiffness of the healing fracture tissues and the implanted hardware both contribute to the stiffness of the composite structure. Since it can be assumed that the implant's stiffness remains constant during healing, changes to the stiffness of the healing fracture site yields quantifiable changes to the stiffness of the bone-implant composite. Our research group has developed a diagnostic device which quantifies this stiffness by applying a physiologic non-detrimental mechanical load to the fracture site (i.e., stabilized bone) while measuring the induced deflection of the fixation hardware via direct electromagnetic coupling (DEC) with an external antenna [97]. Succinctly, the external telemetric DEC antenna electromagnetically couples with the implanted hardware positioned in its near-field region, resulting in an apparent resonant frequency (ARF, in the MHz range) which shifts with changing distance between the coupled members. Thus, measuring ARF shifts during controlled mechanical loading provides a noninvasive means to indirectly measure the stiffness of a fracture treated by any existing metallic orthopaedic implant. Theoretically, temporally repeated DEC measurements can thus indicate if proper healing progression is occurring, as indicated by temporally increasing relative fracture stiffness, or if healing progression has slowed or stopped, as indicated by invariant fracture stiffness prior to fracture union.

We hypothesized that DEC would enable early diagnosis and prediction of aberrant fracture healing by detecting differences in relative fracture stiffness progression during the first 30 days of the healing cascade. In this study we developed a DEC antenna array capable of measuring the displacement of orthopaedic hardware at multiple discrete locations to better characterize the mechanical stiffness of a healing long bone fracture. The efficacy of this diagnostic device was

first tested by *in vitro* simulation of a healing long bone fracture treated by orthopaedic plating. These experiments culminated in an *in vivo* large animal fracture healing model in which the DEC diagnostic device was tested on critical and non-critical ovine fractures treated by orthopaedic plating.

The following article is presented following the ARRIVE reporting checklist (available at https://dx.doi.org/10.21037/atm-21-1853).

4.2 Materials and Methods

4.2.1 Study Design

The purpose of this study was to develop a novel technology to diagnose and predict bone fracture healing outcome. The efficacy of the technology was initially evaluated in fracture healing simulated by the progressive destabilization of cadaveric ovine metatarsals. This experiment served to provide initial validation of the DEC technology while minimizing unnecessary loss of life for *in vivo* experimentation. Tissues for this cadaveric experiment were obtained from animals sacrificed for unrelated studies. The results of the initial cadaveric experiments justified progression to an *in vivo* comparative fracture model where the efficacy of the DEC technology in a more clinically translatable setting could be evaluated. A pilot study was performed to provide initial data for power analysis to determine the appropriate sample size such that sufficient statistical power could be achieved while minimizing animal use. Two fracture models (n = 4 animals per group) were implemented to simulate proper or delayed fracture healing according to the size of the surgically induced osteotomy. The animals were evenly and randomly divided

between the two fracture models by an individual who was impartial and blinded to the study. Power analysis of the primary data of interest, the rate of change of DEC antenna sensitivity during early fracture healing, indicated the initial sample size was sufficient to produce statistically significant differences ($p < 0.05$) with a power value exceeding 0.99; thus, no additional animals were included in this study. DEC sensitivity values were measured weekly throughout healing, with five replicate data collections performed and averaged within each testing session to minimize the occurrence of outlier data points. Experimentation was not performed in a blinded fashion due to readily apparent visual differences in the treated limbs indicating differences in fracture model. Environmental confounders were not controlled. Experimental data points were only removed in the event of gross experimental error.

4.2.2 DEC Antenna Sensitivity to Orthopaedic Implant Deflections

A dipole antenna was created by aligning two identical 2 meter coaxial cables (141-2MSM+; Mini-Circuits; Brooklyn, NY) and electrically connecting their shielding elements near their connectors. The coaxial cables were placed parallel to one another, with approximately 3 mm separation, in a straight line along a non-conductive surface. The end of one cable was connected to a vector network analyzer (VNA) (TTR500; Tektronix; Beaverton, OR) by a coaxial lead cable (Micro-Coax UTIFLEX; CarlisleIT; Pottstown, PA) which measured the reflection coefficient, defined as the ratio of power returned and power supplied to that port (S_{11}, dB), over a range of electromagnetic frequencies (10 - 500 MHz). ARF was measured as the frequency at which S_{11} minima occurred; ARF occurred harmonically at increasing frequencies. The baseline ARF of a given harmonic was measured prior to introducing a stainless steel plate (120 x 20 x 10 mm) on the free end of the dipole antenna (away from the connection to the coaxial lead cable). The ARF

was then measured as the plate was moved along the length of the antenna in 2 mm increments. Antenna locations of maximum DEC sensitivity were determined to be the sites where introduction of the plate resulted in the largest difference in ARF, relative to the baseline ARF (Figure 4.1). This analysis was repeated for the first 11 odd antenna harmonics. The cable was then coiled to align three locations of maximum DEC sensitivity to improve sensitivity in a focused area [97], creating a coiled antenna construct (Figure 4.2A).

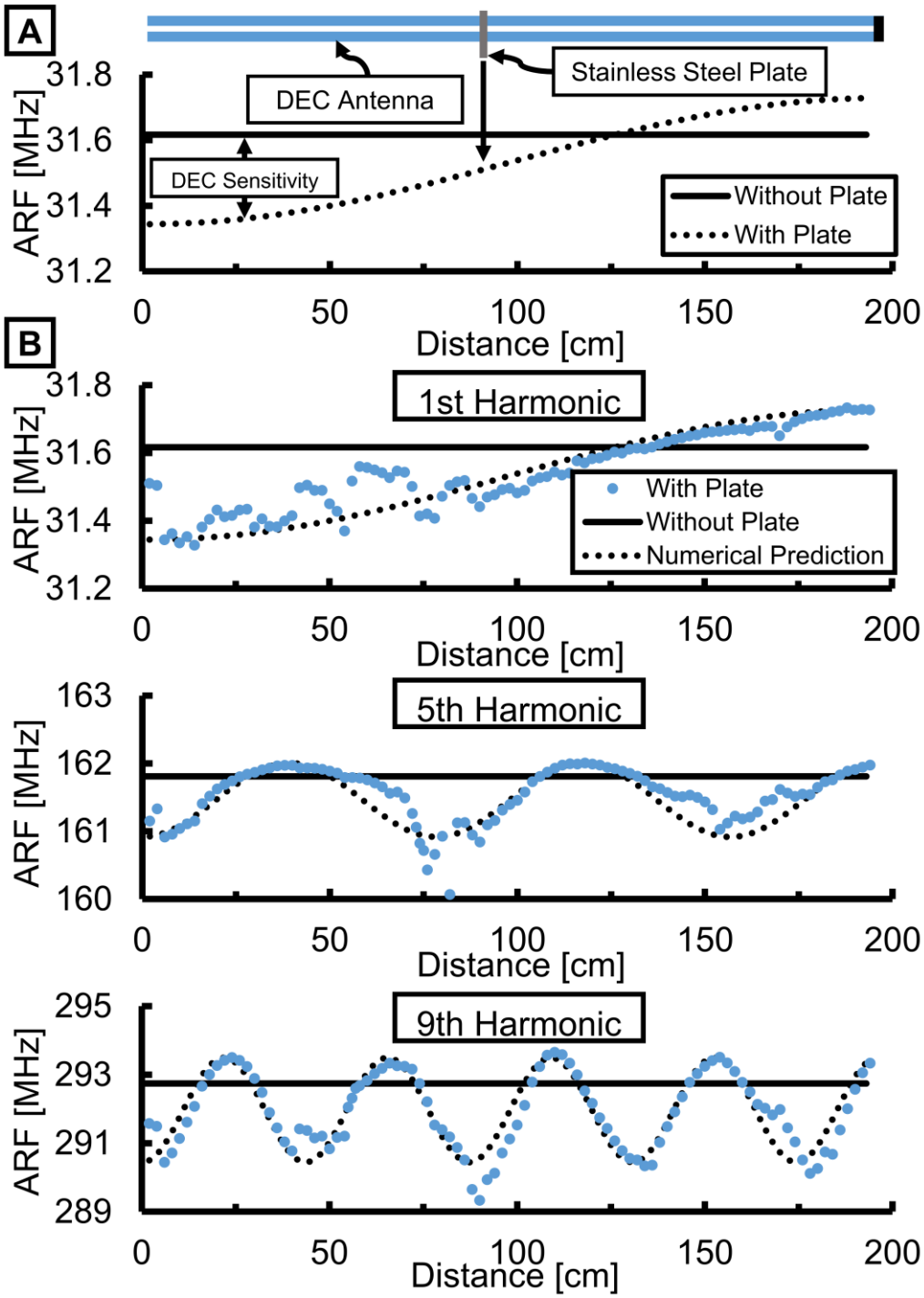

Figure 4.1: Direct electromagnetic coupling (DEC) sensitivity as a function of antenna location. (A) Experimental setup to determine dipole antenna sensitivity to orthopaedic plate proximity at various locations along the antenna's length. DEC sensitivity is found as the difference between the apparent resonant frequencies (ARFs) measured with and without the plate at a given location along the antenna's length. (B) Experimental results for the first, fifth, and ninth ARF harmonics. Each harmonic illustrates a quantity of locations of maximum DEC sensitivity equal to (harmonic number + 1)/2. Dashed line represents a numerical prediction of ARF defined by Equation 4.1.

4.2.3 DEC Antenna Array Sensitivity to Cross-Talk

Simultaneous DEC measurement at multiple discrete locations may provide clinically useful data. For example, multi-location measurements may provide useful information in cases of complex fracture types where multiple orthopaedic implants may be utilized on the same bone. To create a diagnostic antenna capable of measuring in multiple discrete regions, it was necessary to produce an array of multiple antennas. The array was selected to feature three individual antennas to facilitate discrete DEC measurements of the proximal, midspan, and distal thirds on a long bone. Three antennas were produced and stacked so that their DEC regions of sensitivity aligned linearly. A series of experiments were performed to select the antenna designs, including measurement harmonic numbers, so that changes to the DEC coupling distance in one antenna would elicit little to no effect in the ARF of the other antennas (i.e., cross-talk). A custom testing fixture was designed to enable three stainless steel plates, of combined dimensions comparable to one orthopaedic fixation plate (40 x 20 x 10 mm, per plate), to be individually displaced by precision linear actuators (T-LLS105; Zaber Technologies; Vancouver, BC, Canada) to independently alter the DEC coupling distance of each antenna in the array (Figure 4.2A). The distance between each plate and antenna were sequentially increased (0.0-2.0 mm, 0.2 mm increments) while measuring the ARF of each antenna in the array. ARF of the proximal and distal antennas were measured using S11 and S22 measurements, respectively, from a two port VNA (R&S ZVB4; Rhode & Schwarz; Munich, Germany; 1,000 linearly spaced frequency measurement points spanning 20 MHz window centered upon initial ARF; 10 dBm supplied power) while ARF was measured via S11 of a second VNA (Tektronix TTR500; 500 linearly spaced frequency measurement points spanning 10 MHz window centered upon initial ARF; 10 dBm supplied power). Experiments were conducted with parametrically differing designs for each antenna until a design exhibited minimal

change in antenna ARF when the DEC coupling distance was changed for an adjacent antenna (i.e., the ARF of each antenna would only change if the coupling distance was changed for that specific antenna). A set of antennas designed for measurement at the 25th harmonic exhibited this behavior and were utilized for more thorough follow up tests.

4.2.4 DEC Antenna Array Sensitivity to Orthopaedic Plates

To further investigate the sensitivity of the final DEC antenna array, an orthopaedic locking compression plate (LCP; VP4045.09; DePuy Synthes; Warsaw, IN) was fixed to a precision linear actuator. Cadaveric ovine skin was sutured over the LCP to replicate the plated ovine metatarsal used in subsequent *in vitro* and *in vivo* studies. The plate was centered along the length of the antenna array so that each individual antenna measured approximately 1/3 of the orthopaedic plate (Figure 4.2B). The plate was incrementally displaced (0-20 mm, 0.01 mm step size) from the array as the ARF from each antenna was measured. For all data collection henceforth, ARF of the proximal and distal antennas were measured using S11 and S22 measurements, respectively, from a two port VNA (R&S ZVB4; response measured from 805-825 MHz via 1,000 linearly spaced points; 10 dBm supplied power) while ARF was measured via S11 of a second VNA (TTR500; response measured from 830-840 MHz via 500 linearly spaced points; 10 dBm supplied power). ARF values were collected using a custom data acquisition program (LabVIEW 2018; National Instruments; Austin, TX).

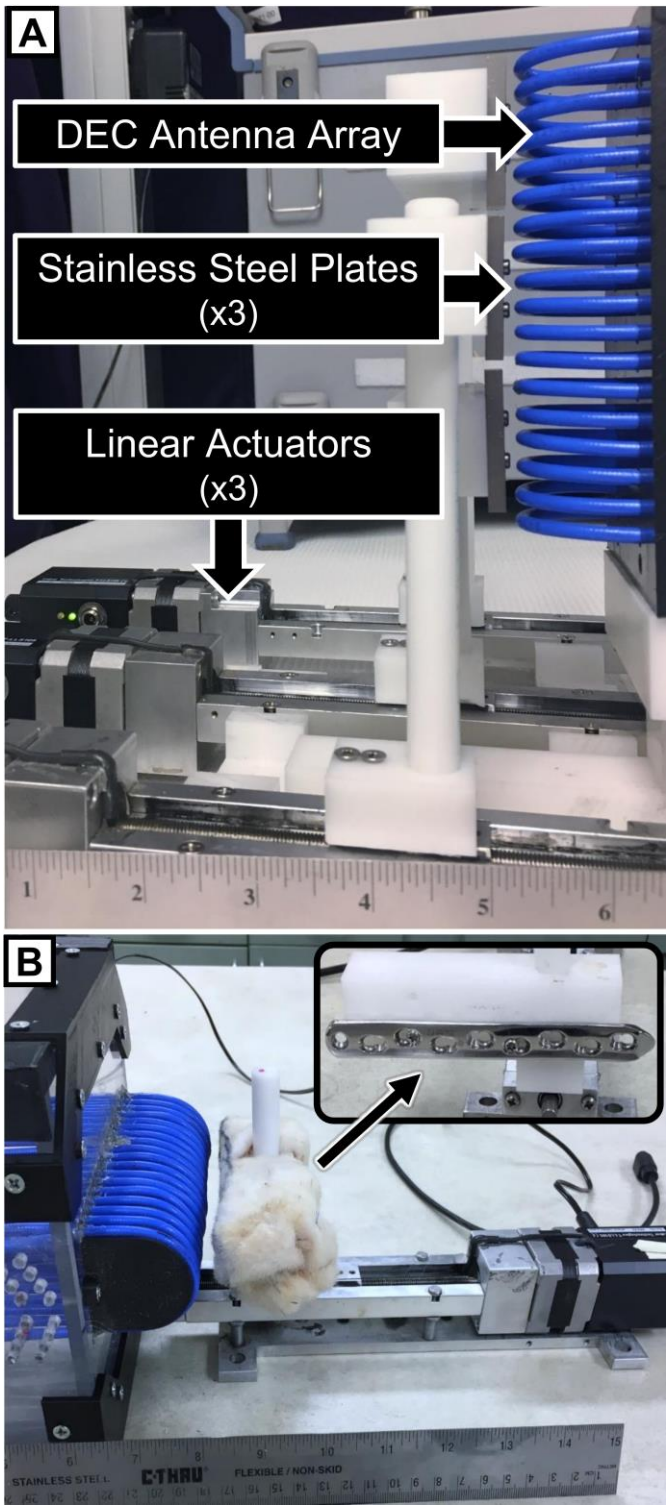

Figure 4.2: Multi location direct electromagnetic coupling (DEC) antenna array sensitivity at discrete locations. (A) Experimental setup in which linear actuators were used to increase plate-antenna displacement at a single antenna location (i.e., one third of the antenna array) while interrogating the response from all three antenna locations. (B) Experimental setup to evaluate antennnae sensitivity to orthopaedic plate displacements, as produced by precision linear actuators, in the presence of physilogic tissues.

4.2.5 DEC Differences in Cadaveric Fractures of Varying Stiffness

A custom DEC-loading fixture was designed to enable the application of mechanical four-point bending to a long bone with orthopaedic hardware fixation, thus inducing implant deflection towards the DEC antenna array discussed in the previous section (Figure 4.3). Four-point bending was selected for this application as it allows the fracture site to be placed between the inner bending points to avoid direct contact of the trauma site. Additionally, this loading mechanism produces a constant bending moment across the fracture site with minimal direct contact forces due to inherent mechanical advantage of the bending device. The bending moment was induced by modulating the contact force of the pneumatically actuated inner bending contact points. Contact forces were measured via load cell (Model 53; Honeywell; Charlotte, NC) and converted to maximum bending moment according to the fixture geometry.

Cadaveric ovine metatarsals were obtained from the hind limbs of animals (n = 8) sacrificed for unrelated studies. A 316L stainless steel 9-hole locking compression plate (LCP; VP4045.09; DePuy Synthes; Warsaw, IN) was surgically implanted on the lateral midspan of the metatarsal and secured with eight locking screws (24 mm length) with the middle hole left empty to facilitate eventual osteotomy at this location. The plated metatarsal was then loaded into the DEC-loading device with the LCP centered between the outer bending points and aligned along the length of the DEC antennas (Figure 4.3B). For all tests, the metatarsal was placed such that the distance between the antennas and the surface of the skin was less than 1 mm at the proximal and distal aspects of the antenna array. Four-point bending loads were applied (1.0-2.0 N-m in 0.25 N-m increments, n = 5 loading cycles per data collection) while measuring antenna ARF. Following loading of the intact metatarsal, the sample was removed from the loading fixture and a bone saw was used to

destabilize the mid-diaphyseal cortex contralateral to the LCP. Monocortical (1CO) and bicortical (2CO) fracture states were induced by progressively removing bone (Figure 4.3A), with each fracture state receiving four-point bending and DEC evaluations. The antenna sensitivity, a relative and inverse measure of the fracture's mechanical stiffness, was calculated as the slope of the resultant ARF/load data. Mean antenna sensitivities were calculated for each antenna and fracture state by averaging the sensitivities of all individual loading cycles.

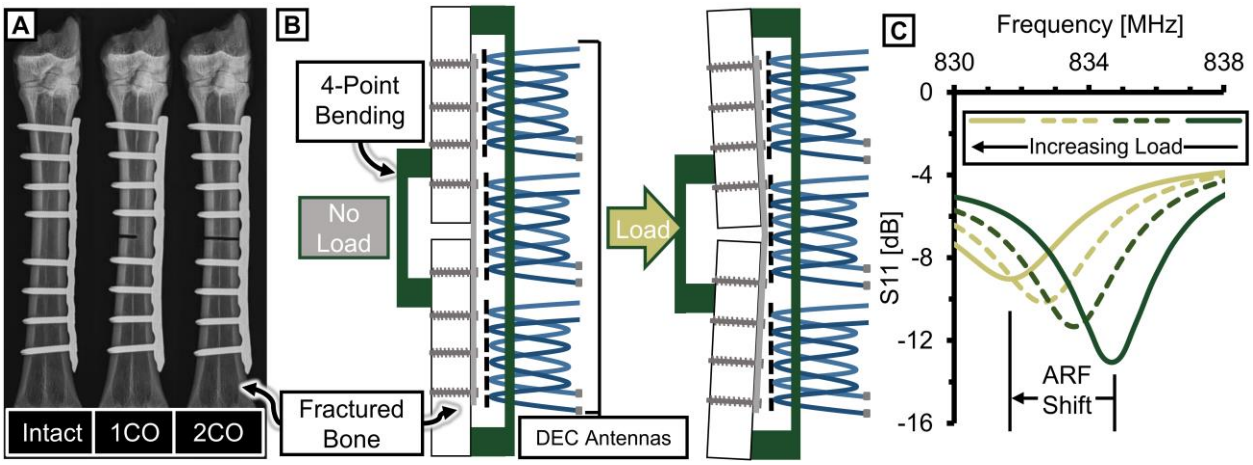

Figure 4.3: Benchtop evaluation of direct electromagnetic coupling (DEC) sensitivity to changes in fracture stiffness. (A) Different stages of fracture healing were simulated by progressively destabilizing the mid-diaphysis of a plated ovine metatarsal via increasing depth of bone saw cuts. Each fracture state was loaded in the custom loading fixture (1.0-2.0 N-m in 0.25 N-m increments, n = 5 loading cycles per data collection, n = 8 total cadaveric samples) while recording DEC antenna responses. (B) Graphical representation of the custom four-point bending loading fixture used to produce deflections of orthopaedic hardware towards the developed multi-location DEC antenna array. (C) Using this device to apply load to a bone treated by plate fixation causes the plate-antenna distance to change resulting in quantifiable shifts in apparent resonant frequency (ARF) proportionate to the amount of plate deflection.

4.2.6 In Vivo DEC Temporal Progression of Proper and Aberrant Healing Fractures

Eight skeletally mature sheep (Rambouillet cross, female, >3 years of age) were utilized for this study (Colorado State University IACUC approval #19-8990A), and housed in Colorado State

University Veterinary Teaching Hospital facilities for the duration of the study. Sheep were selected for this experimental model due to their similarity to humans in several facets pertinent to the study of bone healing: body weight, bone macrostructure [119], bone mineral composition, cortical bone microarchitecture, and bone healing rates [120]. The animals were anesthetized and the fracture site was sterilized according to standard surgical practices. A 10-cm skin incision was made over the lateral aspect of the metatarsal. Overlying soft tissue and periosteum were elevated from the bone. A 9-hole LCP (VP4045.09; DePuy Synthes; Warsaw, IN) was contoured to the metatarsal and the required holes were drilled under saline irrigation. An osteotomy was created at the metatarsal midspan by oscillating surgical saw under saline irrigation. Proper union (PU) and delayed union (DU) surgical models were created by producing a 3-mm or 6-mm osteotomy, respectively, according to results from a previous pilot study. The animals were evenly and randomly divided between the two fracture models. The plate was then attached to the bone using four bicortical locking screws in each bone fragment with the middle screw hole centered over the osteotomy gap. The middle screw hole was filled with the head of a locking screw in order to reduce the risk of plate failure (Figure 4.4A) resulting from the large stress-riser of an unfilled screw hole at the fracture site. The surgical site was closed using standard suturing techniques. The animals received immediate hard casting on the treated limb and were allowed to freely ambulate. The hard cast was bi-valued to facilitate temporary removal for DEC testing and radiographic imaging during the initial stages of healing, and was removed permanently after 3-weeks post-surgery.

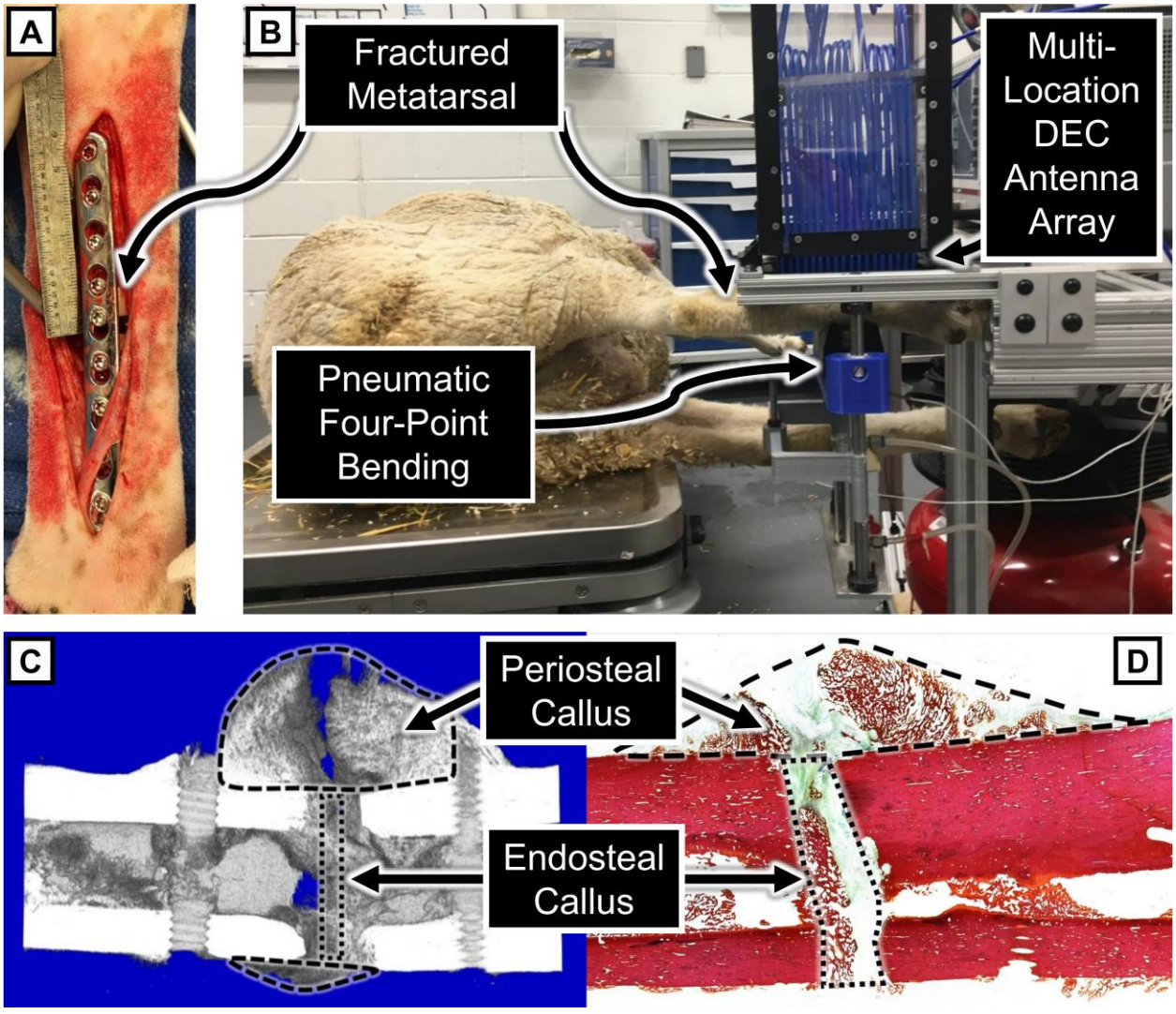

Figure 4.4: Direct electromagnetic coupling (DEC) diagnostic data in an ovine comparative fracture model. (A) Non-reduced ovine mid-diaphyseal fractures were produced by surgical osteotomy of large (5.95 ± 1.32 mm, n = 4 specimen) or small (2.80 ± 1.15 mm, n = 4 specimen) heights in order to produce delayed union (DU) or proper union (PU) healing outcomes, respectively. (B) DEC measurements of relative fracture stiffness were obtained by applying four-point bending loads (1.0-2.0 N-m in 0.25 N-m increments for n = 5 tests) while recording the resultant apparent resonant frequency (ARF) shifts in each DEC antenna. (C, D) Postmortem analysis was performed to compare, for the proper union and delayed union fracture models, tissue composition in the periosteal and endosteal callus regions of interest (ROI) using (C) μCT analysis and (D) mid-transverse histological section stained by with Sanderson's Rapid Bone Stain and counter stained with Van Gieson.

DEC evaluations were preformed twice-weekly during the initial 3-weeks post-surgery, and then weekly until animal euthanasia. During DEC evaluations animals were placed under general anesthesia and positioned in lateral recumbency to minimize animal discomfort and prevent limb movement from confounding DEC measurements of orthopaedic plate displacement. The DEC-loading fixture was utilized to apply four-point bending loads (1.0-2.0 N-m in 0.25 N-m increments for n = 5 tests) to the treated limb while measuring the resultant ARF shifts (Figure 4.4B). For all tests, the metatarsal was positioned such that the distance between the DEC antennas and the surface of the skin was less than 1 mm at the proximal and distal aspects of the antenna array. Mean antenna sensitivities were calculated according to the same methods as the aforementioned *in vitro* experiments. To account for inter-specimen differences in initial limb stiffness resulting from intrinsic variations in anatomic bone structure, normalized antenna sensitivities were quantified as a percentage of each specimen's maximum antenna sensitivity exhibited throughout the study duration. The use of these data as a diagnostic metric was driven by the presumption that relative changes, rather than the absolute value, of fracture stiffness indicate whether fractures are progressing towards proper or adverse healing outcomes. The use of DEC antenna sensitivity as a diagnostic metric were thus supported by the results of the prior benchtop and *ex vivo* experiments which indicated DEC antenna sensitivity to vary with changes in fracture stiffness. Antenna sensitivity rate of change during the initial stages of healing was calculated as the slope of a linear fit applied to the normalized antenna sensitivities during the first 30 days post fracture [96]. Weekly bi-planar radiographic images of the treated limbs were taken throughout the duration of the study.

Animals from the union and delayed-union surgical models were euthanized at 8-weeks and 10-weeks post-surgery, respectively. Following euthanasia, the metatarsals were immediately collected (≤ 30 min.) and soft tissue was removed. The bending stiffness of each sample was measured by four-point bending in a servo-hydraulic testing system (858 MiniBionix; MTS Systems Corp; Eden Prairie, MN). Following five preconditioning cycles, samples received an additional five loading cycles of cranial-caudal bending (0.5-3.0 N-m, 0.05 mm/s crosshead displacement rate). Bending stiffness was calculated from the slope of the linear portion of the moment-displacement data. Following initial bending tests, the LCP and hardware were removed and testing was repeated for the hardware-free bone.

Following biomechanical testing, the samples were placed in 70% ethanol solution. Micro-computed tomography (μCT) analyses were performed at the fracture site (voltage: 70 kVp, current: 114 μA, integration time: 500 ms; Scanco μCT 80; Scanco Medical AG; Bruttisellen, Switzerland). Three dimensional images were rendered from the μCT data and used to produce mid-transverse slices to investigate cortical bone bridging across the fracture site. Total bone volume (TBV), bone volume fraction (BVF = TBV / total volume), and bone mineral density (BMD = mg HA/cm^3) were quantified for the endosteal callus region of interest (ROI) consisting of a 1.5 mm thick section at the fracture midspan, and for the periosteal fracture callus ROI defined as the section between the screw holes adjacent to the fracture, excluding the diaphyseal bone [76] (Figure 4.4C).

The metatarsals were processed for histological analysis by dehydration and hard acrylic embedding using standard histology techniques. Sections were made along the transverse (mediolateral) plane to include the fracture callus and adjacent diaphyseal bone. The sections were stained with Sanderson's Rapid Bone Stain and counter stained with Van Gieson. High-resolution images were obtained using a microscope (E800; Nikon; Tokyo, Japan), Spot Imaging System (Diagnostic Instruments; Sterling Heights, MI), and histomorphometry software (Image Pro; Media Cybernetics; Rockville, MD). Ten-times magnification images were acquired and assembled into a composite image to perform static histomorphometry analyses of the stained sections in two ROIs: periosteal callus and endosteal callus. The periosteal callus ROI was defined with the mediolateral boundary being the region exterior to the bone surface contralateral to the orthopaedic plate, and proximodistal boundaries being the screw holes adjacent to the fracture site. The boundaries of the endosteal ROI was defined by the mediolateral edges of the diaphyseal cortical shell and the proximodistal edges of the fracture gap (Figure 4.4D). Fractional areas (%) of fibrocartilagenous and mineralized tissues were calculated in each ROI.

4.2.7 Statistical Analysis

All statistical analyses were performed using Minitab 18 (Minitab LLC; State College, PA). Statistical comparison of *in vitro* antenna sensitivities were performed using a one-way analysis of variance (ANOVA) with significance between groups determined by *post-hoc* pairwise Tukey comparisons ($\alpha = 0.05$). The effects of fracture model on DEC antenna sensitivity rate of change, μCT, and histomorphometry analyses were compared using two sample t-test comparisons ($\alpha = 0.05$), where μCT and histologic comparisons were made while blocking data to control for ROI. Postmortem biomechanical data comparisons were compared by one-way ANOVA.

4.3 Results

4.3.1 DEC Antenna Sensitivity to Orthopaedic Implant Deflections

To evaluate the efficacy of dipole antennas to detect orthopaedic implant deflections, a stainless steel plate was introduced at various locations along the length of a linear dipole antenna while measuring the resultant shift in ARF apparent for all odd frequency harmonics (Figure 4.1A). For all resonant frequency harmonics tested, the quantity of antenna locations of maximum sensitivity to implant deflections increased with increasing harmonic number (Figure 4.1B). Relative DEC antenna sensitivity (S; %) as a function of position from the end of the antenna (x; mm), total antenna length (L; mm), and the measurement harmonic number (H, #) followed a quantifiable pattern (Equation 4.1); which was used to predict locations of maximum antenna sensitivity for higher order harmonics (H > 11) used in subsequent antenna designs.

$$S(x,H) = 0.5 * \left[1 + \cos\left(\frac{\pi x(2H-1)}{2L}\right)\right] \qquad (4.1)$$

Using the above relationship, a three antenna array was created with the all antennas designed for measurement at the 25th harmonic. This design was selected according to observations that DEC measurements at this harmonic produced minimal cross-talk between adjacent antennas. For each antenna, a linear dipole antenna was coiled to align three identified locations of maximum antenna sensitivity [97], with the goal of amplifying overall antenna sensitivity to implant deflections in a focused spatial region (Figure 4.2A).

4.3.2 DEC Antenna Array Sensitivity to Cross-Talk

In using linear actuators to displace a stainless steel plate from the proximal antenna, while positioning identical stainless steel plates in static adjacency to the midspan and distal antennas

(Figure 4.2A), the proximal antenna experienced a 1.081 MHz ARF shift while the midspan and distal antennas ARF shift magnitudes were ≤ 0.051 MHz (Figure 4.5A). Similar analysis at the midspan antenna produced a 2.110 MHz ARF shift at the midspan antenna, and ARF shift magnitudes at the adjacent antennas were ≤ 0.010 MHz (Figure 4.5B). When this test was performed with the distal antenna, a 0.541 MHz ARF shift was produced at the distal antenna, and the other antennas experienced ARF shift magnitudes of ≤ 0.067 MHz (Figure 4.5C). These data demonstrated that three coiled antennas could be used in close proximity (≥ 4 cm) to each other with minimal effect on adjacent antennas' ARF (i.e., antenna cross-talk) as a function of implant displacement.

4.3.3 DEC Antenna Array Sensitivity to Orthopaedic Plates

To evaluate the sensitivity of the DEC antenna array to changes in antenna-implant distance in the presence of biological tissue, a LCP was covered in cadaveric ovine tissue and displaced from the three antenna array via a precision linear actuator (Figure 4.2D). The sensitivity of each antenna to displacement, defined as the instantaneous slope of the ARF shift / LCP-antenna distance curve (Figure 4.5D), decreased with increasing distance between the skin surface and antenna array. In increasing plate-antenna distance from 0.5 to 5.0 mm, the proximal, midspan, and distal antenna sensitivities decreased by 96%, 88%, and 85%; respectively (Figure 4.5E).

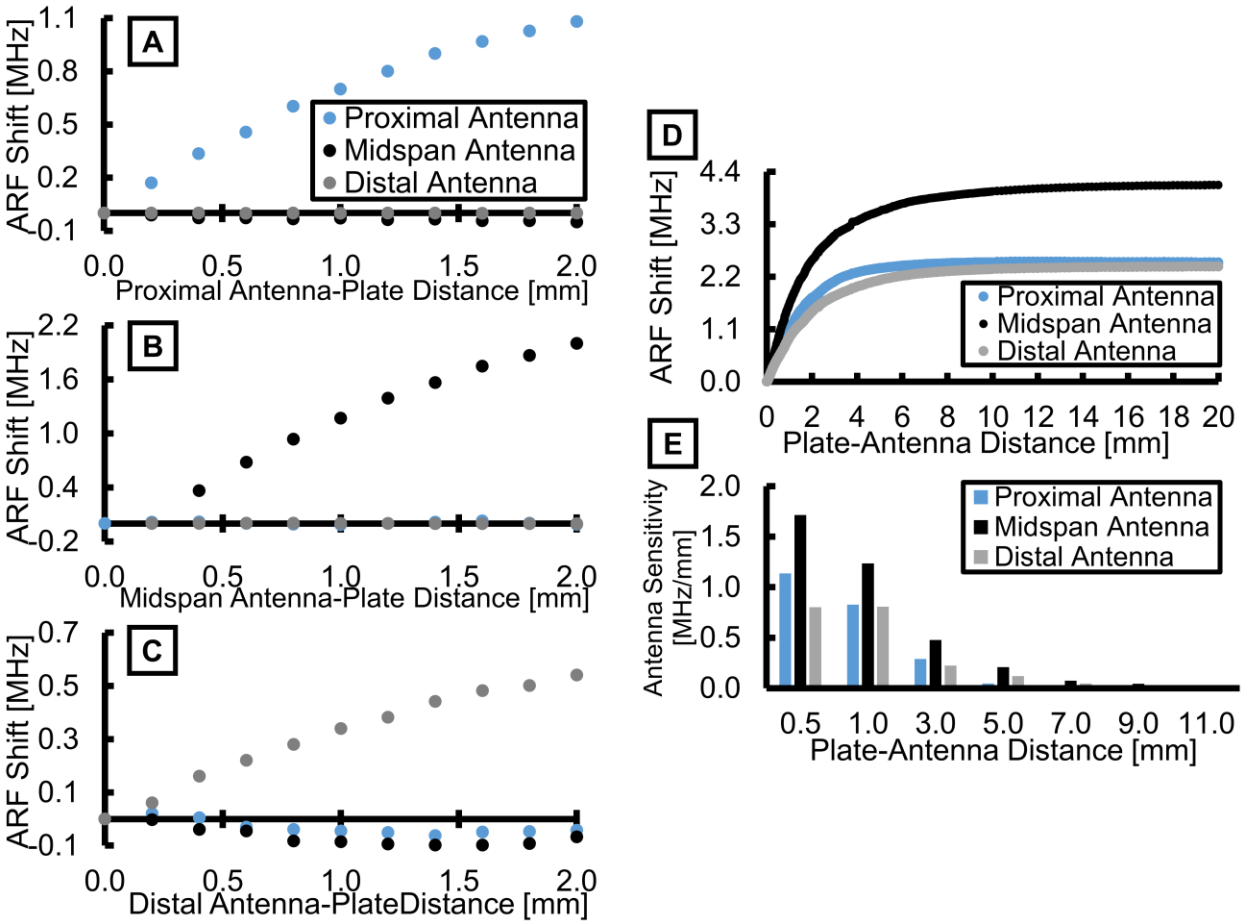

Figure 4.5: Comparative fracture model comparison. (A-C) Results of three-actuator antenna cross-talk experiments (methods depicted in Figure 4.2A). Graphs correspond to individually displacing the top, middle, or lower plate segments (A-C, respectively) while maintaining constant positioning of the other plate segments. Results illustrate maximum ARF shifts at the site of the active linear actuator (i.e., the individual plate segment which was displaced from the antenna array) while apparent resonant frequency (ARF) shifts remained less than 0.1 MHz for antennas away from the active linear actuator. (D) ARF shifts resulting from increasing distance between direct electromagnetic coupling (DEC) antennas and orthopaedic fracture plate covered in cadaveric ovine tissues (methods depicted in Figure 4.2B). (E) Instantaneous slope of each curve in Figure 4.5D produces the antenna sensitivity at a given plate-antenna displacement.

4.3.4 DEC Differences in Cadaveric Fractures of Varying Stiffness

To clarify the sensitivity of the developed DEC antenna array to changes in fracture site stiffness, fracture healing was simulated by progressively reducing the mid-diaphyseal stiffness of cadaveric ovine metatarsals treated by 9-hole LCP (Figure 4.3A). For each fracture state, four-point bending was applied to the metatarsal to produce physiologically relevant LCP deflections which were

simultaneously measured by the DEC antenna array. A characteristic plot of antenna sensitivity as a function of location and fracture state for a single representative sample is provided in Figure 4.6. For the 2CO fracture state, all samples exhibited significantly different antenna sensitivities at all antenna locations. For all samples, the antenna sensitivity at the fracture site was significantly greater for the 2CO state than the 1CO and intact states, and the 1CO state was significantly more sensitive than the intact state for the majority of samples (6 of 8 samples). At locations away from the fracture site (i.e., the proximal and distal antennas), the majority of samples exhibited significantly greater antenna sensitivity for the 2CO state than the 1CO and intact states (7 of 8 samples).

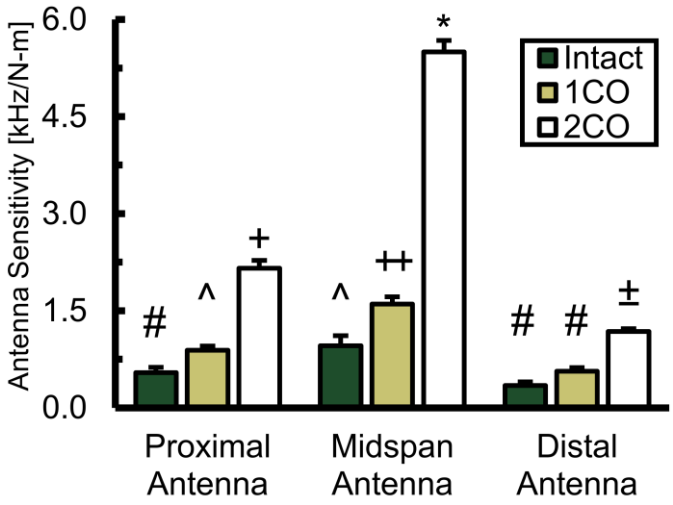

Figure 4.6: Mean direct electromagnetic coupling (DEC) antenna sensitivities (slope of apparent resonant frequency (ARF) shift per applied moment) for each antenna location and fracture state for a single representative cadaveric metatarsal sample. Intact, 1CO, and 2CO fracture states respectively represent a progressive destabilization of the fracture site by reducing the quantity of cortical bone, as depicted in Figure 4.3A. Means with different symbols (i.e., *, +, ++, #, ±, or ^) are significantly different ($p < 0.05$).

4.3.5 In Vivo DEC Temporal Progression of Proper and Aberrant Healing Fractures

To better understand the clinical performance of DEC as a diagnostic tool, an ovine comparative fracture model was implemented in which animals received a mid-diaphyseal metatarsal surgical

osteotomy of large (5.95 ± 1.32 mm) or small (2.80 ± 1.15 mm) heights in order to produce delayed (DU) or proper (PU) healing outcomes, respectively. All fractures were treated by 9-hole LCP and weekly DEC diagnostic data was collected during four-point bending of the treated limb. The mean rate of change in DEC antenna sensitivity during early healing (< 30 days post-fracture) was significantly different between the DU (-3.04 ± 0.67 %/day) and PU fracture groups (0.93 ± 0.80 %/day, $p < 0.001$, Figure 4.7A).

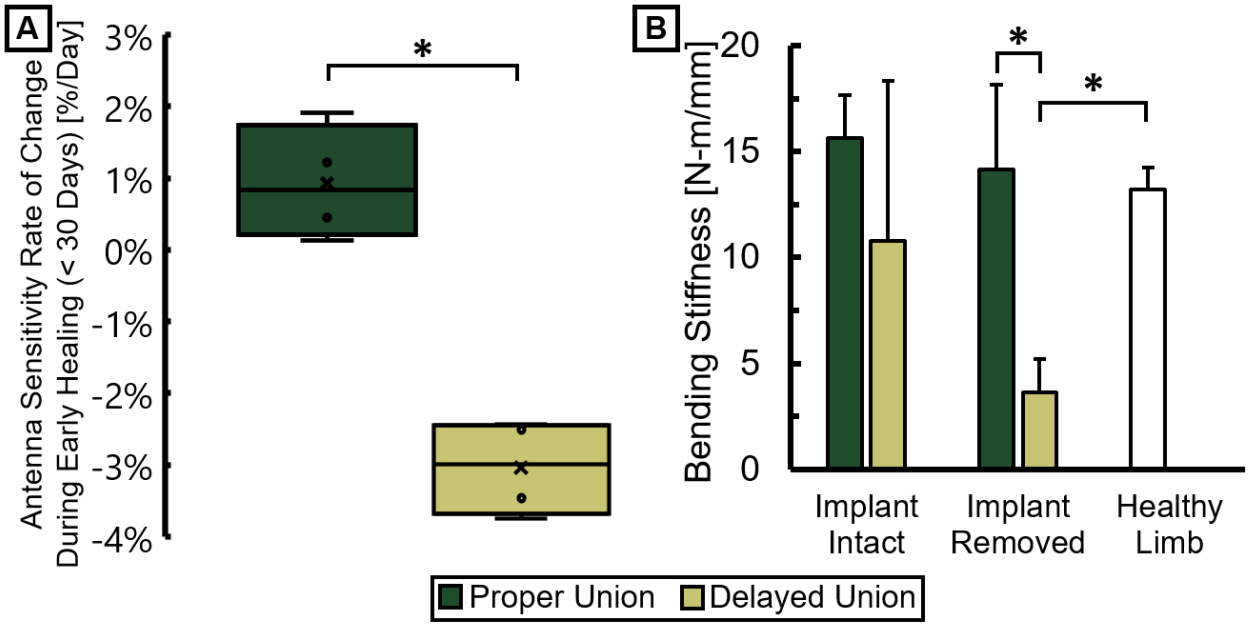

Figure 4.7: Direct electromagnetic coupling (DEC) diagnostic data and postmortem biomechanics comparison for in vivo fracture model. (A) Compiled results of DEC antenna sensitivity rate of change during early fracture healing in DEC diagnostic data for fractures trending towards union versus delayed union. Significant differences ($p < 0.05$) are indicated by a *. (B) Fracture site bending stiffness as determined by post-mortem four-point bending in a servo-hydraulic loading fixture. Significant differences ($p < 0.05$) are indicated by a *. Fracture site bending stiffness (i.e., with the plate implant removed) was significantly lower for the delayed union fracture model than the proper union fracture model ($p = 0.002$) and healthy contralateral metatarsals ($p = 0.003$).

For the DU fracture model, all animals exhibited maximum midspan antenna sensitivity within the first two weeks post-surgery (mean 8.75 ± 3.50 days post-surgery), and tended to decrease until

animal sacrifice (Figure 4.8). For all DU specimens, the normalized midspan antenna sensitivities remained below 50% after four weeks post-surgery. Normalized midspan antenna sensitivity for this group decreased by an average of 81.2 ± 18.0% from maximum sensitivity to sensitivity at study's conclusion. The first radiographic indications of fracture site mineralization for the DU specimen occurred between weeks four and eight (Figure 4.9). Each specimen exhibited visual radiopacity at the fracture site, but had yet to achieve full cortical bridging; thus, it was concluded that all animals in this group exhibited a delayed fracture union healing pathway. The animals in the PU fracture model exhibited maximum midspan antenna sensitivity at 19.00 ± 11.58 days. Initial radiographic indications of fracture site mineralization occurred between three and four weeks post-surgery (Figure 4.9). All specimen in this group achieved clinical union based on successful cortical bridging at the animals' sacrifice.

Fracture callus stiffness was quantified by servo-hydraulic four-point bending during post-mortem analysis. Cranial-caudal bending stiffness of the DU group (n = 4) was measured to be 10.77 ± 7.58 N-m/mm and 3.62 ± 1.59 N-m/mm when subjected to 4-point bending with orthopaedic hardware attached and removed, respectively. Similar analysis of the PU group (n = 3) produced bending stiffness of 15.66 ± 2.00 N-m/mm and 14.15 ± 4.04 N-m/mm, respectively. One PU sample was omitted from biomechanical analysis due to experimental error. The bending stiffness of the intact contralateral metatarsi were 13.23 ± 1.04 N-m/mm (Figure 4.7B).

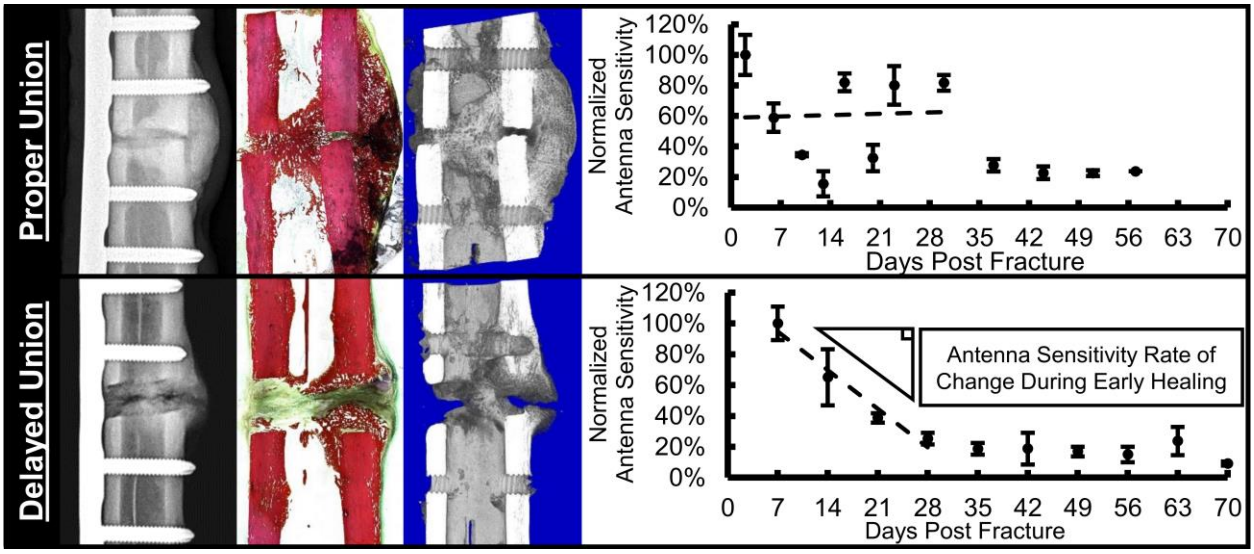

Figure 4.8: Comparison of in vivo fracture models. From left to right are x-ray images, mid-transverse histological section stained by with Sanderson's Rapid Bone Stain and counter stained with Van Gieson, mid-transverse micro computed tomography (μCT) image, and direct electromagnetic coupling (DEC) sensitivity measured at the fracture site throughout the study duration (mean ± standard deviation of n = 5 replicate measurements per testing session). To account for inherent inter-specimen anatomical structural variations, antenna sensitivities are normalized by reporting as a percentage of the maximum observed sensitivity for each specimen during the study duration. Antenna sensitivity rate of change during early healing is calculated as the slope of a linear regression applied to antenna sensitivity data during the first 30 days of fracture healing.

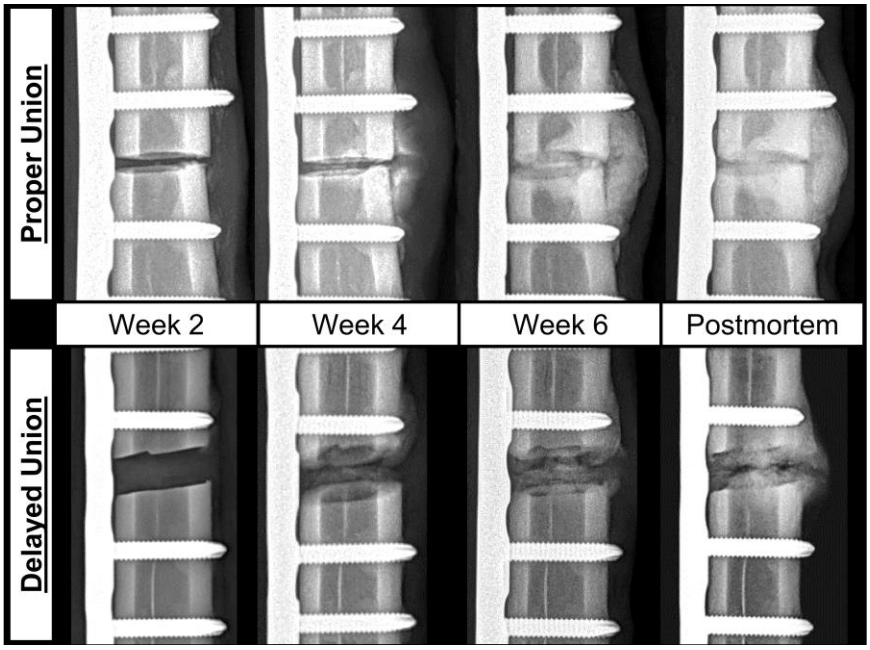

Figure 4.9: Radiographic progression of individual representative samples progressing towards proper (top row) or delayed (bottom row) fracture union.

Periosteal callus and endosteal callus BMD were not significantly higher for animals of the PU fracture model (504.5 ± 37.8 mgHA/cm^3 and 357.8 ± 109.6 mgHA/cm^3, respectively) than the DU fracture model (428.8 ± 66.9 mgHA/cm^3 and 226.6 ± 142.3 mgHA/cm^3, respectively; Figure 4.10C). TBV and BVF within both callus ROIs were on average larger for the PU fracture model than the DU fracture model, however these values were not statistically different (Figure 4.10A-B).

According to postmortem histomorphometry analyses, the mean observed area fraction of bone within the periosteal callus and endosteal callus were significantly higher ($p = 0.009$ and $p = 0.003$, respectively) for animals of the PU model (68.9 ± 13.0% and 63.8 ± 9.9%, respectively) than the DU model (32.1 ± 12.2% and 31.6 ± 6.4%, respectively, Figure 4.10E). Mean area fraction of fibrocartilage tissue was higher in both callus ROIs for the DU fracture group, but these differences were not statistically significant (Figure 4.10F).

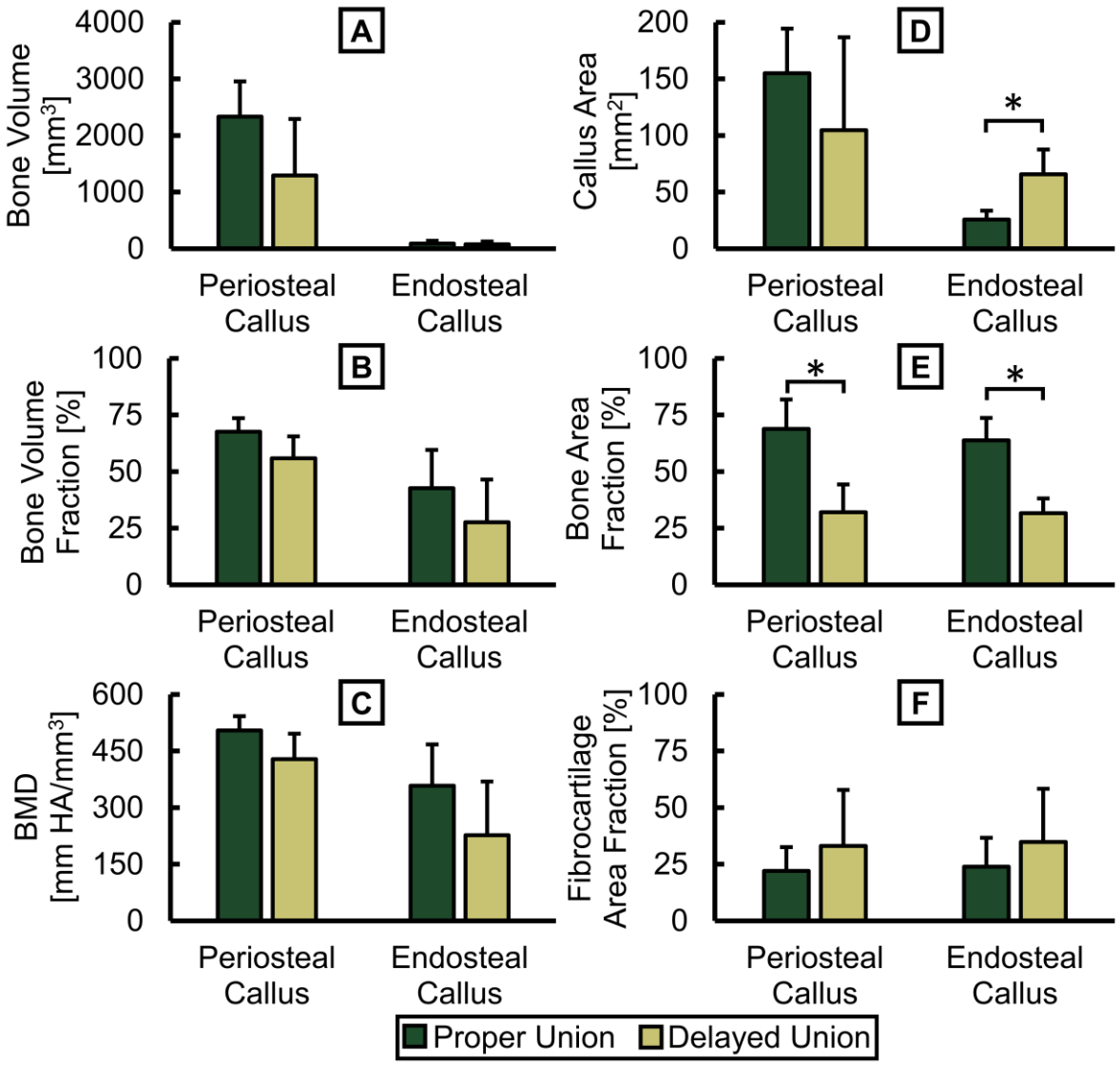

Figure 4.10: Comparative fracture model postmortem micro computed tomography (μCT) and histomorphometry. Significant differences ($p < 0.05$) are indicated by a *. Mean results of μCT analysis of (A) total bone volume (TBV), (B) bone volume fraction (BVF = TBV / total volume), and (C) bone mineral density (BMD). For all analyses, there were no significant differences between proper union and delayed union models within either region of interest (ROI). (D-F) Mean histomorphometry results indicate total callus area to be significantly greater for the delayed union fracture model ($p = 0.04$), and proper union bone area fraction to be significantly greater in both the periosteal and endosteal ($p = 0.009$ and $p = 0.003$, respectively).

4.4 Discussion

During DEC antenna design experiments, introduction of stainless steel to the linear coaxial cable antenna induced large ARF shifts of some harmonics, while having little to no effect on the ARF

of other harmonics. This supports the conclusion that this antenna type is effective at detecting the presence of orthopaedic plates, with the antenna sensitivity varying by location and resonant frequency harmonic number. Locations of maximum antenna sensitivity are of paramount importance for designing antennas to measure orthopaedic hardware deflection as these locations maximize the measurable ARF shift for small changes in antenna-plate displacement.

These results are consistent with the findings of Labus et al. where it was observed that coaxial cable DEC antennas exhibit increasing quantities of high sensitivity antenna locations as measurement harmonic number was increased [97]. The results of the current study expand upon these findings by demonstrating this relationship to hold true for the first 11 ARF harmonics. Increasing harmonic number decreases the size of regions along the cable with high DEC sensitivity (Figure 4.1B). It may be advantageous to design DEC antennas for higher harmonics, therefore creating a more focused region of high sensitivity antenna measurements; however, increasing harmonic number results in elevated measurement frequency (i.e., shifting from MHz to GHz) which is known to produce increased signal loss through biological tissues [84].

The multi-antenna array designed in this study exhibits minimal antenna ARF shifts when displacements are increased at an adjacent antenna (Figure 4.5A-C), thus indicating minimal antenna cross-talk. Each antenna is therefore concluded to be independent in measuring their respective discrete spatial regions. However, it should be noted that this was measured using separate metal plates which were individually displaced. This is not directly representative of orthopaedic hardware deflections which are continuous over the length of the implant.

Furthermore, translations of metal plates via linear actuators simulates rigid body displacements rather than bending induced deflections. These limitations were assumed to be permissible for initial antenna development given that more clinically relevant follow-up studies were performed, but care should nonetheless be taken when comparing these benchtop data to *in vitro* and *in vivo* findings.

All antennas in the final array demonstrated the ability to produce quantifiable ARF shifts of greater than 2 MHz when increasing skin-antenna distance from 0 to 5 mm via linear actuator (Figure 4.5D), which supports the ability of this technique to measure mechanically induced orthopaedic hardware deflections *in vivo*. This test established differences in antenna sensitivity associated with antenna location, where the proximal and distal antennas exhibited ≥ 41.1% reduction in total ARF shifts relative to the middle antenna. Additionally, antenna sensitivity reduced appreciably with increasing distances of empty space between the antenna and LCP, as demonstrated by antenna sensitivity reducing by ≥ 85% when LCP-antenna distance exceeded 5 mm (Figure 4.5E). These data thus indicate that the current DEC antennas must be in close proximity to coupled members for measurement efficacy.

Use of an *in vitro* cadaveric fracture model introduced physiologic tissues and clinically relevant implant bending to provide a more translational approximation of DEC's performance in quantifying relative changes in fracture site stiffness. Antenna sensitivities were highly repeatable for a given fracture state (Figure 4.6) thus suggesting adequate implant-antenna coupling despite the introduction of physiologic tissues. The DEC antenna array further demonstrated the ability to

quantify significant differences in antenna sensitivity associated with stiffness of the fracture site. Decreased occurrences of significant differences were observed at the antennas away from the fracture site, which can feasibly be attributed to a combination of reduced implant deflection at these locations and lower inherent antenna sensitivity. Based upon low data variance, non-linear antenna sensitivity effects did not appear impactful within a given *in vitro* analysis of orthopaedic hardware deflection. This is consistent with the findings of Labus et al. [97] and can ostensibly be attributed to ARF shifts being approximately linear for the small scale deflections produced in this testing setup. However, non-linear effects may present challenges in comparing data from successive time points due to differences in initial implant-antenna distances resulting in changes to antenna sensitivity to hardware deflection.

Significant differences in antenna sensitivity were associated with antenna location within the array. In the case of simple mid-diaphyseal fractures, such as those simulated in this study, quantification of implant deflection away from the fracture site is of secondary interest. However, this information may prove expedient as a diagnostic tool for cases of non-diaphyseal or complex fracture types. Use of multi-location antenna arrays may be additionally useful for improving diagnostic accuracy by reducing data artifacts resulting from soft tissue compliance. DEC antennas measure relative changes to the implant-antenna distance, but are indiscriminate to displacements resulting from mechanical deformation versus rigid body displacement. While the custom loading fixture used in this study was designed to minimize rigid body displacement of the fractured limb, these effects cannot be completely eliminated due to compression of compliant soft tissues (i.e. skin and muscle) at the application sites of bending loads. DEC antenna sensitivities are consequently amplified due to compression of soft tissues causing the entire limb to displace

towards the antennas. Diagnostic DEC data relies upon relative changes in antenna sensitivities, rather than absolute values, thus rigid body effects are hypothesized to be inconsequential for clinical use of DEC provided that soft tissue compliance levels are consistent across testing sessions.

These rigid-body effects may be reduced nonetheless through use of a multi-location antenna array, rather than a single diagnostic antenna. In four-point bending, translation in the direction of bending at the stationary (outer) bending points is negligible for bending displacements alone. Thus, the multi-location DEC array may be used to measure deflections at these locations to quantify rigid body displacements, while simultaneously performing diagnostic DEC measurements at the fracture site. Subtracting these rigid body effects from the diagnostic measurements could then facilitate improved accuracy of measurements made at the fracture site. In theory, such a technique would obviate soft tissue compliance effects to provide an isolated measurement of relative implant stiffness which could not be obtained exclusively from four-point bending or single-DEC measurements.

For the *in vivo* fracture model, all animals of the PU group achieved successful fracture healing prior to study termination as supported by radiographic appearance of cortical bridging and postmortem bending stiffness values comparable to healthy untreated bone (Figure 4.7B). Conversely, terminal radiographic images of the DU fracture gap indicated failure to achieve cortical bridging. Radiographic callus presentation was varied in this treatment group, with three animals presenting large partially calcified endosteal and periosteal calluses, and one animal

showing a complete lack of periosteal callus formation or calcification. The former case is indicative of mechanical instability at the fracture site and may heal if given excess time to heal; however, the latter case is suggestive of atrophic nonunion and is unlikely to heal without secondary clinical intervention [15, 26, 27]. The radiographic indications of aberrant healing in this treatment group are supported by the postmortem biomechanics data where the observed mean fracture stiffness was significantly lower than healthy limbs or those of the PU treatment group (Figure 4.7B).

Despite the significant differences in observed fracture stiffness associated with surgical model, no significant differences were observed in μCT data. However, periosteal callus measurements of TBV, BVF, and BMD were trending towards being significantly greater in the PU model relative to the DU model ($p = 0.14$, $p = 0.095$, & $p = 0.11$; respectively). These trends are supported by the observed histomorphometry data which indicated the PU model to express significantly higher bone area fractions in both the periosteal and endosteal callus regions (Figure 4.10E). These findings are consistent with previous studies which have demonstrated larger fracture gaps to experience delayed fracture healing [99] and reduced callus mineralization [130].

Differences between biomechanical and μCT analyses may stem from the inability of μCT to discern cortical bridging in the periosteal callus. For example, three samples in the DU fracture group exhibited hypertrophic periosteal callus formation in which large quantities of mineralized tissue were formed near the diaphyseal cortices, but very little formed at the fracture site. The resultant discontinuity of mineralized tissue across the fracture gap is expected to decrease fracture

site mechanical stiffness while still exhibiting adequate levels of bone formation according to μCT analysis of the periosteal callus composition as a whole. This conclusion is supported by the histologic and μCT appearance of calcified tissue bridging of the fracture site in the PU group, which was accompanied by a significantly greater bending stiffness relative to the DU group (Figure 4.7B). These observations are consistent with the findings of Panjabi et. al. [44] and Augat et. al. [131] which established the importance of cortical continuity along the fracture line for restoring mechanical stability.

The biomechanical, histology, and μCT data suggest the two cohorts of this study to be a reasonable approximation of normal and aberrant / delayed fracture healing. *In vivo* radiographic evidence of callus mineralization was temporally adequate in the PU group (i.e., callus radiopacity appearing three to four weeks post-fracture) but was considerably postponed for the DU group (i.e., callus radiopacity appearing four to eight weeks post-fracture); thus, this study partially recapitulated the diagnostic deficits of x-ray imaging for predicting fracture healing outcome. This is further supported by the appearance of radiopaque tissues at the fracture site in three of four DU animals despite reduced fracture stiffness (Figure 4.7B). These findings are consistent with current literature where it has been established that planar radiographic images are a poor predictor of stiffness [42] and strength [44] of the healing fracture.

While standard planar x-ray imaging was unable to identify changes to the osteotomy site during the early stages of fracture healing, DEC antenna diagnostics were able to detect significant differences between proper and delayed healing during the first 30 days of fracture healing (Figure

4.7A). Normalized DEC sensitivity from the DU group were greatest during the initial stages of healing (mean 8.75 ± 3.50 days post-surgery) followed by a steady decrease throughout the remaining study duration. The PU group exhibited observably different temporal DEC profiles throughout the study, and were generally characterized by a lack of temporal pattern (Figure 4.8).The present data agree with previous studies where it has been shown that fracture site stiffness may be indirectly quantified by monitoring fixation plate mechanics [75], and temporally repeated measurements can identify aberrant bone healing during early stages of healing [69, 78, 96]. DEC is advantageous for this application as it does not require direct measurement of implant strain, thus obviating the need for external fracture fixation or sensor instrumentation of custom internal fixation devices which has been associated with sensor failure [69] and difficulties in interrogating sensors through overlaying soft tissue [80].

While the significant differences observed within the first 30 days of healing marks a five month improvement relative to mean nonunion diagnosis in humans [16], but care must be taken when extrapolating these results to human fracture due to inherent interspecies differences despite similarities in body weight, bone macrostructure [119], bone mineral composition, cortical bone microarchitecture, and bone healing rates [120]. The current study also remains limited by small sample size and low variety of fracture type and treatment combinations. The possibility of unintentional bias cannot be excluded from these experiments due to non-blinded testing. As discussed in the proceeding text, this study is also limited by the lack of technical maturity inherent to any emerging technology including the DEC antenna used throughout these experiments.

Despite positive results for DEC in differentiating proper and aberrant healing pathways during initial stages of fracture repair, there remains a number of obstacles to be overcome for this diagnostic technique to achieve clinical utility. We hypothesize that the dissimilarity of the PU and DU fracture group antenna sensitivity profiles can be attributed to differences in fracture stiffness rate of change during initial fracture healing in combination with the data normalizing technique used in this study. It is thought that the DU group exhibits a gradual increase in fracture stiffness throughout the study duration while the PU group experiences a rapid improvement in fracture stiffness during the early stages of healing due to the smaller fracture gap and more expedient healing response. This theory aligns with results of previous studies where fractures exhibiting delayed healing present significantly reduced mineralized tissue formation and callus formation during the initial stages of healing, but later compensate through excess callus volume to achieve callus stiffness comparable to rapidly healing fractures [132]. This is further supported by the expedited radiographic appearance of callus calcification in the PU group of the present study.

Based on this hypothesis, it is thought that the gradual changes in fracture stiffness of the DU group may be adequately quantified by weekly DEC measurements. In instances of rapidly stiffening fractures, however, DEC measurements would quickly become unable to reliably distinguish data noise from legitimate ARF shifts due to insufficient antenna sensitivity to exceedingly small plate displacements. Normalized DEC values would thus be similar from week to week as the antenna sensitivity is insufficient to detect further changes in plate displacement of the already stiff plate-fracture construct. This theory aligns with the present data as evidenced by the negative early healing rate of change in antenna sensitivity for the DU group (-3.04 ± 0.67 %/day) and the near zero value for the PU group (0.93 ± 0.80 %/day, Figure 4.7A, Figure 4.8).

These results emphasize the need for future technological developments to the DEC antennas to improve their sensitivity to small plate displacements. Such improvements will progress the clinical utility of this diagnostic by enabling better characterization and comparison of proper-, delayed, and non-unions throughout the full duration of the healing timeline.

As previously discussed, the use of a multi-DEC antenna array is of particular interest for potential application towards averting DEC data artifacts resulting from soft tissue compliance. In using four-point bending to produce the implant deflections vital to DEC measurements, there is an unavoidable introduction of rigid body displacement of the treated limb resulting from compression of soft tissues at the limb-loading fixture contact points. These effects may potentially be mitigated through implementation of the multi-location DEC array to directly quantify limb rigid body displacements. However, the current design of the DEC antenna array is insufficient to enable measurements in a region of sufficiently discrete spatial resolution to facilitate such corrections; thus, future technological improvements will be pursued to this end.

Additional improvements for DEC must be centered upon real-time identification of aberrant fracture healing. While the current system was able to identify significant differences in healing pathway during the first 30 days post-fracture, this result was obtained during *post hoc* analysis. For clinical utility, it is imperative that fracture healing outcome be identified within the initial stages of healing, rather than in retrospective analysis. The predictive ability of this technology may potentially be improved with additional insights into the mechanical progression of fractures from additional translational studies of larger populations with diverse fracture types. Furthermore,

interpretation of early healing DEC diagnostic data would benefit from increased antenna sensitivity to facilitate improved characterization of the rapidly achieved fracture stiffness of properly healing fractures.

Future development of the DEC antenna and testing methods must also be focused on accounting for the non-linear relationship between antenna-implant distance and DEC antenna sensitivities. Accounting for these effects, either through the development of an antenna with linear distance-sensitivity behavior or through calibration methods, would enable DEC measurements to provide a direct quantification of implant deflection. Doing so would reduce effects introduced by minor differences in limb-antenna distance between testing session, and would provide clear insight to the exact mechanical state of the healing fracture site.

Further development of the DEC technology necessitates additional benchtop characterization of the effects of clinically pertinent variables on antenna sensitivity. For example, there exists a multitude of steel, cobalt-chromium, and titanium alloys which see pervasive use as orthopaedic implants, and implant alloy ostensibly affects DEC antenna sensitivity.

Furthermore, the cadaveric and *in vivo* tests performed in this study utilized a fracture model in which the LCP was covered by minimal amounts of overlaying skin, thus minimizing intervening tissues from impeding hardware-antenna coupling. However, many clinical fracture cases, such as treatment of femoral fractures, demand implantation of hardware below large depths of adipose and muscular tissues. The results of the current experiments indicate that DEC antenna sensitivity

depreciates non-linearly with increasing antenna-skin surface distance (Figure 4.5E), but the impact of hard and soft tissue thickness are not known at this time. Future works must thus be executed to characterize these relationships to better inform the clinical viability of the current and subsequent antenna designs. Such information may advise whether antennas must be designed for lower frequency measurements where electromagnetic wave penetration through biological tissues is improved [84].

Despite the present limitations of this new technology, *in vitro* and *in vivo* data exhibit the efficacy of the DEC multi-antenna system for quantifying relative temporal changes in healing fracture stiffness. This technology demonstrated the ability to quantify differences in proper versus aberrant fracture healing at 30 days post-fracture. This marks a potential five month improvement relative to average human clinical nonunion diagnosis times using x-ray imaging, although care must be taken when directly comparing the results of the present translational ovine fracture model to fracture healing in humans. In addition to its potential to accelerate diagnosis times to improve treatment of adverse fracture healing, DEC is advantageous as an emerging technology due to the relatively few regulatory hurdles associated with its clinical implementation. This can be attributed to its presumed compatibility with any existing metallic orthopaedic implant and its utilization of low energy radio frequency waves from a source external to the body. Thus, despite the need for ongoing technology maturation, DEC demonstrates potential as a clinical tool to expedite the diagnosis and treatment of failed bone fracture healing.

4.5 Footnote

We thank Dr. Holly Stewart, Katie Bisazza, Cat Hersh, Lisa Mangin, Erin McCready, Meaghan Monahan, & Izzy Olaes for their contributions to conducting *in vivo* biomechanics studies.

4.5.1 Funding

This project was supported by the National Institute of Health (NIH) - National Institute of Arthritis and Musculoskeletal and Skin Diseases (NIAMS) [R01AR069734-01 - "Early Detection and Prediction of Complex Bone Fracture Healing"]. All authors listed were involved in the study design, data collection, data interpretation, and preparation of the attached manuscript. All authors have read and approved of the submitted manuscript.

4.5.2 Reporting Checklist

The authors have completed the ARRIVE reporting checklist.

4.5.3 Conflicts of Interest

All authors have completed the ICMJE uniform disclosure form. Funding for this project was supported by the NIH-NIAMS. Additional funding from the NIH and Colorado Office of Economic Development and International Trade (COEDIT) supported related research, but did not directly support this presented work. J. Wolynski and Drs. Labus, Puttlitz, and McGilvray are authors of pending and issued patents related to the DEC technology presented in this manuscript.

4.5.4 Ethical Statement

The authors are accountable for all aspects of the work in ensuring that questions related to the accuracy or integrity of any part of the work are appropriately investigated and resolved. Experiments performed by this study were approved by the Colorado State University Institutional Animal Care and Use Committee [CSU IACUC approval #19-8990A].

CHAPTER 5: VIVALDI DEC ANTENNA DEVELOPMENT (SPECIFIC AIM 1)

The findings of Chapter 4 exhibited promising results for the use of DEC as a diagnostic predictor of bone fracture healing outcome. However, the coiled coaxial antenna design was sufficiently large to hinder the spatial resolution of the antenna measurement regions, thus precluding the ability to feasibly use multiple antennas to account for limb rigid body displacements. Furthermore, it was hypothesized that antenna calibration techniques could be implemented to directly convert DEC antenna sensitivity to fracture bending stiffness. The hypothesized technique, however, would require the antenna position to be accurately controlled via mounting to a precision linear actuator, which was not feasible for the large coiled coaxial antenna design. To this end, a collaborative effort was made with Dr. Branislav Notaroš (Colorado State University) and Dr. Milan Ilić (University of Belgrade) to develop an improved DEC antenna design.

The remainder of this chapter is adapted from a full-length research article, currently in peer-review at *IEEE Access*, which reflects the results of this collaboration. It should be noted that Drs. Notaroš and Ilić are to be credited with antenna design; my contributions to this article were the design, execution, and interpretation of experiments to evaluate the efficacy of new antenna designs for orthopaedic diagnostic applications.

5.1 Introduction

Orthopaedic bone fracture healing complications remain pervasive, despite ongoing improvements to clinical standards of care. Long bone fractures, such as those of the tibia, exhibit failed healing

(nonunion) in up to 12% of cases [11]. Fracture nonunions are extraordinarily harmful to patient wellbeing, ultimately leading to the need for additional surgical intervention, chronic pain, increased opioid usage, and an estimated 118% increase in medical expenditures [11, 12]. Healing outcome can be improved, and patient suffering reduced, in cases where rapid diagnosis of adverse fracture healing is achieved to advise corrective therapies during the early stages (<30 days post-surgery) of fracture healing [9, 13].

Achieving an early prediction of healing outcome remains difficult using current clinical diagnostic tools: namely, biplanar x-ray imaging. This qualitative and subjective technique has proven to lack specificity [30, 40, 42, 109] which limits the reliability of x-ray image predictions of healing outcome [43], and further increases mean nonunion diagnosis times to exceed 6 months [16]. The clinical deficit resulting from the imperative need for rapid prediction of adverse fracture healing, coupled with the apparent inefficacy of x-ray imaging techniques, necessitates the development of new orthopaedic diagnostic techniques.

Ongoing efforts have pursued development of technologies to quantify *in vivo* fracture biomechanics [52, 53], as fracture stiffness has demonstrated reliability as an early predictor of healing [23, 50, 53, 58, 61, 62, 67, 133]. These techniques exploit differences in the temporal progression of fractures trending towards proper or adverse healing outcomes. Proper bone fracture healing causes a progressive increase in fracture tissue (callus) stiffness; conversely, adverse healing presents temporal invariance in callus stiffness progression [78]. These mechanical patterns are apparent during early phases of fracture healing, prior to x-ray appearance of

radiopaque tissues, thus biomechanical methods exhibit promise as means to expedite accurate prediction of healing outcome [67, 96].

Bone fractures are ubiquitously treated by implantation of metallic orthopaedic hardware (i.e., rods, plates, and screws) to stabilize and support bone fragments. The bone-implant behaves as a composite structure whose biomechanical properties reflect contributions from both members; thus, temporal changes to the callus are apparent in the stiffness changes of the composite. Previous efforts have been made to leverage this phenomenon for diagnostic purposes, by instrumenting orthopaedic hardware with sensors to telemetrically report the hardware's mechanical environment (i.e., strain or load share) [78, 80, 96, 98]. Despite promising results, this technique typically requires hardware modification to accommodate sensor architecture, which precludes use with existing orthopaedic hardware types and may contribute to premature / traumatic implant failure [69].

To address these challenges, a diagnostic antenna system was developed for noninvasive quantification of relative changes in fracture stiffness for any case treated with off-the-shelf metallic orthopaedic hardware [97, 123, 129]. This diagnostic device utilized a coiled coaxial dipole antenna design to directly electromagnetically couple (DEC) to metals in its near-field, thus enabling detection of displacements of metallic implant hardware [97]. By applying controlled physiologically non-detrimental mechanical loads to the fractured limb, implanted metallic hardware displaces towards the DEC antenna. Resultant deflections produced a measureable change in the resonant frequency of the antenna, where the magnitude of implant deflections were a function of the fracture stiffness, a direct measure of healing. This technology has exhibited

aptitude in quantifying relative changes in healing fracture stiffness in translational cadaveric [129] and *in vivo* fracture models [123]. However, this antenna's predictions of implant displacements are highly sensitive to the initial antenna-implant distance which can be neither known nor controlled with confidence in a clinical setting. Specifically, imperceptibly small variations in antenna placement across temporally repeated diagnostic measurements consequently produce sufficient variance to obfuscate healing progression patterns.

We hypothesize that the ability to perform antenna calibrations will surmount these limitations by enabling accurate conversion of resonant frequency shift into implant displacements. However, these calibrations require the ability to precisely displace the antenna while performing diagnostic DEC measurements, thus quantifying resonant frequency shifts for a known change in antenna implant distance. The large size of the previous coaxial cable antenna design makes this infeasible, hence there is an imperative need for DEC antennas with an appreciable size reduction. Within this study, the applicability of Vivaldi-type antennas for this task was explored; to our knowledge, this has not been investigated nor exploited elsewhere.

Vivaldi-type antennas are known to have excellent broadband characteristics, low cross polarization, and directive radiation patterns [134]. They are widely used in broadband applications [135], and have recently been used as contactless sensors [136]. A Vivaldi-type antenna was primarily chosen for the considered application due to its simple design, low fabrication cost, ease of fabrication on a printed circuit board (PCB), simple feeding network providing internal matching with no need for tuning, and a thin profile. The thin profile of this antenna design facilitates mounting on any positioning rig, as well as adding additional elements

and forming an array for simultaneous multi-element sensing, which is ideal for orthopaedic applications.

The objective of this study was to explore the sensitivity of Vivaldi antennas for detecting movement of metal plates in the near field. Standard and miniaturized antenna designs were evaluated by computational modelling to predict antenna sensitivity to changes in metallic plate displacements; analogous physical experiments were performed using fabricated prototype antennas. Physical experiments were parametrically varied to evaluate the effects on antenna sensitivity related to alloy of the metallic plate, antenna orientation relative to the metallic plate, and whether antennas could be spatially adjusted following data collection to facilitate antenna calibration. The resultant data were used to inform the feasibility to utilize Vivaldi antennas for applications as orthopaedic diagnostic sensors.

5.2 Methods

5.2.1 Vivaldi Antenna Design

Vivaldi antennas belong to a class of tapered slot antennas. The antenna operation is most easily understood if the planar copper structure (Figure 5.1A) is imagined as an axial cross section of a body of rotation (BoR), obtained by rotating the cross section around the x-axis, since it resembles a cavity-backed open ended horn. With this in mind, one can easily understand the expectation of the antenna to be highly sensitive to frontally positioned structures, which is a main desired feature in the intended orthopedic application.

Planar Vivaldi antennas [137], manufactured on PCB, were considered as the basic sensing element for the intended application. The top side (Figure 5.1A) was comprised of a copper plating residing on a thin dielectric substrate (i.e., essentially forming an open ended slot line), and a theoretical feed point. On the bottom side (Figure 5.1B) was an actual feeding network comprised of a simple tapered microstrip line acting as an impedance transformer, metalized through via, and subminiature version A (SMA) PCB-mount connector which facilitated straightforward link to a vector network analyzer (VNA) by coaxial line.

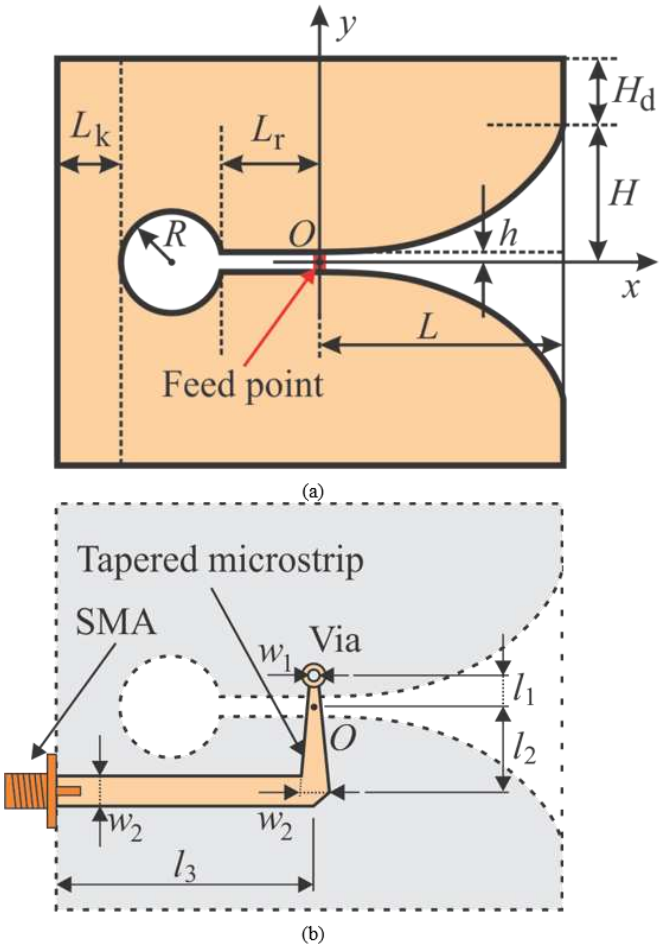

Figure 5.1: A sketch of a planar Vivaldi antenna with relevant geometrical parameters: (a) top side of a PCB with theoretical point-like feed and (b) bottom side with actual feeding network.

The symmetric slot-like section in the antenna middle (Figure 1A) was characterized [32] by a circular section (i.e., a short ended slot line of radius R) followed by a straight slot of length L_r and half-width h, followed by a slot of length L, and exponentially tapered half-width ranging from h to H, whose tapering edge was governed by Equations 5.1 – 5.3, where a is a normalizing parameter:

$$y = Ae^{ax} + B \tag{5.1}$$

$$B = h - A, \tag{5.2}$$

$$A = \frac{H - h}{e^{aL} - 1} \tag{5.3}$$

The copper plating extends to the left of the circle and, symmetrically to the top and bottom of the tapered slot by lengths L_k and H_d, respectively. The feeding point (i.e., via) was located at $x = 0$, its vertical position was very close to the conductor, edge with slightly adjustable y-axis position to facilitate impedance matching (Figure 5.1B). The width and length of the tapered microstrip feeding line were obtained by optimizing the impedance matching of the antenna to the standard 50-ohms.

When measuring through biological tissues, increasing electromagnetic frequency results in greater attenuation [84], thus operation at frequencies around 1.5 GHz was considered. The antenna, termed as "standard", was designed for variation of resonances about this frequency with respect to change in position of front-mounted metallic structures. Minimal antenna size was an important design consideration for the intended use as an orthopaedic sensor; thus, we also analyzed a "miniaturized" version of the Vivaldi antenna, which was similarly optimized with

respect to position of front-mounted metallic structures. Antenna design parameters are given in Table 5.1.

Table 5.1: Vivaldi antenna parameters for 1.5 GHz operation.

Parameter	Standard Antenna		Miniaturized Antenna	
h	0.1	mm	0.1	mm
H	20	mm	10	mm
H_d	30	mm	5	mm
L	100	mm	30	mm
R	15	mm	1	mm
L_k	6	mm	2	mm
L_r	2	mm	2	mm
a	35	m^{-1}	10	m^{-1}
w_1	1	mm	1	mm
w_2	2.9	mm	2.9	mm
l_1	8	mm	0.95	mm
l_2	38	mm	6.17	mm
l_3	38	mm	8	mm

5.2.2 Antenna Simulation

For the purpose of computer simulation (in silico) of antenna performance prior to prototype production, each antenna was modeled in a full-wave three dimensional (3-D) electromagnetic (EM) simulator (ANSYS HFSS, ANSYS; Canonsburg, PA) (Figure 5.2). This model employed a simple bridge feed and a lumped generator port. The feed was comprised of two metallic strip posts running vertically through the dielectric and a port residing on the dielectric surface (highlighted in cyan in Figure 5.2B). Metallic surfaces of the antenna were modeled as infinitely thin sheets. The primary interest was the antenna near field characteristics, thus far field parameters were not investigated. The model was encased in an air box and absorbing boundary condition (ABC) was applied at its faces to truncate the numeric domain. Full-wave simulations were carried

out at a reference frequency of 2 GHz to ensure optimal convergence at both lower and slightly higher frequencies. An initially seeded small domain tetrahedral mesh and first-order basis functions for field expansion were used. Near monotonic convergence to a maximal magnitude of S-parameter variation lower than 0.002 was typically achieved within 10 adaptive passes employing approximately 33000 elements, 209000 unknowns. Antenna reflection coefficient (S11) was simulated over a range of frequencies (0.3 – 3.0 GHz) using an interpolating sweep.

A plate was modeled as a perfect electric conductor (PEC) (dimensions of 152 x 12 x 6 mm), and was symmetrically positioned in front of the antenna (Figure 5.2A). For both antenna designs, S_{11} was simulated over a frequency broad band (0 – 6 GHz). Simulations were repeated for increasing distance / offset between the plate and antenna (0.1, 0.5, 1, 2, 3, 4, 6, 8, and 10 mm). Antenna resonance near 1.5 GHz was predicted for each plate offset.

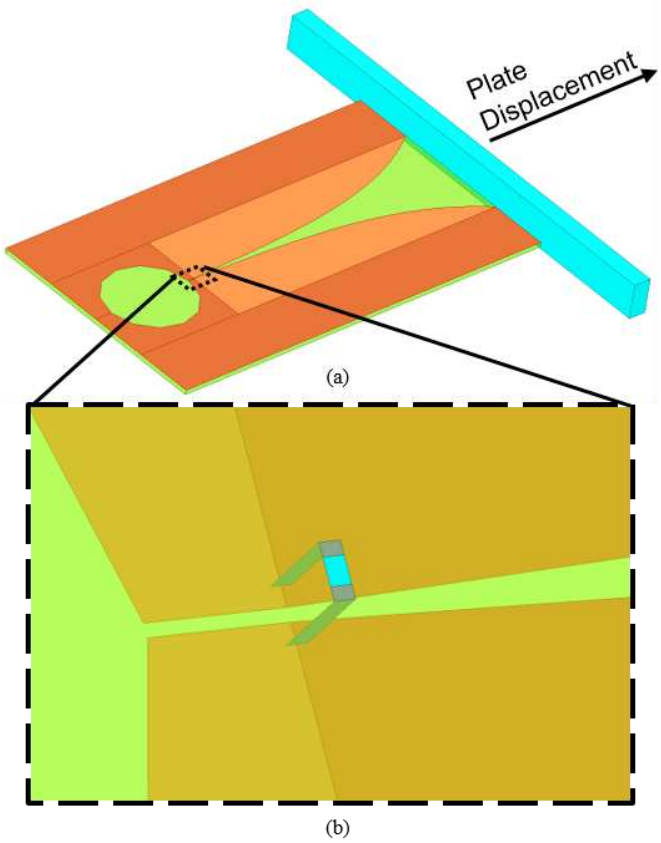

Figure 5.2: A full-wave EM model of the Vivaldi antenna with geometrical parameters from Table 5.1. (a) Top side of the antenna with metallic plate placed in front of its measurement side. (b) A magnified view of the simple lumped-port feed attached at the bottom of the substrate.

5.2.3 Prototype Antenna Production

Following *in silico* characterizations of the antennas, prototypes were fabricated for benchtop testing validation. The feeding microstrip line for both Vivaldi antenna designs were optimized to obtain good impedance matching to 50-ohms (Figure 5.3). Our design opted for a h_s = 1.57 mm thick FR-4 substrate ($\epsilon_r = 4.4$, $\tan\delta = 0.02$) with t_s = 35 μm thick double sided copper metallization. Note that these materials were employed with the exact parameters from the simulation models. The only exception was the metallization thickness, which was neglected in simulations without loss of accuracy at the considered frequencies. The layouts of the optimized antenna designs were transferred from the EM simulator to a PCB design tool, KiCad, for requisite file generation. Final

antennas were manufactured using photolithography and chemical etching. Since the PCB production allowed automatic via metallization, the only additional antenna assembly process was the soldering of the SMA connector. No additional matching networks or tuning was required because the antennas were internally matched.

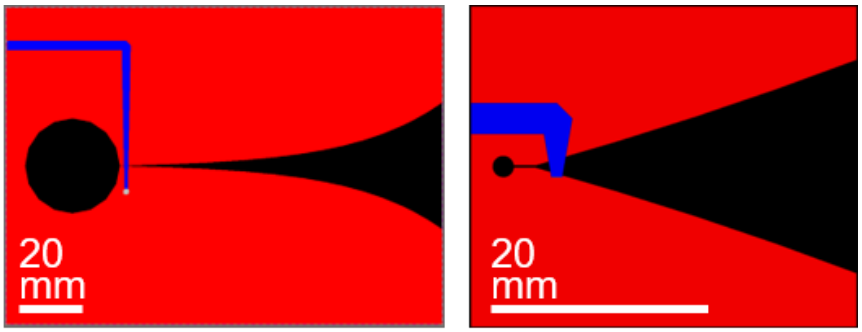

Figure 5.3: Layout of the (a) standard and (b) miniaturized Vivaldi antenna designs, showing top copper layer in red and bottom layer (feeding strip) in blue. Feature dimensions within each layout are proportionately accurate, but scaling of each layout are different to improve visibility (accurate dimensions for each layout are detailed in Table 5.1).

5.2.4 Prototype Antenna Sensitivity to Metallic Structure Displacements

To evaluate the sensitivity of the prototype antennas to changes in antenna-implant distance, a stainless steel (SS) plate (40 mm × 20 mm × 10 mm) was secured to a precision linear actuator (T-LLS105; Zaber Technologies; Vancouver, BC, Canada; 0.15625 µm microstep resolution) so that change in resonant frequency (resonant frequency shift) could be measured while progressively increasing the antenna-plate distance (Figure 5.4). To mitigate potential off-target coupling, the plate was offset from the actuator using non-conductive nylon arms, where the plate was secured to the nylon using orthopaedic screws (3.5 mm diameter, 316L stainless steel). To recapitulate the testing environment relevant to how the antenna would be used as an orthopaedic diagnostic tool,

the antenna was positioned within a surrounding aluminum construct (150 x 150 mm internal frame dimensions) (Figure 5.4).

The starting position of the plate was in direct contact with the measuring edge of the antenna, and was displaced from the antenna (0 – 10 mm, 0.01 mm increments, $n \approx 5$ data points collected at each position) while antenna resonant frequency shifts were measured. Resonant frequency was determined as the frequency at which minimum S_{11} occurred, as measured by VNA (TTR500; Tektronix; Beaverton, OR; 200 MHz span linearly distributed over 500 points, 7 dBm power). Antenna sensitivity was calculated by taking the slope of a linear fit applied to a 0.5 mm window of resonant frequency shift-displacement data. These methods were repeated for parametric variations of prototype antenna design and antenna orientation (i.e., antenna and plate lengths being parallel or perpendicular, Figure 5.4). The miniaturized antenna was designed with intended biomedical applications, and thus antenna sensitivity to orthopaedically relevant metallic alloys was a primary concern. Accordingly, tests for the miniaturized antenna design included an additional parameter: use of SS or titanium (Ti) plate materials (dimensionally equivalent plate designs).

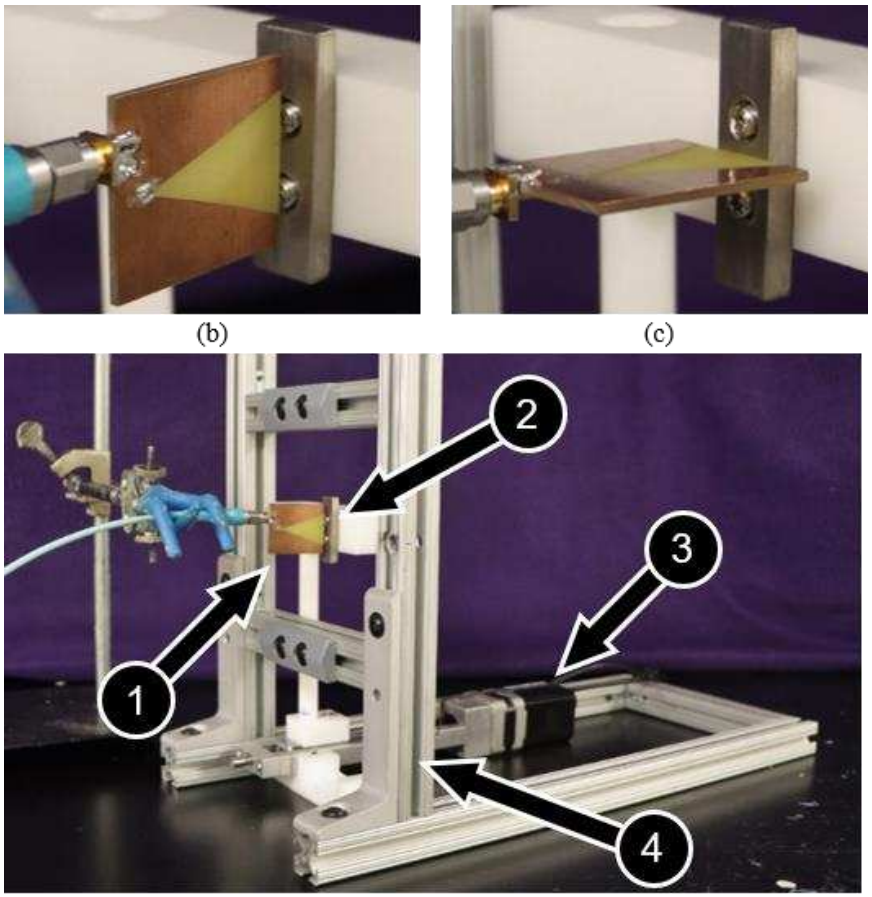

Figure 5.4: (a) The prototype antenna (1) was positioned such that it was aligned either (b) parallel or (c) perpendicular to a metallic plate. The plate was attached to a precision linear actuator (3) so that antenna-plate displacement could be precisely increased while measuring the resultant shift in resonant frequency. The antenna was surrounded by an aluminum frame (4) to recapitulate the testing environment necessary for use as an orthopaedic diagnostic device.

An additional test was performed using the miniaturized antenna, positioned perpendicular to a SS plate segment (Figure 5.4C). In this test, the antenna and plate segment were connected to separate precision linear actuators, with the movement direction of each actuator being collinear. An initial test was performed in which resonant frequency shifts were collected while displacing the plate, following the methods of the preceding paragraph. Upon test completion, the plate was returned to its initial location, and the test was repeated while instead displacing the antenna. The purpose of this study was to evaluate the hypothesis that resonant frequency shifts were repeatable for any

antenna-plate displacement scenario, regardless of which of the two members were displaced. Despite the simplicity of this test, the findings were of paramount interest for orthopaedic applications, as discussed later.

5.3 Results

5.3.1 Antenna Simulation

Figure 5.5 shows a comparison of antenna S_{11} obtained by simulations and by measurements on a fabricated prototype, in free space, using a calibrated VNA.

Figure 5.6A-B show simulated predictions of S_{11} behavior for broadband (up to 6 GHz) in the standard antenna, and near the operational frequency of interest (1.5 GHz) for the miniaturized antenna. A family of curves were obtained for various metallic plate offsets (i.e., distances from the front of the antenna). For the standard antenna, resonances were predicted around 1.5 GHz, 2.5 GHz, 3.2 GHz, 4.5 GHz and above.

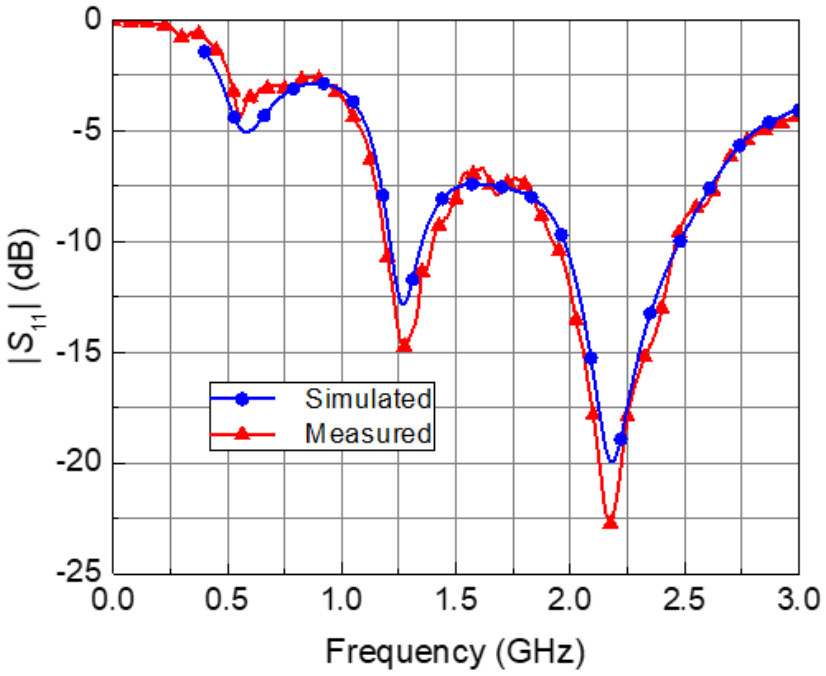

(a)

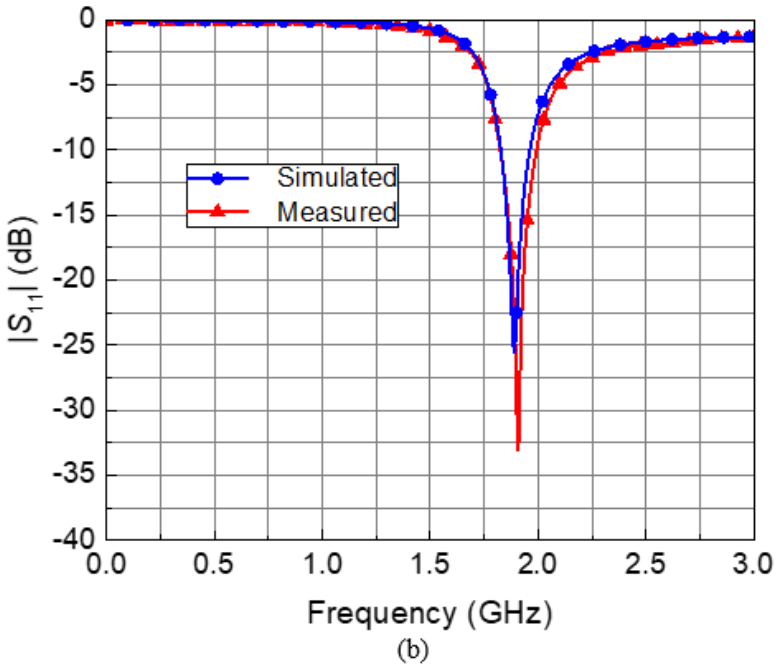

(b)

Figure 5.5: Comparison of simulated and prototype measurements of antenna S11 versus frequency for the (a) standard and (b) miniaturized antenna designs.

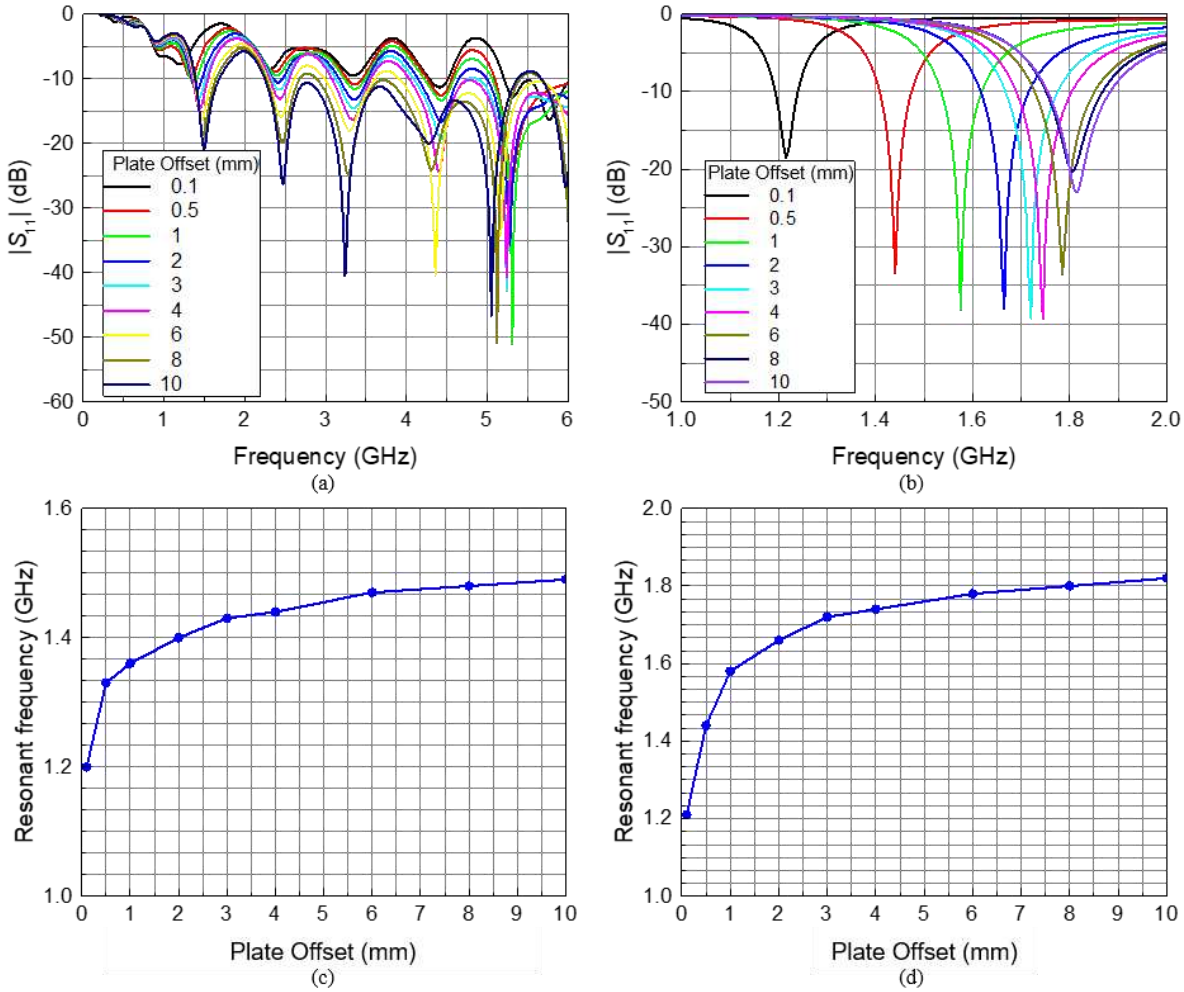

Figure 5.6: Simulated measurements of antenna S11 versus frequency for the (a) standard and (b) miniaturized antenna designs, as a function of metallic plate offset from the antenna. Resonant frequency (resonance near 1.5 GHz) for the (c) standard and (d) miniaturized antennas.

For the resonance of interest (near 1.5 GHz), resonant frequency increased non-linearly with increasing antenna-metallic plate distance (Figure 5.6C-D, Table 5.2). For both the standard and miniaturized antennas, predicted resonant frequency increases resulting from the first 1 mm of metallic plate offset (0.16 and 0.37 GHz, respectively) were greater than those for the next 9 mm of offset (0.13 and 0.24 GHz, respectively; Table 5.2).

Table 5.2: Vivaldi antenna resonances around 1.5 GHz as a function of increasing antenna-metallic plate distance.

	Standard Antenna		Miniaturized Antenna	
Plate Offset (mm)	Resonant f (GHz)	$\|S_{11}\|$ (dB)	Resonant f (GHz)	$\|S_{11}\|$ (dB)
0.1	1.20	–7.75	1.21	–18.49
0.5	1.33	–9.80	1.44	–33.44
1	1.36	–10.64	1.58	–27.57
2	1.40	–11.84	1.66	–37.94
3	1.43	–13.06	1.72	–39.23
4	1.44	–14.66	1.74	–33.96
6	1.47	–16.37	1.78	–33.58
8	1.48	–18.65	1.80	–20.28
10	1.49	–20.83	1.82	–22.99

5.3.2 Prototype Antenna Sensitivity to Metallic Structure Displacements

During physical tests, antenna resonant frequency increases were observed as the distance between antenna and SS plate segments were increased via linear actuator (Figure 5.7A-B); however, the magnitude of these increases were smallest for the standard antenna, and clear data trends were absent when this antenna was positioned perpendicular to the metal plate (Figure 5.7A).

As distance was increased from 0 – 10 mm, resonant frequency increases of 227.2 MHz and 98.5 MHz were observed for tests in which the miniaturized antenna was oriented parallel or perpendicular to a SS plate segment, respectively (Figure 5.7B). Similar analysis for a Ti plate segment yielded total resonant frequency increases of 177.7 and 58.1 MHz, respectively. For all miniaturized antenna tests, sensitivity (i.e., the instantaneous slopes at various displacement values of Figure 5.7A-B) was largest for plate-antenna distances of less than 1 mm, and tended to non-linearly decrease with increasing plate-antenna distance. For distances less than 10 mm, antenna

sensitivities were larger when the miniaturized antenna was positioned parallel, instead of perpendicular, to the plate segment (Figure 5.7D).

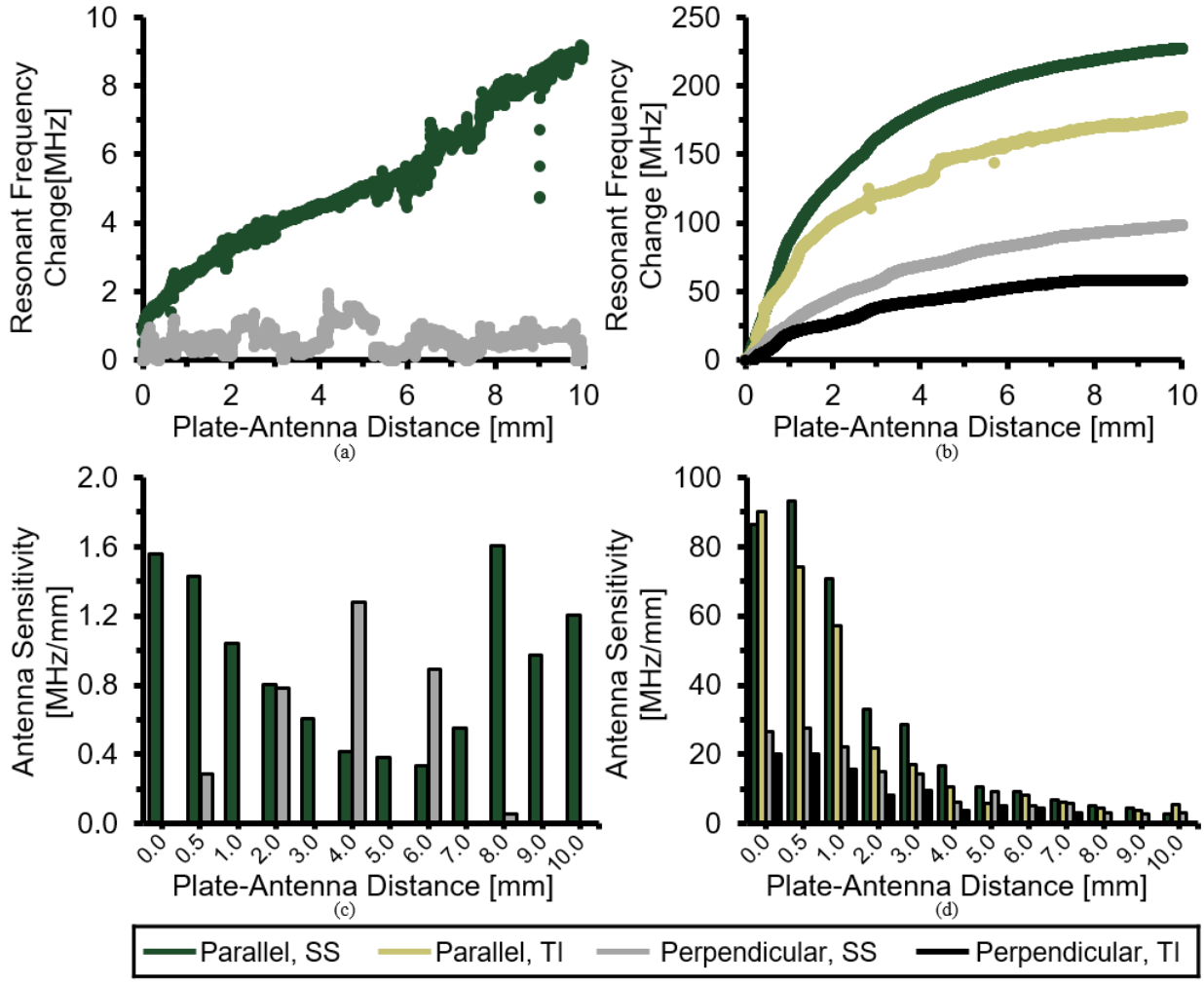

Figure 5.7: Change in resonant frequency measured while increasing distance between (A) standard or (B) miniaturized antenna and metal plate segment of SS or Ti alloy. Tests were repeated with the antenna aligned parallel or perpendicular to the plate segment (Figure 5.4). Antenna sensitivity of the (C) standard or (D) miniaturized antennas were calculated by taking the slope of a linear fit applied to a 0.5 mm window of resonant frequency shift-displacement data in (A) or (B), respectively.

Resonant frequency shifts were similar for tests in which the plate-antenna distance was increased by displacing the plate or displacing the antenna (Figure 5.8). For the first 0.5 mm of displacement, resonant frequency shifts tended to be larger for the test in which the antenna was displaced, and

the average difference in resonant frequency shift for any given plate-antenna distance in this range was 1.7 MHz. For all plate-antenna distances of 0.5 mm or larger, resonant frequency shifts for each method averaged 5.2% difference, and did not exceed 10% difference.

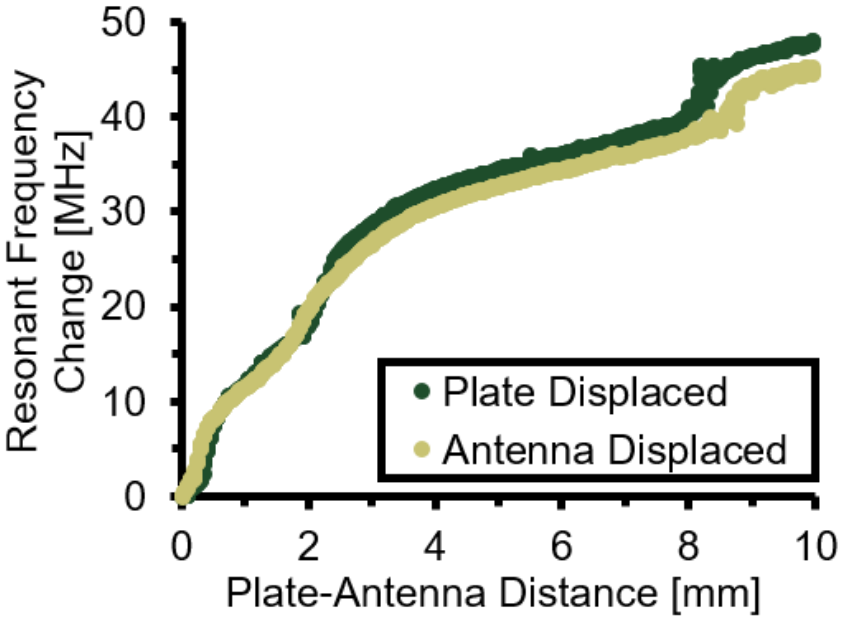

Figure 5.8: Resonant frequency shifts associated with the miniaturized antenna positioned perpendicular to a SS plate segment. Plate-antenna distance was increased by linear actuator displacement of either the plate (antenna remained stationary) or antenna (plate remained stationary).

5.4 Discussion

In silico simulations of the two proposed Vivaldi antenna designs established the efficacy of the antennas, with regards to their intended application of sensing metallic orthopaedic implant deflections, prior to fabrication. The validity of these simulations was supported by the apparent agreement in simulated and prototype measurements of antenna S_{11} versus frequency data for both antenna designs (Figure 5.5).

Computational predictions of antenna behavior, in the presence of a metallic plate, further indicate that standard antenna resonances can be observed around 1.5 GHz, 2.5 GHz, 3.2 GHz, 4.5 GHz and above. Out of these sets, the resonances around 1.5 GHz (as well as around 3.2 GHz and possibly others) are particularly favorable due to their easily distinguishable resonant frequencies, which are well separated for different plate distances (Figure 5.6A). The data of Table 5.2 support the conclusion that resonances are pronounced, sharp, well separated, and easily distinguishable by both frequency and magnitude.

The validity of these computational simulations are further bolstered by the similarity in predicted miniaturized antenna resonant frequency shift (Figure 5.6D), to the data obtained from comparable physical experiments with a prototype antenna (Figure 5.7B). Experimental agreement was worse for the standard antenna design (Figure 5.6C and Figure 5.7A), although this can ostensibly be attributed to the difference in metallic plate dimensions for the two methodologies. The computational experiments modeled a large plate segment which covered the entire antenna opening, while benchtop experiments used a smaller plate segment (intended to recapitulate the region of interest for orthopaedic applications) which covered only 20% - 40% of the measurement side of the antenna (perpendicular and parallel orientations, respectively).

We can conclude from the miniaturized antenna data sets that resonant frequency shifts are highly sensitive at small distances between a metallic object and the antenna; these sensitivities become increasingly diminished as the plate offset increases (Figure 5.7D). Benchtop results further exhibit the efficacy of the Vivaldi antennas to detect changes in antenna-plate distance for a variety of metallic alloys relevant to orthopaedic applications (i.e., stainless steel and titanium). These data,

however, advise that antenna sensitivities tend to be slightly elevated for stainless steel relative to titanium, and further suggest that sensitivity was maximized when the metallic structure covered greater portions of the measurement edge of the antenna (i.e., antenna parallel to implant). Based on these findings, it can be concluded that the miniaturized antenna is well suited to detect relative displacements of any metallic orthopaedic structure, but performance is optimized by maximizing the alignment of the antenna and implant and minimizing the initial distance between these two components.

In spite of the standard antenna design's excellent *in silico* results for the structure displacement sensing applications, this design tends to be rather large (i.e., *length* x *height* = 138 mm x 100 mm, where length = $L + L_r + 2R + L_k$ and height = $2[H + H_d]$, Figure 5.1 and Table 5.1), and exhibits poor benchtop sensitivity to small profile metallic structures (Figure 5.7C). The miniaturized antenna, however, features a total calculated *length* x *height* = 36 mm x 30 mm, which amounts to an approximately 13-fold reduction in total surface area. Despite this area reduction, comparing Figure 5.6C to 5.6D and Figure 5.7A to 5.7B, we can conclude that miniaturization of the antenna did not degrade its sensitivity performance. In fact, antenna sensitivity was actually improved substantially (i.e., the same variations in plate offsets yield even higher resonant frequency shifts in the same bandwidth). The appreciable reduction in antenna size has the additional benefit of facilitating antenna mounting to a precision linear actuator.

The results of Figure 5.8 suggest that resonant frequency changes were irrespective to whether the antenna or metallic structure was displaced to change the relative distance between the two members. Despite the perceptive triviality of this observation, these data represent a gestalt whose

clinical importance cannot be overstated. The primary limitation of direct electromagnetic coupling antennas, as an orthopaedic diagnostic tool, is the highly nonlinear relationship between resonant frequency shift and antenna-metallic structure distance (Figure 5.6 & Figure 5.7). As a clinical tool, controlled mechanical loads are applied to a fractured limb and the resultant deflections of implanted metallic structures (i.e., plates, rods, and screws used to stabilize fractured bone segments) are noninvasively measured via antenna resonant frequency shifts [97, 98, 129]. The magnitude of these shifts is highly sensitive to the initial antenna-implant distance (Figure 5.6 & Figure 5.7) [97], which cannot be accurately known nor measured in a clinical setting. Comparison of data collected from different points within the healing timeline is thus an arduous task.

The similarity of the two data profiles in Figure 5.8 confirms that knowledge of initial antenna-implant distance is unnecessary for accurate prediction of implant deflections, as long as the position of the antenna can be precisely displaced in the same direction of implant deflections. After diagnostic tests are performed (i.e., collecting resonant frequency shift per applied load), the antenna can be displaced known distances, via linear actuator, from the measurement site while assessing the resultant resonant frequency shift (i.e., resonant frequency shifts per known change in antenna-implant distance). The measured resonant frequency shift per change in antenna-implant distance can be used to calibrate the initial diagnostic test data to produce implant deflection per applied load, which is the inverse of fracture bending stiffness. This metric is essential for clinical diagnosis of fracture healing progression; thus, additional studies are warranted to further explore the ability of the proposed technique for accurate prediction of bone fracture bending stiffness.

5.5 Conclusions

The antennas developed in this study are intended for use in orthopaedic diagnostic applications. These antennas have demonstrated efficacy in remotely detecting relative deflections and/or displacements of metallic plates of alloys similar to those used to treat fractured bones. While these results are promising, it should be noted that clinically available orthopaedic fixation hardware is highly varied in structure/design/material. Regardless, the diagnostic application of this technology relies upon relative and repeated resonant frequency shifts, and thus this technology / approach is applicable to any metallic implant design that is used to mechanically stabilize any body part. However, to fully characterize the extent of clinical applicability of this technology with different implant designs and implementations, additional translational studies should be performed in translational and/or clinical models. Future studies are therefore recommended for evaluating the applicability of the miniaturized antenna for predicting healing induced bone fracture stiffness progression. These results nonetheless agree with previous antenna development studies [97], which were foundational to the development of subsequent clinical diagnostic devices [123, 129]. Previous antenna designs were notably limited by highly nonlinear antenna sensitivity, as a function of initial antenna-implant distance, which made clinical implementation of this technology challenging. The miniaturized antenna developed in this study marks a pronounced improvement of this technology due to its appreciably reduced size while still maintaining excellent antenna sensitivity. This antenna will thus enable the implementation of calibration techniques to mitigate nonlinear antenna effects, and enable direct prediction of essential indicators of bone fracture healing progress (fracture stiffness). The findings of this study will thus serve as the foundation for developing novel orthopaedic diagnostic technologies.

5.6 Footnote

Financial support for this project was provided by the National Institute of Health (NIH) - National Institute of Arthritis and Musculoskeletal and Skin Diseases (NIAMS) [R01AR069734-01 - "Early Detection and Prediction of Complex Bone Fracture Healing"], the Colorado Office for Economic Development and International Trade (CTGG1 2020-2697), and the Translational Medicine Institute at Colorado State University.

CHAPTER 6: VIVALDI DEC ANTENNA TESTING (SPECIFIC AIM 1 & SPECIFIC AIM 3)

The findings of Chapter 5 suggested Vivaldi DEC antennas to be advantageous for orthopaedic diagnostic applications due to their reduced antenna size and high sensitivity to changes in antenna-metal coupling distance. The size reduction of these antennas, relative to the coiled coaxial DEC antenna design, was sufficient to allow the Vivaldi antennas to be attached to a precision linear actuator on a diagnostic loading device, thus enabling antenna calibration. Such antenna calibration procedures enable the antenna sensitivity metrics, which were used in Chapter 4, to be directly converted into clinically relevant measurements of fracture bending stiffness. To support these improvements, a study was performed in which the accuracy of stiffness values predicted by the calibrated DEC antenna was compared to values obtained using traditional material testing methods.

Additionally, a parametric finite element (FE) model was created to support the hypothesis that fracture healing will result in predictable and quantifiable reductions in implant deflections resulting from mechanical loading of a fracture limb (Specific Aim 3). To support the validity of the behaviors demonstrated by the FE models, a parametric numerical model was created to predict implant displacements using beam theory and simplified model geometries / boundary conditions. The methods and results of this study are detailed in Appendix C and Appendix D, respectively.

The remainder of this Chapter details studies to 1) evaluate the accuracy of DEC fracture stiffness predictions and 2) predict implant deflections through parametric FE modelling, and is adapted from a full-length research article currently in peer-review at *Annals of Translational Medicine*.

6.1 Introduction

Failed bone fracture healing (nonunion and/or delayed unions) is exceedingly detrimental to patients, resulting in chronic pain, need for additional surgical intervention, increased prescription opioid usage, and a reported 118% increase in treatment costs [11, 12]. Despite ongoing advances in orthopaedic fracture fixation techniques, nonunion incidences remain prevalent, especially among long bones such as the tibia, where up to 12% of cases experience nonunion [11]. For these cases, it is clear that rapid diagnosis of adverse fracture healing is paramount for advising adjunct therapies during the early phases of healing to minimize suffering and financial burden to the patient [9, 13].

Bone fracture healing is characterized by a complex cascade of overlapping phases of inflammation, repair, and remodeling [18]; the exact coarse of fracture healing is highly influenced by the biomechanical [99] and biological environment at the fracture site [17, 138]. Infection, insufficient biological activity, and/or suboptimal mechanical fixation can all lead to cessation of healing progression [25], with the majority of nonunion causes being multi-factorial [139]. *A priori* prediction of nonunion proves exceedingly difficult due to the numerous treatment and patient specific factors contributing to nonunion [7, 128, 140]. Clinical distinction of nonunions from

delayed unions (i.e., fractures which will properly heal, albeit slowly) makes diagnosis of nonunion an especially arduous task.

Planar x-ray imaging is the prevailing fracture healing diagnostic tool; however, this technology has proven to lack specificity, and thus is limited by clinician interpretation [30, 40, 42, 109]. These inherent limitations limit the reliability of radiographic predictions of healing outcome [43] and delay the mean nonunion diagnosis time to 6.2 months [16].

Fracture bending stiffness has exhibited efficacy as a reliable [23, 50, 53, 58, 62, 133] and early predictor [61, 67] of healing outcome. Regrettably, x-ray data have been shown to be an inadequate predictor of fracture stiffness [42]. Accordingly, it is common clinical practice to augment radiographic data with semi-quantitative mechanical assessments of the fracture's stability, as determined through manual manipulation of the fracture site. These methods, however, have demonstrated insufficient accuracy in correctly predicting fracture stiffness [51].

To this end, efforts have been made to develop technologies to accurately quantify the progression of fracture biomechanics throughout the healing cascade [1, 53]. The underlying principle of these technologies results from bone segments stabilized by orthopaedic hardware behaving as a composite structure. As proper healing progresses, structural and compositional evolution of the fracture callus leads to resultant improvements in the mechanical stiffness of the fracture site. Stiffness of the bone-callus-hardware composite is accordingly increased [53], and the share of mechanical load supported by the fixation hardware is shifted to the healing callus tissues [75].

Proper healing is indicated by the progressive increase in stiffness of the composite structure, while adverse healing presents a temporally invariant stiffness [78]. It has been observed that these temporal biomechanical profiles present prior to the callus mineralization required for radiographic indicators of healing. Thus, quantitative mechanical diagnostic approaches which do not rely upon radiographic methods have exhibited success as an objective and temporally expedited predictor of fracture healing outcome [67, 96]

Mechanical diagnostic technologies have predominately targeted fractures treated via external fixation approaches due to the ease in instrumenting externally located fixation hardware for mechanical analyses [60-62, 64, 66-68, 141]. Such methods preclude application to orthopaedic fixation plates and intramedullary nails (IMN), despite their clinical ubiquity. Extensive studies have been performed to develop implantable telemetric sensors capable of measuring the mechanical state of the implant hardware and wirelessly reporting these values to external data acquisition devices [69, 78-80, 82, 83, 85-90, 92-96, 98, 111]. These devices must surmount extensive engineering design challenges associated with powering and interrogating sensors through biological tissues, and often require implant hardware geometry to be modified to accommodate sensor architecture [80, 96, 98] which increases the barriers to clinical implementation and can lead to premature / catastrophic implant failure [69].

To mitigate these limitations, our research group has developed direct electromagnetic coupling antenna (DEC) systems which noninvasively quantify relative changes in bending stiffness of fractures stabilized by any clinically available metallic implant (i.e., IMN or plate; titanium or

stainless steel). DEC is comprised of an antenna designed to couple with metal implants in its near-field to produce an apparent resonant frequency (ARF) which varies according to the distance between the coupled members [97]. Application of controlled mechanical loads, such as four-point bending, produces changes in implant displacement (i.e., deflections) of magnitude dependent upon fracture stiffness [123, 129]. Implant deflections, per applied bending load, are measured via change in antenna ARF (ARF shifts) to noninvasively quantify relative fracture stiffness. Similar to the previously discussed technologies, DEC is hypothesized to provide and early and objective prediction of fractures trending towards nonunion by elucidating cases which exhibit temporal fracture stiffness invariance prior to the presentation of radiopaque tissues.

Coiled coaxial DEC antennas have demonstrated efficacy in quantifying relative changes in fracture stiffness in cadaveric [129] and *in vivo* fracture models [123]. However, the original DEC antenna design was limited by reduced antenna sensitivity and a large antenna size. Accordingly, a novel Vivaldi style DEC antenna was designed to minimize antenna size while increasing DEC sensitivity to stainless steel and titanium implant deflections (Chapter 5). New antenna calibration methods have additionally been developed to enable antenna sensitivity (i.e., ARF shift per applied load) to be converted directly to fracture stiffness, as the latter metric is more clinically relevant.

We hypothesized this new DEC antenna design, and associated antenna calibration methods, would enable accurate noninvasive quantification of fracture stiffness. One purpose of this study is to evaluate the accuracy of fracture stiffness values predicted by this DEC diagnostic technique

by comparing with values obtained by traditional material testing methods in an ovine cadaveric fracture model.

Of additional interest are the deflections of orthopaedic implants during mechanical loading of fractured limbs, as this is foundational to the applicability of DEC as a predictor of healing outcome. These deflections are specific to the mode and magnitude of applied mechanical load, and ostensibly vary with fracture type and fixation implant selection. These highly specific factors preclude the use of existing literature to predict temporal changes in implant deflections, and exhaustive *in vivo* tests of the myriad combinations of fracture and treatment type are neither feasible nor ethical. Yet, this data is imperative for predicting the efficacy of DEC as a diagnostic tool for a variety of clinically relevant cases.

This knowledge gap can be addressed through the use of finite element (FE) analysis, which enables *in silico* simulation of bone-implant constructs during mechanical loading. FE methods additionally permit the fracture geometry, state of healing, and implant type to be rapidly and parametrically varied to evaluate implant deflections under innumerable circumstances of clinical relevance. FE and numerical analyses have frequently been implemented in fracture healing studies to evaluate the effects of implant design [142-145], implant placement [146-148], bone-implant load transfer [149-151], screw placement configurations [145, 148, 152], fracture geometry [126, 148, 153-156], and the mechanoregulation of healing [126, 157-161]. Yet to the authors' knowledge, only one prior study has implemented this technique to predict implant deflections [129], and this study was limited to a singular variation of fracture-treatment type.

Thus, an additional goal of this study was to conduct a parametric series of 1,632 finite element analyses to better characterize implant deflections. These data quantify the potential sensitivity for this new DEC system for a variety of permutations in fracture stabilization approach and fracture callus mechanical stability. Taken together, these data will have identified the efficacy and optimal applications for this new DEC system.

6.2 Methods

6.2.1 Ex Vivo Prediction of Fracture Stiffness

6.2.1.1 Fracture Stiffness Prediction by DEC Diagnostic Device

To better understand the potential of the DEC system as a diagnostic tool, it was necessary to test the accuracy of its predicted fracture stiffness values relative to standard *in vitro* methods (Figure 6.1A-E). Healthy cadaveric ovine metatarsals (Rambouillet cross, female, >3 years of age, n = 8) were obtained from animals sacrificed from unrelated studies. Sheep were selected for this study due their orthopaedic similarities to humans; namely, their similarity in body weight, bone macrostructure [119], cortical microarchitecture, and bone mineral composition [120]. A skin incision was made along the lateral midspan of the samples so that a nine-hole stainless steel locking compression plate (LCP; VP4045.09; DePuy Synthes; Warsaw, IN, USA) could be fixed to the bone via standard surgical practice. The LCP was secured to the mid-diaphysis with eight bicortical locking screws (3.5 mm diameter, 316L stainless steel). The middle screw hole was filled with a locking screw head (i.e., screw threads removed leaving only the locking head) to facilitate subsequent ostectomy at the LCP midspan [123] (Figure 6.1A). Overlaying soft tissue was restored using standard suturing techniques.

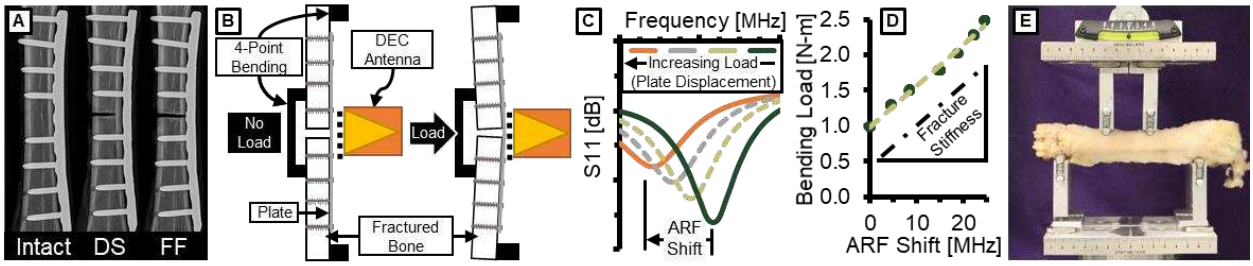

Figure 6.1: Direct electromagnetic coupling (DEC) fracture stiffness prediction methods. A) Radiographic images showing samples in an intact, destabilized (DS), and fully fractured (FF) state. B) Schematic representation of the custom DEC four-point bending device used. Application of bending loads cause the implant hardware to deflect towards the DEC antenna. C) The resultant implant deflections cause antenna resonant frequency (ARF) to shift in a predictable and measurable manner. D) The slope of the resultant load-ARF shift data was combined with calibration data to predict fracture stiffness. E) DEC predictions of fracture stiffness were compared with stiffness measurements obtained using standard *in vitro* four-point bending protocols.

Samples were placed in a custom pneumatic DEC loading fixture that controlled four-point bending loads applied to the sample, thus inducing implant deflections towards the DEC antenna positioned at the LCP midspan (Figure 6.1B). The DEC antenna was affixed to a precision linear actuator to enable the initial sample-antenna distance to be approximately 0.5 mm. Bending moment was produced by increasing the compressive force applied to the inner bending points, with resultant load cell measurements (Model 53; Honeywell; Charlotte, NC, USA) being converted to maximum bending moment based on four-point bending fixture geometry. Antenna ARF was measured via vector network analyzer (VNA) (TTR500; Tektronix; Beaverton, OR; Reflection coefficient measured from 1,550 – 1,850 MHz at 500 equally spaced points, 7 dB power) (Figure 6.1C).

Bending loads were applied to the intact sample (1.0 – 2.5 N-m, in 0.25 N-m increments, n = 5 preload cycles, and n = 5 data collection cycles per test, Figure 6.1B-D) while measuring the

resultant change in ARF shift (Figure 6.2A). Following loading cycles, an antenna calibration procedure was performed in which the antenna was displaced with a linear actuator while measuring resultant changes in ARF (-0.05 to +0.05 mm relative to antenna position during bending measurements, 0.01 mm step sizes, n = 7 data points per position, n = 5 displacement cycles per data collection). Slope of a linear fit applied to the calibration data was used to determine the expected ARF shift per change in antenna-implant distance (calibration factor, in units of ΔMHz/Δmm) for the current testing configuration (Figure 6.2B). ARF shifts from the preceding DEC bending tests were divided by this calibration factor to obtain predictions of implant displacements. Fracture stiffness was then calculated from the slope of a linear fit applied to the resultant DEC bending moment-displacement data (Figure 6.2C).

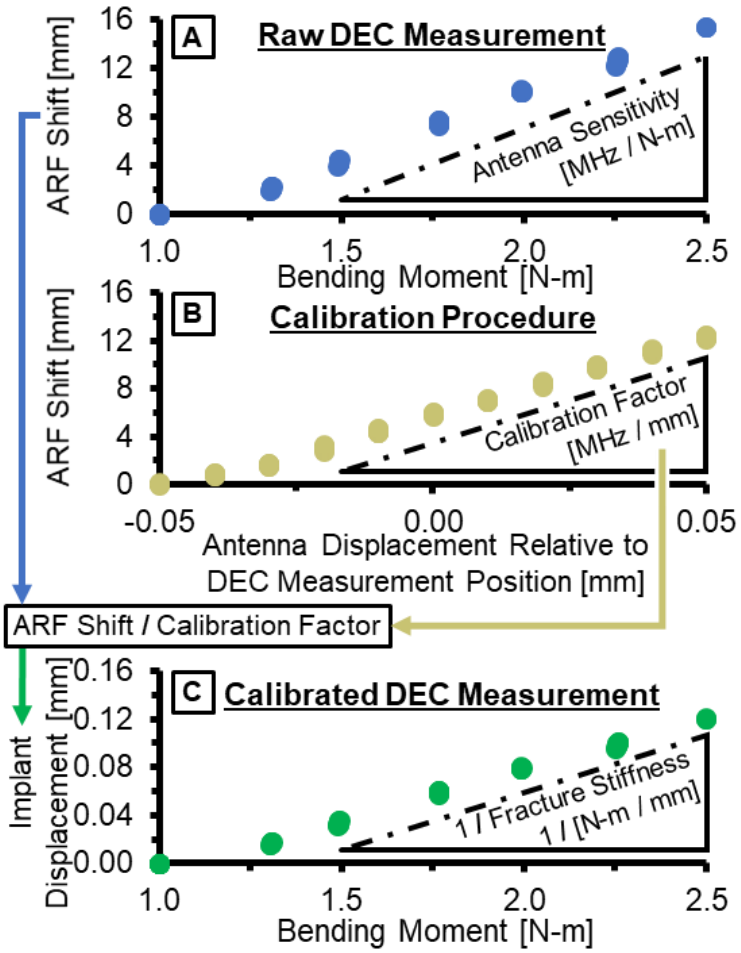

Figure 6.2: Methods for converting direct electromagnetic coupling (DEC) measurements into fracture stiffness. A) Change in apparent resonant frequency (ARF shift) is measured by the DEC antenna during four-point bending of the fracture site (Figure 6.1). B) Immediately after performing DEC bending measurements, the DEC antenna is displaced relative to the fractured limb, via precision linear actuator, to determine ARF shift for a known change in implant-antenna distance. Antenna calibration factor is obtained from the slope of a linear fit applied to the resultant ARF shift-antenna displacement data. C) ARF shifts from the DEC bending experiment (Figure 6.2A) are converted to implant displacements by dividing by the calibration factor. Fracture bending stiffness is obtained from the inverse of the slope of a linear slope fitted to the resultant implant displacement-bending moment data.

6.2.1.2 Fracture Stiffness Quantification via MT Methods

Following DEC methods, fracture stiffness was quantified using traditional material testing (MT) techniques. Samples were transferred to a servo-hydraulic MT machine (Landmark 370.02; MTS Systems Corp., Eden Prairie, MN) equipped with a four-point bending fixture of comparable

mechanical configuration to the DEC loading device (Figure 6.1E). Cyclic four-point bending loads were applied to the sample via compressive displacement of the MT crosshead (1.0 – 3.0 N-m at 0.05 mm/s cross-head displacement rate, n = 5 preload cycles, and n = 5 data collection cycles per test). Fracture bending stiffness was calculated from the slope of a linear fit applied to the moment-cross head displacement data.

After MT stiffness had been determined, destabilized (DS) and fully fractured (FF) states were created via bone saw ostectomy trans to the LCP midspan [123, 129]. DS states were characterized by removal of all but half of the cortex adjacent to the LCP; FF states were characterized by removal of the remaining cortex (i.e., cutting the bone into separate proximal and distal halves, Figure 6.1A). DEC and MT quantifications of bending stiffness were performed for each sample, in all fracture states, using the aforementioned methods.

6.2.1.3 Study Design

The progressive fracture destabilization technique precluded blinded testing and randomized treatment / fracture state, but the order of DEC and MT tests of each fracture state were randomly decided by random number generation. Sample size was determined *a priori* according to a previous study where statistically significant differences in DEC measurements of *ex vivo* simulated fracture state (i.e., using a cadaveric fracture model identical to this study), and in postmortem MT measurements of ovine fracture bending stiffness, were apparent using an identical sample size (n = 8) [123]. In the current study, animal confounders were not thought to be substantive for cadaveric *ex vivo* states, and thus were not controlled. Ethical committee

approval was not required due to samples being retrieved from animals sacrificed for unrelated purposes. A singular exclusion criterion was implemented such that selected cadaveric samples featured sufficient metatarsal length to accommodate the LCP geometry. Individual data points were not omitted.

6.2.1.4 Statistical Analysis

Following statistical tests of equal variance, fracture bending stiffness values for each technique and fracture state were statistically compared using a two-way repeated measures analysis of variance (ANOVA) with post-hoc Tukey Test (α =0.05, Minitab 18; Minitab LLC; State College, PA, USA).

6.2.2 Finite Element Predictions of Implant Deflections

6.2.2.1 Model Generation

While direct calculation of fracture stiffness in a relatively simplistic cadaveric model is possible using the methods of the previous section, comparable analysis of the innumerable permutations of fracture and treatment type, over the continuous stages of healing (i.e., the gradient in elastic modulus of the callus during healing), is not feasible using *in vivo* or *ex vivo* models. Yet these data are vital to inform the DEC approach; specifically, these data can validate the foundational hypothesis that for all fracture and treatment types, healing induced changes to callus stiffness result in quantifiable reduction in implant bending deflections. To this end, 1,632 finite element (FE) analyses were performed to predict implant deflections for parametric variations of fracture

elastic modulus (n = 17), fracture size (n = 8), implant treatment type (n = 2), implant size (n = 3), and implant material (n = 2).

CT images of a healthy ovine metatarsal (Figure 6.3A) were segmented using open source medical image processing software (ITK-SNAP, Version 3.8.0) [162] to produce a surface mesh of the bone geometry. This was then converted to a three-dimensional part file to make geometric modifications (Figure 6.3B) corresponding to fracture and treatment type (SOLIDWORKS 2018 SP5.0; Dassault Systèmes; Vélizy-Villacoublay, France). Three dimensional part files were also generated for a LCP and locking screws of comparable geometry to those used in the prior cadaveric study, and for an intramedullary nail (IMN) (7 mm diameter, 147 mm length, two 3.5 mm pins for securing the proximal and distal ends). The LCP geometry was modeled to follow the lateral contours of the metatarsal geometry, similar to what would be used in a clinical environment (Figure 6.3C).

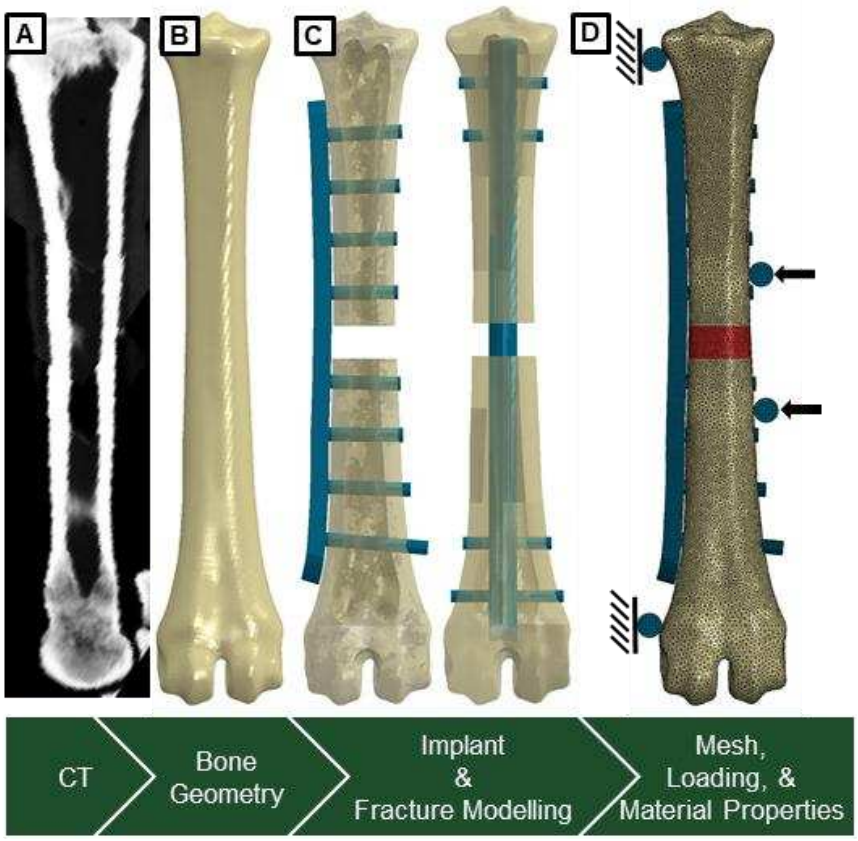

Figure 6.3: Methods of finite element (FE) analysis of fracture healing. A) Computed tomography (CT) images were collected of an ovine metatarsal and B) segmented into a three dimensional model. C) An osteotomy fracture was modeled and the bone fragments were stabilized by either locking compression plates (LCP) or intramedullary nails (IMN). D) A mesh, of density determined via convergence study, was assigned and four-point bending loads were applied to produce 2 N-m maximum bending load. The type, material, and structure of fixation hardware (blue) was parametrically varied, as were the material properties and height of the osteotomy / endosteal callus (red). Deflection at the implant midspan nodes was measured for all models.

Additional models were generated for LCP and IMN with approximately 50% increased and 50% decreased structural stiffness based upon changes in their cross-sectional geometry (i.e., +/- 50% of original sections' second moment of area in the direction of applied bending). LCP were thus modeled with a thickness of 3.57, 4.50, or 5.15 mm; IMN were modeled with a diameter of 5.88, 7.00, or 7.75 mm. The metatarsal geometry required modification to accommodate the different types of hardware fixation: three models were created with intramedullary reaming for the corresponding IMN sizes, and a single model was created for the LCP models. To analyze the

effect of osteotomy fracture size, separate geometric models were created featuring mid-diaphyseal fractures with non-reduced fracture gaps varying from one to eight mm, in one mm increments. A 1.0 index fracture callus (i.e., no periosteal callus) was modelled within the fracture gap. Thus, 32 total metatarsal geometry models were created to account for all parametric combinations of treatment and fracture type.

All models were imported into Abaqus (CAE 2019; Dassault Systèmes; Vélizy-Villacoublay, France) for subsequent meshing and FE analysis. The modeled orthopaedic hardware was meshed using 8-node linear hexahedral (C3D8R) elements, while the metatarsals were assigned 10-node quadratic tetrahedral (C3D10) elements to better accommodate the inherent geometric complexity of the bone (Figure 6.3D). All materials were assigned isotropic linear elastic material properties with exception to the cortical bone which was treated as transversely isotropic linear elastic [163]. The material properties of the fracture callus were assumed to be spatially homogenous and the elastic modulus was parametrically varied to produce 17 values logarithmically spanning from 0.1% to 100% of cortical bone (Table 6.1). Implant fixation hardware was parametrically assigned material properties corresponding to stainless steel (SS) or titanium (Ti). The effects of epiphyseal trabecular bone were assumed to be negligible based on the region of interest being the diaphyseal midspan and the epiphyses being located in regions of zero applied bending moment, thus trabecular bone was not included in these models.

Table 6.1: Material properties assigned to the finite element (FE) model.

Material	Elastic Modulus	Poisson Ratio
Cortical Bone	†E_1 = 17.0 GPa	ν_{12} = 0.48
	E_2 = 11.5 GPa	ν_{23} = 0.40
	E_3 = 11.5 GPa	ν_{31} = 0.48
Stainless Steel	E = 193 GPa	ν = 0.29
Titanium	E = 110 GPa	ν = 0.34
Callus	‡E = [% of Cortical E_1] [1.0, 2.5, 5.0, 7.5]×10^{-2}, [1.0, 2.5, 5.0, 7.5]×10^{-1}, [1.0, 2.5, 5.0, 7.5]×10^{0}, [1.0, 2.5, 5.0, 7.5, 10]×10^{1}	ν = 0.30

†Subscripts denote the material direction, with 1 being longitudinal while 2 and 3 represent the orthotropic (transverse) directions [163]; subscripts are omitted for materials modelled as isotropic. ‡Callus elastic modulus was parametrically increased, as a percentage of cortical bone, as an approximation of fracture healing.

To represent perfect screw fixation (i.e., no screw loosening), a tied constraint was applied at the interface between hardware members (i.e., locking screw heads to the LCP, or bolts to the IMN) and between bone and the fixation hardware (i.e., locking screw cortical threads or bolts to cortical bone). The loading and boundary conditions were assigned to match the *in vitro* four-point bending load used for DEC analysis (Figure 6.3D). The inner and outer contact points of four-point bending device were modeled as rigid cylinders of 6 mm diameter, and were symmetrically positioned such that the fracture site was centered between the contact points. The outer bending points were assigned encastre boundary conditions while equal point loads were assigned to each of the inner bending points in order to produce a 2 N-m moment between the inner points. The primary data

of interest for all models was the implant's midspan deflection, as measured by the displacement in the direction of applied load for nodes located at the implant midspan.

6.2.2.2 Mesh Convergence Study

A parametric mesh refinement study was performed to ensure that results were not influenced by inadequate mesh resolution. For both the LCP and IMN models, mesh convergence was performed using the parametric variation featuring 8 mm fracture, callus modulus of 0.01% of cortical bone, and standard hardware geometry. For the LCP model, four models with identical geometry and loading conditions were analyzed, with models being labeled Low (139,388 elements), Medium (239,195 elements), High (467,443 elements), and Extra High (773,909 elements). For all models, implant midspan deflection was predicted and total strain energy was calculated for the cortical bone, callus, and implant hardware regions of interest (ROI). Mesh refinement beyond the High density model caused implant deflection and strain energy in the callus and cortical bone to change by less than 4%. Further mesh refinement of the implant hardware in the High density model caused the implant deflection and strain energy in all ROIs to change by less than 3%. This refined High density model (549,011 elements) was thus deemed to be fully converged.

Similar mesh convergence was performed in the IMN model with Low (84,505 elements), Medium (163,020 elements), High (318,626 elements), and Extra High (663,267 elements). Mesh refinement beyond the High density model caused implant deflection and strain energy in the cortical bone and hardware to change by less than 4%. Further mesh refinement resulted in implant deflection and strain energy in all ROI to change by less than 3%; thus, this refined High density

model (382,909 elements) was deemed to be fully converged. The converged mesh resolutions from this sub-study were applied to all parametric analysis variations, although exact element counts varied slightly due to difference in model geometries.

6.2.2.3 Strain Gage Validation

To validate the accuracy of the FE models, strain results were compared between *in vitro* and *in silico* tests. Cadaveric metatarsals (n = 10) were obtained from animals sacrificed for unrelated studies, and all soft tissue was removed. All samples received a mid-diaphyseal ostectomy via bone saw, and half of the samples were stabilized via LCP while the others were stabilized via IMN. The hardware and fracture model were selected to recapitulate the parameters of the mesh validation models. Using standard strain gauge application techniques, stacked strain rosettes (C2A-06-062WW-350; Micro-Measurements; Raleigh, NC, USA) were adhered to the cortical bone between the two screws proximal to the fracture site (i.e., to avoid excessive strain gradients resulting from the screw holes of the LCP hardware), or to the IMN midspan. Samples were placed in a MT equipped with a four-point bending fixture of configuration mechanically comparable to the FE model loading conditions. Static four-point bending loads were applied (2.0 N-m, n = 5 preload cycles from 0.0 – 3.0 N-m, and n = 5 data collections per test) while maximum principal strain was measured using a custom data collection code (LabVIEW 2019; National Instruments; Austin, TX, USA).

Maximum principal strain from the two fully converged FE models were independently averaged from regions of comparable area to the strain rosettes (n = 10 nodes and n = 9 nodes for the LCP

and IMN models, respectively). For both fixation methods, mean FE strain values were within one standard deviation of experimental strains, thus the FE models were deemed validated.

6.3 Results

6.3.1 Ex Vivo Prediction of Fracture Stiffness

When quantifying fracture bending stiffness for progressively destabilized cadaveric fractures, no significant differences were observed for any fracture state for values obtained via MT methods versus DEC methods ($p = 0.587$, $p = 0.985$, $p = 0.975$; for intact, DS, and FF comparisons; respectively). Traditional MT techniques measured mean stiffness values of 19.6 ± 5.8, 17.4 ± 6.6, and 10.3 ± 2.4 N-m/mm for the intact, DS, and FF, respectively. Mean DEC stiffness predictions were not significantly different from the MT values, with values of 23.3 ± 4.5, 18.9 ± 9.0, and 11.9 ± 2.4 N-m/mm for the intact, DS, and FF, respectively. For both the MT and DEC techniques, means stiffness values were significantly lower for the FF state than the intact ($p < 0.001$ & $p = 0.002$, respectively) and DS ($p = 0.030$ & $p = 0.036$, respectively) states (Figure 6.4). Calibrated DEC results predicted an 82.2 μm reduction in mean implant bending deflection from intact to FF states.

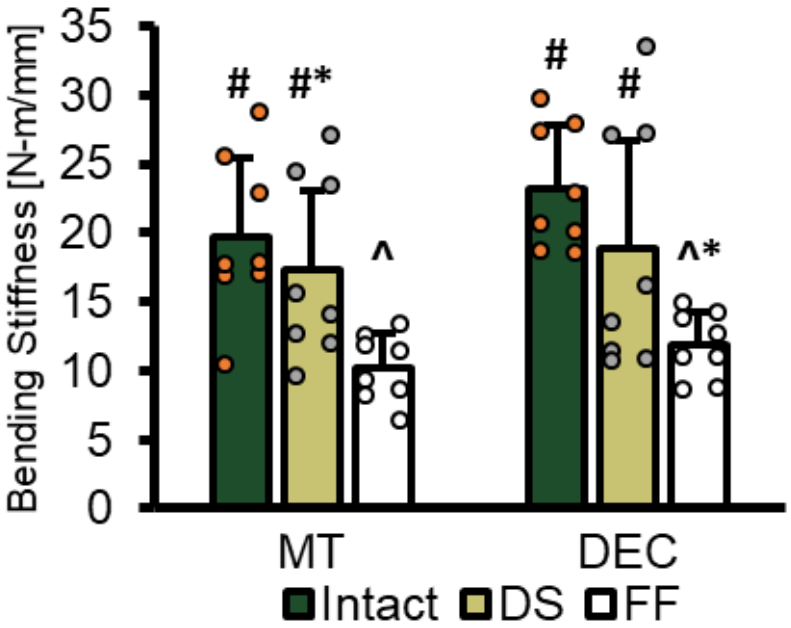

Figure 6.4: Fracture bending stiffness predictions. Bending stiffness of cadaveric metatarsals of decreasing stability levels (i.e., intact, destabilized [DS], and fully fractured [FF] states) were measured using material testing (MT) methods and direct electromagnetic coupling (DEC) predictions. Bars depict mean + standard deviation, where overlaid points correspond to the mean values of each sample (n = 8). Bars which do not share symbols (#, *, ^) are significantly different ($p < 0.05$).

6.3.2 Finite Element Predictions of Implant Deflections

Parametric FE predictions of implant midspan deflections during four-point loading have been separated into individual semi-log charts according to the implant treatment type (Figure 6.5). The largest change in implant deflection (i.e., difference in implant deflections predicted at callus moduli of 0.01% and 100% of cortical bone) was 267.9 μm for the case of an 8 mm fracture treated via reduced stiffness Ti LCP; however, the greatest individual instance of implant deflection, 316.0 μm, was observed at initial fracture (i.e., callus modulus = 0.01% of cortical bone) for an 8 mm fracture treated via reduced stiffness Ti IMN. The smallest predicted displacement was 24.43 μm and occurred at full healing (i.e., callus modulus = 100%) for the 1 mm fracture stabilized by increased stiffness SS LCP.

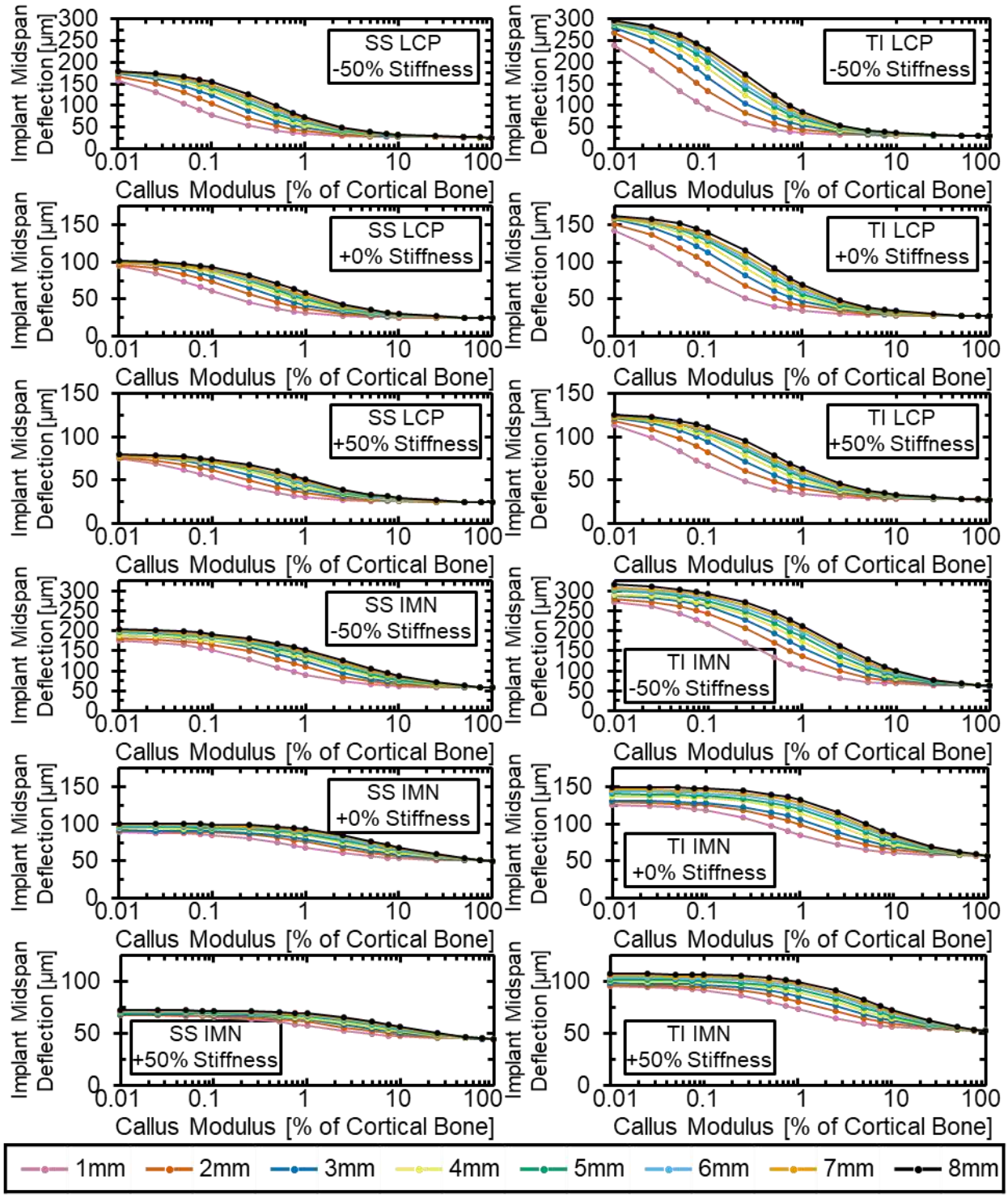

Figure 6.5: Parametric finite element (FE) predictions of implant deflections resulting from the application of experimentally equivalent four-point bending loads. Different colors correspond to the parametrically varied osteotomy fracture height. Each chart corresponds to a unique permutation of fracture fixation type (i.e., stainless steel [SS] or titanium [Ti] implant material, locking compression plating [LCP] or intramedullary nailing [IMN], & implant stiffness altered via modification to cross-sectional geometry).

When fully healed, displacements for all fracture types within a given treatment permutation (i.e., callus modulus of 100% for all points within any individual plot Figure 6.5) exhibited a set of values with standard deviations less than 0.5% of their mean, thus indicating convergence. At initial fracture, displacements for all fracture types within a given treatment permutation exhibited a set of values with standard deviations less than 7% of their mean. For the average stiffness SS model (i.e., comparable parameters to the fracture model used for *ex vivo* testing), mean implant displacement decreased by 74.7 μm from fully fractured to fully healed states (Figure 6.5).

6.4 Discussion

When destabilizing fractures, MT methods found significant differences in the bending stiffness of FF relative to DS and intact states. This supports the use of a progressive destabilization as a chronologically reversed approximation of fracture healing mechanics. DEC methods were similarly able to detect significant differences in FF stiffness relative to DS and intact states. Of primary interest to this study was the ability of DEC to accurately predict the magnitude of stiffness. For all fracture states, DEC predictions of fracture stiffness were not significantly different from values obtained by MT testing values (Figure 6.4).

While traditional MT methods are a gold-standard technique for quantifying structural properties in a laboratory setting, they are neither safe nor feasible for use as a clinical diagnostic tool. The data of this study, however, suggest DEC can predict fracture bending stiffness to within 25% difference of MT methods, with no significant differences in values measured by each method for

any fracture state. Unlike MT devices, DEC is highly portable and noninvasive, and therefore well suited for use as a diagnostic tool in clinical or home tele-medicine applications.

The present results agree with previous DEC studies with regards to the ability of this technology to detect implant deflections [97] and differences in fracture stiffness [123, 129]. These studies showed success in using relative temporal changes in DEC antenna sensitivity to indicate the healing trajectory; however, the large antenna designs used in these early studies precluded the use of linear actuator antenna calibration procedures requisite for converting antenna sensitivity into fracture bending stiffness. The antenna sensitivity data provided by previous antenna versions are less clinically intuitive than fracture stiffness, and require continuous data to indicate relative changes in fracture stiffness. Thus, missed measurements during early healing, when using the previous antenna design, would potentially limit the predicative efficacy of DEC.

This study marks a substantial improvement in this technology due to the implementation of antenna calibration methods to accurately convert DEC measurements into fracture stiffness. Fracture stiffness is an absolute metric which can be obtained and interpreted at any point during the healing cascade, and provides an objective indication of healing status. It has been shown that human fracture stiffness magnitude of 15 N-m/degree is an effective benchmark to diagnose fracture union [62, 141] and temporal changes in fracture stiffness can predict healing outcome 2.5 weeks prior to radiographic diagnosis [67]. Thus, the demonstrable accuracy of DEC quantifications of fracture stiffness supports the conclusion that this technique will provide clinical utility for early prediction of fracture healing outcome.

The cadaveric simulations of this study exhibit compelling results for DEC as a diagnostic tool, but it should be noted that this fracture model implemented a simplified approximation of fracture healing for a single selection of fracture stabilization hardware. In a clinical setting, fracture healing progression is a continuous process and the permutations of fracture and treatment type are innumerable. These studies also utilized an ovine cadaveric model, which have intrinsic structural differences in bone structure relative to humans. Additional translational studies will therefore be pursued to better establish the efficacy of DEC in a clinical setting.

Despite these limitations, the mechanical behaviors necessary to DEC measurements were predicted for a large volume of fracture-treatment types using FE methods, hence obviating the need for excessive animal experimentation. Results of the current parametric FE study support the foundational hypothesis that implant deflections during four-point bending decrease in accordance with healing induced increases in callus bending rigidity. FE and DEC cadaveric simulations of comparable fracture fixation models aligned closely, with total predicted implant bending deflection reduction (fully fractured to fully intact states) agreeing within 10% (74.7 and 82.2 μm, respectively).

For all permutations of fracture and treatment type, FE implant displacement predictions decreased non-linearly with increasing callus elastic modulus (Figure 6.5). These results agree with the findings of Richardson *et al.* [62] which, in human clinical tibia fracture treated via external fixation, found fracture stiffness to non-linearly increase over time. This temporal stiffness profile was characterized by exponential increase during the early stages of healing, followed by a plateau

upon reaching the stiffness of an intact tibia. The results of this clinical study agree closely with the profiles observed in Figure 6.5, assuming an inverse relationship between implant deflection and fracture stiffness.

All FE fracture models for a given fracture type featured similar implant displacements at initial fracture, and converged to a common displacement at fully healed states, but paths between these two points varied considerably (Figure 6.5). Small fracture gaps exhibited rapid reductions in implant deflections for small increases in callus modulus, while increasing fracture gap size delayed this reduction. This effect became increasing pronounced with decreasing stiffness of fracture fixation hardware (i.e., using Ti versus SS, or implant structures of -50% versus +50% inherent stiffness). These findings suggest that the total magnitude of implant deflection / stiffness changes throughout proper healing, as measured via DEC, is influenced exclusively by fixation implant type and callus mechanics, and is irrespective of fracture size. However, it should be noted that this observation neglects the effects of fracture size on callus formation in a clinical setting (i.e., not all callus will present with the structural and material homogeneity assumed in this study).

In all cases, increases in hardware stiffness decreased the total change in implant deflections throughout the healing duration. Implant deflections are foundational to DEC predictions of fracture stiffness; thus, these data suggest that DEC is especially well suited for cases with less rigid fracture fixation. For example, fractures with increased stiffness SS IMN fixation exhibit relatively low change in deflections, therefore repeated DEC measurements can be expected to be exhibit similar temporal stiffness for fractures trending towards union (i.e., callus elastic modulus

increasing) and for fractures trending towards adverse healing (i.e., callus elastic modulus is invariant). Conversely, properly healing fractures treated by Ti LCP fixation exhibit large implant deflection reductions during the early stages of healing, and therefore will provide clear differences in temporal stiffness profiles of fractures trending towards proper union (i.e., stiffness progressively increases) and those trending towards adverse healing (i.e., stiffness is invariant).

Significant differences in DEC fracture stiffness were observed between the intact and FF states, suggesting that changes in implant deflections exceeding 82.2 μm (i.e., total predicted implant deflection reduction using calibrated DEC) can be confidently detected for indicating healing state. FE results indicate average total deflection reductions to be approximately equal to (within 10%) or exceeding this benchmark for all but the most rigid implant designs (53.5, 44.4, 48.5, 25.2 μm; for models of increased stiffness SS LCP, mean stiffness SS IMN, increased stiffness Ti IMN, and increased stiffness SS IMN; respectively). *In vitro* experiments of the current study were not designed to specifically elucidate the minimum deflection resolution of the DEC antenna, therefore future studies will be conducted to better characterize the efficacy of DEC for these highly rigid treatment types.

As with the cadaveric study, this FE analysis is somewhat limited by its simplistic approximation of fracture healing. Modeled fracture types were limited to mid-diaphyseal transverse fractures, and callus was assumed to be of index 1.0 (i.e., no periosteal callus formation) with spatially homogeneous material properties. In a clinical setting, fracture healing is more complex with inhomogeneous material and structural modifications in response to the mechanical environment

of the fracture site [99]. While advanced FE models of fracture healing can implement such analysis [164, 165], it was deemed unnecessary for this study as any callus of inhomogeneous structure / composition will feature an overall structural rigidity comparable to some point within the range of materials tested in this study (i.e., the rigidity falls some point between the 0.01% and 100% callus models tested herein).

It is important to clarify that the dependent variable presented in Figure 6.5 is callus elastic modulus, which does not directly correspond to healing time. Clinical fracture healing is a highly variable process, thus mapping callus modulus to healing time cannot be done with any level of confidence, especially when considering that increased fracture gaps are known to exhibit delayed healing [99].

This cadaveric study is not a perfect representation of clinical fracture healing, but provides a reasonable approximation of what can be expected of DEC at the extrema of the fracture healing cascade (i.e., fully fractured and fully healed), and FE results further bolster the validity of the mechanics foundational to DEC for a large volume / variety of fracture and hardware stabilization types. The results of the current study indicate that the novel Vivaldi antenna style DEC antenna exhibits the same diagnostic traits of previous coiled-coaxial cable designs, yet with a smaller antenna profile and increased sensing resolution. Additionally, the calibration methods presented provide a means to accurately quantify fracture stiffness, thus marking a pivotal step forward for the clinical translatability of this technology.

The small antenna footprint and its demonstrated accuracy in quantifying objective metrics of fracture healing provide a path to utility in clinical and/or home tele-medicine settings, where it will augment radiographic imaging to improve the time and confidence of adverse healing diagnoses. Thus, the results of these experiments warrant additional studies of this technology, to better characterize the efficacy of this novel diagnostic tool in a clinically translatable fracture model.

6.5 Footnote

All authors listed were involved in the study design, data collection, data interpretation, and preparation of the attached manuscript. All authors have read and approved of the submitted manuscript.

6.5.1 Funding

This project was supported by the National Institute of Health (NIH) - National Institute of Arthritis and Musculoskeletal and Skin Diseases (NIAMS) [R01AR069734-01 - “Early Detection and Prediction of Complex Bone Fracture Healing”].

6.5.2 Reporting Checklist

The authors have completed the ARRIVE reporting checklist.

6.5.3 Conflicts of Interest

All authors have completed the ICMJE uniform disclosure form. Funding for this project was supported by the NIH-NIAMS. Additional funding from the NIH and Colorado Office of Economic Development and International Trade (COEDIT) supported related research, but did not directly support this presented work. J. Wolynski and Drs. Labus, Puttlitz, and McGilvray are authors of pending and issued patents related to the DEC technology presented in this manuscript.

6.5.4 Ethical Statement

The authors are accountable for all aspects of the work in ensuring that questions related to the accuracy or integrity of any part of the work are appropriately investigated and resolved.

CHAPTER 7: SUMMARY & CONCLUSIONS

This project reflects the inherent necessity of iterative design when developing novel technologies. While this research embarked seeking to predict adverse fracture healing with the use of bioMEMS sensors to telemetrically monitor implant surface strains, the current diagnostic iteration (i.e., DEC) utilizes entirely different biomechanical engineering principles. Despite the promising results demonstrated by early benchtop studies of the bioMEMS, *in vivo* studies elucidated considerable limitations to this technology; namely, sensors being damaged / removed from fracture fixation hardware during surgical implantation, thus necessitating implant hardware modification to protect sensor architecture, which limits clinical applicability and appreciably reduces implant safety. A new technology based on quantification of mechanically induced implant deflections, rather than implant surface strains, was thus developed to surmount these challenges. This DEC diagnostic technology enables the use of unmodified metallic implants which further reduces regulatory hurdles for clinical implementation.

A series of benchtop experiments were performed to develop and characterize a DEC antenna from coiled cables, which was then developed into a multi-location antenna array. The efficacy of this antenna for quantifying changes in fracture stiffness was established using *in vitro* simulations of fracture healing and subsequent *in vivo* translational fracture models. Once again, these *in vivo* studies clarified unforeseen limitations in the design of the technology. The foremost limitation was the large antenna size which reduced spatial specificity of the diagnostic measurement, limited the ability to perform multi-location measurements to reduce data artifacts from off-target biomechanical effects (limb rigid body displacements), and precluded the ability to calibrate

antennas to convert antenna sensitivity measurements into clinically useful measurements of fracture stiffness.

Collaborative efforts facilitated the development of a third technology iteration which utilized a Vivaldi style design to substantially reduce the DEC antenna size. The improved form factor of this antenna has facilitated the implementation of newly developed antenna calibration procedures which have demonstrated efficacy in enabling accurate quantification of fracture site bending stiffness using DEC methods. Benchtop studies support the use of this most recent antenna design for measuring metallic implant deflections as a means to predict proper versus adverse fracture healing. Extensive parametric FE simulations suggest this technology to be feasible for diagnostic implementation in a large variety of clinically relevant permutations of fracture and treatment type. FE results, however, also suggest that this diagnostic technique may be less appropriate for highly rigid fracture fixation types, where implant deflections resulting from mechanical loading are minimal.

While the extensive research of this project suggests DEC diagnostic techniques may potentially present a paradigm shift in early recognition and prediction of adverse fracture healing outcomes, continued testing of this technology remains necessary. Future works will benefit from additional *in vivo* comparative fracture studies to better evaluate the efficacy of the newest antenna design and calibration methods in a clinically translatable environment. It is advised that future studies explore the use of intramedullary nail fracture fixation techniques to better characterize the ability of DEC to perform measurements through cortical bone. Furthermore, these studies would benefit

from the implementation of multiple Vivaldi DEC antennas to evaluate whether fractured limb rigid body displacements can be mitigated using DEC measurements at multiple locations, simultaneously. Positive results from this recommended line of studies would support progressing DEC diagnostic technologies to clinical trials, where its predictive efficacy can be directly compared to current standard diagnostic modalities.

In summation, the findings of this doctoral research support the continued development of DEC as a tool for early diagnostic prediction of adverse bone fracture healing. There remains a need for ongoing development and testing, but the technologies / techniques developed in this body of work may feasibly one day see clinical orthopaedic implementation to improve standard of practice and reduce patient suffering.

REFERENCES

1. Amin, S., et al., *Trends in fracture incidence: a population-based study over 20 years.* J Bone Miner Res, 2014. **29**(3): p. 581-9.

2. Darder, A. and F. Gomar, *A series of tibial fractures treated conservatively.* Injury, 1975. **6**(3): p. 225-35.

3. Tzioupis, C. and P.V. Giannoudis, *Prevalence of long-bone non-unions.* Injury, 2007. **38 Suppl 2**: p. S3-9.

4. Ekegren, C.L., et al., *Incidence, Costs and Predictors of Non-Union, Delayed Union and Mal-Union Following Long Bone Fracture.* Int J Environ Res Public Health, 2018. **15**(12): p. 2845.

5. Metsemakers, W.J., et al., *Individual risk factors for deep infection and compromised fracture healing after intramedullary nailing of tibial shaft fractures: a single centre experience of 480 patients.* Injury, 2015. **46**(4): p. 740-5.

6. Tay, W.H., et al., *Health outcomes of delayed union and nonunion of femoral and tibial shaft fractures.* Injury, 2014. **45**(10): p. 1653-8.

7. Calori, G.M., et al., *Risk factors contributing to fracture non-unions.* Injury, 2007. **38 Suppl 2**: p. S11-8.

8. Copuroglu, C., G.M. Calori, and P.V. Giannoudis, *Fracture non-union: who is at risk?* Injury, 2013. **44**(11): p. 1379-82.

9. Heckman, J.D. and J. Sarasohn-Kahn, *The economics of treating tibia fractures. The cost of delayed unions.* Bull Hosp Jt Dis, 1997. **56**(1): p. 63-72.

10. Mills, L.A., S.A. Aitken, and A. Simpson, *The risk of non-union per fracture: current myths and revised figures from a population of over 4 million adults.* Acta Orthop, 2017. **88**(4): p. 434-439.

11. Antonova, E., et al., *Tibia shaft fractures: costly burden of nonunions.* BMC Musculoskelet Disord, 2013. **14**: p. 42.

12. Brinker, M.R., et al., *The devastating effects of tibial nonunion on health-related quality of life.* J Bone Joint Surg Am, 2013. **95**(24): p. 2170-6.

13. Kanakaris, N.K. and P.V. Giannoudis, *The health economics of the treatment of long-bone non-unions.* Injury, 2007. **38 Suppl 2**: p. S77-84.

14. Hak, D.J., et al., *Delayed union and nonunions: epidemiology, clinical issues, and financial aspects.* Injury, 2014. **45 Suppl 2**: p. S3-7.

15. Phieffer, L.S. and J.A. Goulet, *Delayed unions of the tibia.* J Bone Joint Surg Am, 2006. **88**(1): p. 206-16.

16. Bhandari, M., et al., *A lack of consensus in the assessment of fracture healing among orthopaedic surgeons.* J Orthop Trauma, 2002. **16**(8): p. 562-6.

17. Claes, L., S. Recknagel, and A. Ignatius, *Fracture healing under healthy and inflammatory conditions.* Nat Rev Rheumatol, 2012. **8**(3): p. 133-43.

18. Oryan, A., S. Monazzah, and A. Bigham-Sadegh, *Bone injury and fracture healing biology.* Biomed Environ Sci, 2015. **28**(1): p. 57-71.

19. McKibbin, B., *The biology of fracture healing in long bones.* J Bone Joint Surg Br, 1978. **60-B**(2): p. 150-62.

20. Perren, S.M., *Evolution of the internal fixation of long bone fractures. The scientific basis of biological internal fixation: choosing a new balance between stability and biology.* J Bone Joint Surg Br, 2002. **84**(8): p. 1093-110.

21. Claes, L.E. and C.A. Heigele, *Magnitudes of local stress and strain along bony surfaces predict the course and type of fracture healing.* J Biomech, 1999. **32**(3): p. 255-66.

22. Einhorn, T.A. and L.C. Gerstenfeld, *Fracture healing: mechanisms and interventions.* Nat Rev Rheumatol, 2015. **11**(1): p. 45-54.

23. Marsh, D., *Concepts of fracture union, delayed union, and nonunion.* Clin Orthop Relat Res, 1998. **355S**(355 Suppl): p. S22-30.

24. Fisher, J.S., et al., *Radiologic evaluation of fracture healing.* Skeletal Radiol, 2019. **48**(3): p. 349-361.

25. Giannoudis, P.V. and N.K. Kanakaris, *Non-unions*, in *Trauma and Orthopaedic Classifications: A Comprehensive Overview*, N.G. Lasanianos, N.K. Kanakaris, and P.V. Giannoudis, Editors. 2015, Springer London: London. p. 529-532.

26. Thomas, J.D. and J.L. Kehoe, *Bone Nonunion*, in *StatPearls*. 2021, StatPearls Publishing Copyright © 2020, StatPearls Publishing LLC.: Treasure Island (FL).

27. Bell, A., D. Templeman, and J.C. Weinlein, *Nonunion of the Femur and Tibia: An Update.* Orthop Clin North Am, 2016. **47**(2): p. 365-75.

28. Giannoudis, P.V., T.A. Einhorn, and D. Marsh, *Fracture healing: the diamond concept.* Injury, 2007. **38 Suppl 4**: p. S3-6.

29. Andrzejowski, P. and P.V. Giannoudis, *The 'diamond concept' for long bone non-union management.* J Orthop Traumatol, 2019. **20**(1): p. 21.

30. Hammer, R.R., S. Hammerby, and B. Lindholm, *Accuracy of radiologic assessment of tibial shaft fracture union in humans.* Clin Orthop Relat Res, 1985(199): p. 233-8.

31. Schlickewei, C.W., et al., *Current and Future Concepts for the Treatment of Impaired Fracture Healing.* Int J Mol Sci, 2019. **20**(22): p. 5805.

32. Rupp, M., et al., *Diaphyseal long bone nonunions - types, aetiology, economics, and treatment recommendations.* Int Orthop, 2018. **42**(2): p. 247-258.

33. Nauth, A., et al., *Principles of Nonunion Management: State of the Art.* J Orthop Trauma, 2018. **32 Suppl 1**(Supplement 3): p. S52-S57.

34. Leighton, R., et al., *Healing of fracture nonunions treated with low-intensity pulsed ultrasound (LIPUS): A systematic review and meta-analysis.* Injury, 2017. **48**(7): p. 1339-1347.

35. Vaughn, J., et al., *Nail Dynamization for Delayed Union and Nonunion in Femur and Tibia Fractures.* Orthopedics, 2016. **39**(6): p. e1117-e1123.

36. Huang, K.C., et al., *Evaluation of methods and timing in nail dynamisation for treating delayed healing femoral shaft fractures.* Injury, 2012. **43**(10): p. 1747-52.

37. Augat, P., et al., *Imaging techniques for the assessment of fracture repair.* Injury, 2014. **45 Suppl 2**: p. S16-22.

38. Axelrad, T.W. and T.A. Einhorn, *Use of clinical assessment tools in the evaluation of fracture healing.* Injury, 2011. **42**(3): p. 301-5.

39. Corrales, L.A., et al., *Variability in the assessment of fracture-healing in orthopaedic trauma studies.* J Bone Joint Surg Am, 2008. **90**(9): p. 1862-8.

40. Blokhuis, T.J., et al., *The reliability of plain radiography in experimental fracture healing.* Skeletal Radiol, 2001. **30**(3): p. 151-6.

41. Whelan, D.B., et al., *Development of the radiographic union score for tibial fractures for the assessment of tibial fracture healing after intramedullary fixation.* J Trauma, 2010. **68**(3): p. 629-32.

42. McClelland, D., et al., *Fracture healing assessment comparing stiffness measurements using radiographs.* Clin Orthop Relat Res, 2007. **457**: p. 214-9.

43. Davis, B.J., et al., *Reliability of radiographs in defining union of internally fixed fractures.* Injury, 2004. **35**(6): p. 557-61.

44. Panjabi, M.M., et al., *Correlations of radiographic analysis of healing fractures with strength: a statistical analysis of experimental osteotomies.* J Orthop Res, 1985. **3**(2): p. 212-8.

45. Nicholls, P.J., et al., *X-ray diagnosis of healing fractures in rabbits.* Clin Orthop Relat Res, 1979(142): p. 234-6.

46. Morgan, E.F., et al., *Micro-computed tomography assessment of fracture healing: relationships among callus structure, composition, and mechanical function.* Bone, 2009. **44**(2): p. 335-44.

47. Morshed, S., et al., *Outcome assessment in clinical trials of fracture-healing.* J Bone Joint Surg Am, 2008. **90 Suppl 1**(Supplement_1): p. 62-7.

48. Mallinson, P.I., et al., *Dual-Energy CT for the Musculoskeletal System.* Radiology, 2016. **281**(3): p. 690-707.

49. Chehade, M.J., et al., *Clinical implications of stiffness and strength changes in fracture healing.* J Bone Joint Surg Br, 1997. **79**(1): p. 9-12.

50. Wade, R.H., C.I. Moorcroft, and P.B. Thomas, *Fracture stiffness as a guide to the management of tibial fractures.* J Bone Joint Surg Br, 2001. **83**(4): p. 533-5.

51. Webb, J., et al., *Manual assessment of fracture stiffness.* Injury, 1996. **27**(5): p. 319-20.

52. Augat, P., et al., *Biomechanical methods for the assessment of fracture repair.* Injury, 2014. **45 Suppl 2**: p. S32-8.

53. Claes, L.E. and J.L. Cunningham, *Monitoring the mechanical properties of healing bone.* Clin Orthop Relat Res, 2009. **467**(8): p. 1964-71.

54. Bible, J.E. and H.R. Mir, *External Fixation: Principles and Applications.* J Am Acad Orthop Surg, 2015. **23**(11): p. 683-90.

55. Lowenberg, D.W., M. Githens, and C. Boone, *Principles of tibial fracture management with circular external fixation.* Orthop Clin North Am, 2014. **45**(2): p. 191-206.

56. Bliven, E.K., et al., *External fixation of the lower extremities: Biomechanical perspective and recent innovations.* Injury, 2019. **50 Suppl 1**: p. S10-S17.

57. Cunningham, J.L., et al., *The measurement of stiffness of fractures treated with external fixation.* Eng Med, 1987. **16**(4): p. 229-32.

58. Wehner, T., et al., *Temporal delimitation of the healing phases via monitoring of fracture callus stiffness in rats.* J Orthop Res, 2014. **32**(12): p. 1589-95.

59. An, K.N., R.A. Kasman, and E.Y. Chao, *Theoretical analysis of fracture healing monitoring with external fixators.* Eng Med, 1988. **17**(1): p. 11-5.

60. Grasa, J., et al., *Monitoring in vivo load transmission through an external fixator.* Ann Biomed Eng, 2010. **38**(3): p. 605-12.

61. Hente, R., J. Cordey, and S.M. Perren, *In vivo measurement of bending stiffness in fracture healing.* Biomed Eng Online, 2003. **2**: p. 8.

62. Richardson, J.B., et al., *Measuring stiffness can define healing of tibial fractures.* J Bone Joint Surg Br, 1994. **76**(3): p. 389-94.

63. Evans, M., J. Kenwright, and J.L. Cunningham, *Design and performance of a fracture monitoring transducer.* J Biomed Eng, 1988. **10**(1): p. 64-9.

64. Seide, K., et al., *Three-dimensional load measurements in an external fixator.* J Biomech, 2004. **37**(9): p. 1361-9.

65. Blazquez-Carmona, P., et al., *Real-Time Wireless Platform for In Vivo Monitoring of Bone Regeneration.* Sensors (Basel), 2020. **20**(16): p. 4591.

66. Schmickal, T., J. von Recum, and A. Wentzensen, *Stiffness measurement of the neocallus with the Fraktometer FM 100.* Arch Orthop Trauma Surg, 2005. **125**(10): p. 653-9.

67. Claes, L., et al., *Monitoring and healing analysis of 100 tibial shaft fractures.* Langenbecks Arch Surg, 2002. **387**(3-4): p. 146-52.

68. Ogrodnik, P.J., C.I. Moorcroft, and P.B. Thomas, *Measuring multi-dimensional, time-dependent mechanical properties of a human tibial fracture using an automated system.* Proc Inst Mech Eng H, 2007. **221**(6): p. 641-52.

69. Seide, K., et al., *Telemetric assessment of bone healing with an instrumented internal fixator: a preliminary study.* J Bone Joint Surg Br, 2012. **94**(3): p. 398-404.

70. Edwards, C.C., et al., *Severe open tibial fractures. Results treating 202 injuries with external fixation.* Clin Orthop Relat Res, 1988(230): p. 98-115.

71. Tejwani, N., D. Polonet, and P.R. Wolinsky, *External fixation of tibial fractures.* J Am Acad Orthop Surg, 2015. **23**(2): p. 126-30.

72. Augat, P. and C. von Ruden, *Evolution of fracture treatment with bone plates.* Injury, 2018. **49 Suppl 1**: p. S2-S7.

73. Taljanovic, M.S., et al., *Fracture fixation.* Radiographics, 2003. **23**(6): p. 1569-90.

74. Rosa, N., et al., *Recent developments on intramedullary nailing: a biomechanical perspective.* Ann N Y Acad Sci, 2017. **1408**(1): p. 20-31.

75. Stoffel, K., K. Klaue, and S.M. Perren, *Functional load of plates in fracture fixation in vivo and its correlate in bone healing.* Injury, 2000. **31 Suppl 2**: p. S-B37-50.

76. Gadomski, B.C., et al., *Partial gravity unloading inhibits bone healing responses in a large animal model.* J Biomech, 2014. **47**(12): p. 2836-42.

77. Burny, F., et al., *Concept, design and fabrication of smart orthopedic implants.* Med Eng Phys, 2000. **22**(7): p. 469-79.

78. Kienast, B., et al., *An electronically instrumented internal fixator for the assessment of bone healing.* Bone Joint Res, 2016. **5**(5): p. 191-7.

79. Schneider, E., et al., *Loads acting in an intramedullary nail during fracture healing in the human femur.* J Biomech, 2001. **34**(7): p. 849-57.

80. Wilson, D.J., et al., *A single-channel telemetric intramedullary nail for in vivo measurement of fracture healing.* J Orthop Trauma, 2009. **23**(10): p. 702-9.

81. Ledet, E.H., et al., *Smart implants in orthopedic surgery, improving patient outcomes: a review.* Innov Entrep Health, 2018. **5**: p. 41-51.

82. Melik, R., et al., *Bio-implantable passive on-chip RF-MEMS strain sensing resonators for orthopaedic applications.* Journal of Micromechanics and Microengineering, 2008. **18**(11).

83. Melik, R., et al., *Nested Metamaterials for Wireless Strain Sensing.* IEEE Journal of Selectd Topics in Quantum Electronics, 2010. **16**(2): p. 450-458.

84. Johnson, C.C. and A.W. Guy, *Nonionizing electromagnetic wave effects in biological materials and systems.* Proceedings of the IEEE, 1972. **60**(6): p. 692-718.

85. Fischer, W.J., et al. *Galfenol resonant sensor for indirect wireless osteosynthesis plate bending measurements*. in *Proc. IEEE Sens. Conf.* 2009. Christchurch, Canterbury, New Zealand: IEEE.

86. Sauer, S., et al., *Passive Wireless Resonant Galfenol Sensor for Osteosynthesis Plate Bending Measurement.* IEEE Sensors Journal, 2012. **12**(5): p. 1226-1233.

87. Melik, R., et al., *Metamaterial-based wireless strain sensors.* Applied Physics Letters, 2009. **95**(1): p. 011106.

88. Oess, N.P., B. Weisse, and B.J. Nelson, *Magnetoelastic Strain Sensor for Optimized Assessment of Bone Fracture Fixation.* IEEE Sensors Journal, 2009. **9**(8): p. 961-968.

89. Tan, Y., et al., *A Passive and Wireless Sensor for Bone Plate Strain Monitoring.* Sensors (Basel), 2017. **17**(11): p. 2635.

90. Wachs, R.A., et al., *Elementary Implantable Force Sensor: For Smart Orthopaedic Implants.* Adv Biosens Bioelectron, 2013. **2**(4).

91. Tan, Y., J. Zhu, and L. Ren, *A Two-Dimensional Wireless and Passive Sensor for Stress Monitoring.* Sensors (Basel), 2019. **19**(1): p. 135.

92. Melik, R., et al., *Circular High-Q Resonating Isotropic Strain Sensors with Large Shift of Resonance Frequency under Stress.* Sensors (Basel), 2009. **9**(12): p. 9444-51.

93. Melik, R., et al., *Metamaterial based telemetric strain sensing in different materials.* Opt Express, 2010. **18**(5): p. 5000-7.

94. Melik, R., et al. *Metamaterial-based wireless RF-MEMS strain sensors*. in *2010 IEEE Sensors*. 2010.

95. Melik, R., et al., *RF-MEMS Load Sensors with Enhanced Q-factor and Sensitivity in a Suspended Architecture.* Microelectron Eng, 2011. **88**(3): p. 247-253.

96. McGilvray, K.C., et al., *Implantable microelectromechanical sensors for diagnostic monitoring and post-surgical prediction of bone fracture healing.* J Orthop Res, 2015. **33**(10): p. 1439-46.

97. Labus, K.M., et al., *A Coaxial Dipole Antenna for Passively Sensing Object Displacement and Deflection for Orthopaedic Applications.* IEEE Access, 2018. **6**: p. 68184-68194.

98. Wolynski, J.G., et al., *Utilizing Multiple BioMEMS Sensors to Monitor Orthopaedic Strain and Predict Bone Fracture Healing.* J Orthop Res, 2019. **37**(9): p. 1873-1880.

99. Claes, L.E., et al., *Effects of mechanical factors on the fracture healing process.* Clin Orthop Relat Res, 1998(355 Suppl): p. S132-47.

100. Claes, L.E., et al., *Effect of dynamization on gap healing of diaphyseal fractures under external fixation.* Clin Biomech (Bristol, Avon), 1995. **10**(5): p. 227-234.

101. Jackson, R.W. and I. Macnab, *Fractures of the shaft of the tibia; a clinical and experimental study.* Am J Surg, 1959. **97**(5): p. 543-57.

102. Nicoll, E.A., *Fractures of the Tibial Shaft. A Survey of 705 Cases.* J Bone Joint Surg Br, 1964. **46**: p. 373-87.

103. Weissman, S.L., H.Z. Herold, and M. Engelberg, *Fractures of the middle two-thirds of the tibial shaft.* J Bone Joint Surg Am, 1966. **48**(2): p. 257-67.

104. Dickson, K., et al., *Delayed unions and nonunions of open tibial fractures. Correlation with arteriography results.* Clin Orthop Relat Res, 1994(302): p. 189-93.

105. Goodship, A.E. and J. Kenwright, *The influence of induced micromovement upon the healing of experimental tibial fractures.* J Bone Joint Surg Br, 1985. **67**(4): p. 650-5.

106. Miclau, T., et al., *Effects of delayed stabilization on fracture healing.* J Orthop Res, 2007. **25**(12): p. 1552-8.

107. Uhthoff, H.K., P. Poitras, and D.S. Backman, *Internal plate fixation of fractures: short history and recent developments.* J Orthop Sci, 2006. **11**(2): p. 118-26.

108. Garcia, P., et al., *Development of a reliable non-union model in mice.* J Surg Res, 2008. **147**(1): p. 84-91.

109. Whelan, D.B., et al., *Interobserver and intraobserver variation in the assessment of the healing of tibial fractures after intramedullary fixation.* J Bone Joint Surg Br, 2002. **84**(1): p. 15-8.

110. Young, J.W., et al., *Sonographic evaluation of bone production at the distraction site in Ilizarov limb-lengthening procedures.* AJR Am J Roentgenol, 1990. **154**(1): p. 125-8.

111. Melik, R., et al., *Flexible metamaterials for wireless strain sensing.* Applied Physics Letters, 2009. **95**(18): p. 181105.

112. Hak, D.J., R. Neiman, and S. Hazelwood, *Biomechanical strain analysis of the proximal femur following retrograde intramedullary nailing.* Curr Orthop Pract, 2010. **21**(4): p. 385-389.

113. Montanini, R. and V. Filardi, *In vitro biomechanical evaluation of antegrade femoral nailing at early and late postoperative stages.* Med Eng Phys, 2010. **32**(8): p. 889-97.

114. Firoozabadi, R., et al., *Does plugging unused combination screw holes improve the fatigue life of fixation with locking plates in comminuted supracondylar fractures of the femur?* J Bone Joint Surg Br, 2012. **94**(2): p. 241-8.

115. Kregor, P.J., et al., *Treatment of distal femur fractures using the less invasive stabilization system: surgical experience and early clinical results in 103 fractures.* J Orthop Trauma, 2004. **18**(8): p. 509-20.

116. Vallier, H.A., et al., *Failure of LCP condylar plate fixation in the distal part of the femur. A report of six cases.* J Bone Joint Surg Am, 2006. **88**(4): p. 846-53.

117. Henderson, C.E., et al., *Locking plates for distal femur fractures: is there a problem with fracture healing?* J Orthop Trauma, 2011. **25 Suppl 1**: p. S8-14.

118. Lujan, T.J., et al., *A computational technique to measure fracture callus in radiographs.* J Biomech, 2010. **43**(4): p. 792-5.

119. Pearce, A.I., et al., *Animal models for implant biomaterial research in bone: a review.* Eur Cell Mater, 2007. **13**: p. 1-10.

120. Martini, L., et al., *Sheep model in orthopedic research: a literature review.* Comp Med, 2001. **51**(4): p. 292-9.

121. Geetha, M., et al., *Ti based biomaterials, the ultimate choice for orthopaedic implants – A review.* Progress in Materials Science, 2009. **54**(3): p. 397-425.

122. Heyland, M., et al., *[Steel or titanium for osteosynthesis : A mechanobiological perspective].* Unfallchirurg, 2017. **120**(2): p. 103-109.

123. Wolynski, J.G., et al., *Diagnostic prediction of ovine fracture healing outcomes via a novel multi-location direct electromagnetic coupling antenna.* Ann Transl Med, 2021. **9**(15): p. 1223.

124. Zhang, L., et al., *The role of impairment of mesenchymal stem cell function in osteoporotic bone fracture healing.* Australas Phys Eng Sci Med, 2017. **40**(3): p. 603-610.

125. Ghimire, S., et al., *Role of Dynamic Loading on Early Stage of Bone Fracture Healing.* Ann Biomed Eng, 2018. **46**(11): p. 1768-1784.

126. Ghiasi, M.S., et al., *Computational modeling of human bone fracture healing affected by different conditions of initial healing stage.* BMC Musculoskelet Disord, 2019. **20**(1): p. 562.

127. Zhang, L., M. Richardson, and P. Mendis, *Role of chemical and mechanical stimuli in mediating bone fracture healing.* Clin Exp Pharmacol Physiol, 2012. **39**(8): p. 706-10.

128. Gaston, M.S. and A.H. Simpson, *Inhibition of fracture healing.* J Bone Joint Surg Br, 2007. **89**(12): p. 1553-60.

129. Labus, K.M., et al., *Direct electromagnetic coupling for non-invasive measurements of stability in simulated fracture healing.* J Orthop Res, 2019. **37**(5): p. 1164-1171.

130. Claes, L., K. Eckert-Hubner, and P. Augat, *The fracture gap size influences the local vascularization and tissue differentiation in callus healing.* Langenbecks Arch Surg, 2003. **388**(5): p. 316-22.

131. Augat, P., et al., *Local tissue properties in bone healing: influence of size and stability of the osteotomy gap.* J Orthop Res, 1998. **16**(4): p. 475-81.

132. Lienau, J., et al., *Initial vascularization and tissue differentiation are influenced by fixation stability.* J Orthop Res, 2005. **23**(3): p. 639-45.

133. Joslin, C.C., et al., *Weight bearing after tibial fracture as a guide to healing.* Clin Biomech (Bristol, Avon), 2008. **23**(3): p. 329-33.

134. Yngvesson, K.S., et al., *The tapered slot antenna-a new integrated element for millimeter-wave applications.* IEEE Transactions on Microwave Theory and Techniques, 1989. **37**(2): p. 365-374.

135. Wu, J., et al., *A Printed UWB Vivaldi Antenna Using Stepped Connection Structure Between Slotline and Tapered Patches.* IEEE Antennas and Wireless Propagation Letters, 2014. **13**: p. 698-701.

136. Entesari, K., R. Ebrahimi Ghiri, and E. Kaya, *Broadband dielectric spectroscopy*, in *IEEE Microwave Magazine*. 2021. p. 26-48.

137. *Modern Antenna Handbook*. 2008, Hoboken, NJ: John Wiley & Sons, Inc.

138. Jagodzinski, M. and C. Krettek, *Effect of mechanical stability on fracture healing--an update.* Injury, 2007. **38 Suppl 1**(1): p. S3-10.

139. Mills, L., et al., *The multifactorial aetiology of fracture nonunion and the importance of searching for latent infection.* Bone Joint Res, 2016. **5**(10): p. 512-519.

140. Santolini, E., R. West, and P.V. Giannoudis, *Risk factors for long bone fracture non-union: a stratification approach based on the level of the existing scientific evidence.* Injury, 2015. **46 Suppl 8**: p. S8-S19.

141. Dwyer, J.S., et al., *Stiffness measurements to assess healing during leg lengthening. A preliminary report.* J Bone Joint Surg Br, 1996. **78**(2): p. 286-9.

142. Steiner, M., et al., *Numerical simulation of callus healing for optimization of fracture fixation stiffness.* PLoS One, 2014. **9**(7): p. e101370.

143. Ganesh, V.K., K. Ramakrishna, and D.N. Ghista, *Biomechanics of bone-fracture fixation by stiffness-graded plates in comparison with stainless-steel plates.* Biomed Eng Online, 2005. **4**(1): p. 46.

144. Gomez-Benito, M.J., et al., *A 3D computational simulation of fracture callus formation: influence of the stiffness of the external fixator.* J Biomech Eng, 2006. **128**(3): p. 290-9.

145. Wee, H., et al., *Finite Element-Derived Surrogate Models of Locked Plate Fracture Fixation Biomechanics.* Ann Biomed Eng, 2017. **45**(3): p. 668-680.

146. Cao, Y., et al., *The impact of plate length, fibula integrity and plate placement on tibial shaft fixation stability: a finite element study.* J Orthop Surg Res, 2019. **14**(1): p. 52.

147. Favre, P., et al., *Superior versus anteroinferior plating of the clavicle: a finite element study.* J Orthop Trauma, 2011. **25**(11): p. 661-5.

148. Stoffel, K., et al., *Biomechanical testing of the LCP--how can stability in locked internal fixators be controlled?* Injury, 2003. **34 Suppl 2**: p. B11-9.

149. Zhao, X., et al., *Investigation of load transfer process between external fixator and bone model by experimental and finite element methods.* J Appl Biomater Funct Mater, 2019. **17**(1): p. 2280800019826512.

150. Li, J., et al., *A theoretical analysis and finite element simulation of fixator-bone system stiffness on healing progression.* J Appl Biomater Funct Mater, 2018. **16**(3): p. 115-125.

151. Li, J., et al., *A finite element analysis for monitoring the healing progression of fixator-bone system under three loading conditions.* Biomed Mater Eng, 2018. **29**(4): p. 473-483.

152. Zhang, Y.K., et al., *Biomechanical effect of the configuration of screw hole style on locking plate fixation in proximal humerus fracture with a simulated gap: A finite element analysis.* Injury, 2016. **47**(6): p. 1191-5.

153. Gomez-Benito, M.J., et al., *Influence of fracture gap size on the pattern of long bone healing: a computational study.* J Theor Biol, 2005. **235**(1): p. 105-19.

154. Miramini, S., et al., *Influence of fracture geometry on bone healing under locking plate fixations: A comparison between oblique and transverse tibial fractures.* Med Eng Phys, 2016. **38**(10): p. 1100-8.

155. Oh, J.K., et al., *Effect of fracture gap on stability of compression plate fixation: a finite element study.* J Orthop Res, 2010. **28**(4): p. 462-7.

156. Lacroix, D. and P.J. Prendergast, *A mechano-regulation model for tissue differentiation during fracture healing: analysis of gap size and loading.* J Biomech, 2002. **35**(9): p. 1163-71.

157. Andreykiv, A., F. van Keulen, and P.J. Prendergast, *Simulation of fracture healing incorporating mechanoregulation of tissue differentiation and dispersal/proliferation of cells.* Biomech Model Mechanobiol, 2008. **7**(6): p. 443-61.

158. Garcia-Aznar, J.M., et al., *Computational simulation of fracture healing: influence of interfragmentary movement on the callus growth.* J Biomech, 2007. **40**(7): p. 1467-76.

159. Lipphaus, A. and U. Witzel, *Finite-Element Syntheses of Callus and Bone Remodeling: Biomechanical Study of Fracture Healing in Long Bones.* Anat Rec (Hoboken), 2018. **301**(12): p. 2112-2121.

160. Steiner, M., et al., *Disadvantages of interfragmentary shear on fracture healing--mechanical insights through numerical simulation.* J Orthop Res, 2014. **32**(7): p. 865-72.

161. Wehner, T., et al., *Prediction of the time course of callus stiffness as a function of mechanical parameters in experimental rat fracture healing studies--a numerical study.* PLoS One, 2014. **9**(12): p. e115695.

162. Yushkevich, P.A., et al., *User-guided 3D active contour segmentation of anatomical structures: significantly improved efficiency and reliability.* Neuroimage, 2006. **31**(3): p. 1116-28.

163. Reilly, D.T. and A.H. Burstein, *The elastic and ultimate properties of compact bone tissue.* J Biomech, 1975. **8**(6): p. 393-405.

164. de Alcantara, A.C.S., et al., *Patient-Specific Bone Multiscale Modelling, Fracture Simulation and Risk Analysis-A Survey.* Materials (Basel), 2019. **13**(1): p. 106.

165. Kim, H.-J., S.-H. Chang, and H.-J. Jung, *The simulation of tissue differentiation at a fracture gap using a mechano-regulation theory dealing with deviatoric strains in the presence of a composite bone plate.* Composites Part B: Engineering, 2012. **43**(3): p. 978-987.

166. Gadomski, B.C., et al., *Computational characterization of fracture healing under reduced gravity loading conditions.* J Orthop Res, 2016. **34**(7): p. 1206-15.

167. Haidukewych, G.J., *Innovations in locking plate technology.* J Am Acad Orthop Surg, 2004. **12**(4): p. 205-12.

APPENDIX A: FSBIOMEMS SUPPLEMENTARY FIGURES

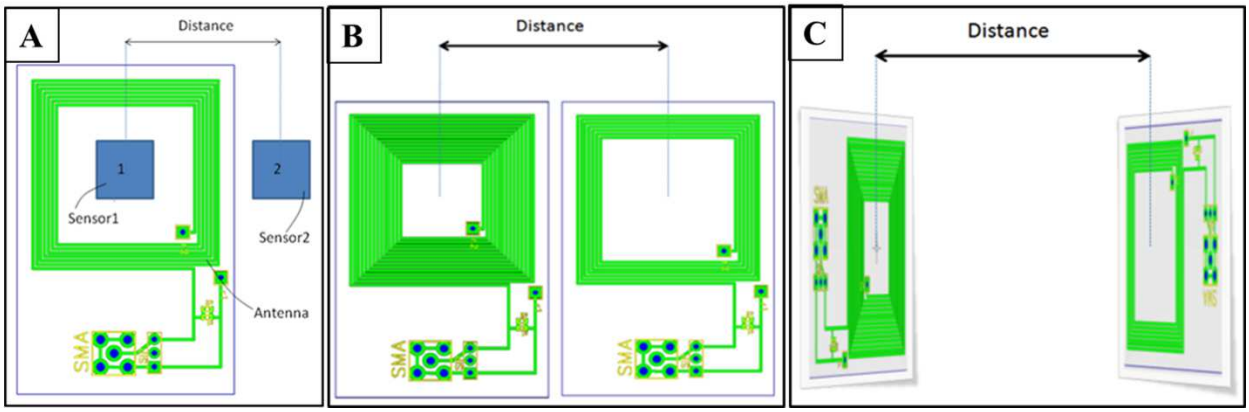

Figure A.1: Schematic of experimental setups for: (A) sensor based cross-talk (B) in-plane antenna based cross-talk (C) axially aligned antenna based cross-talk.

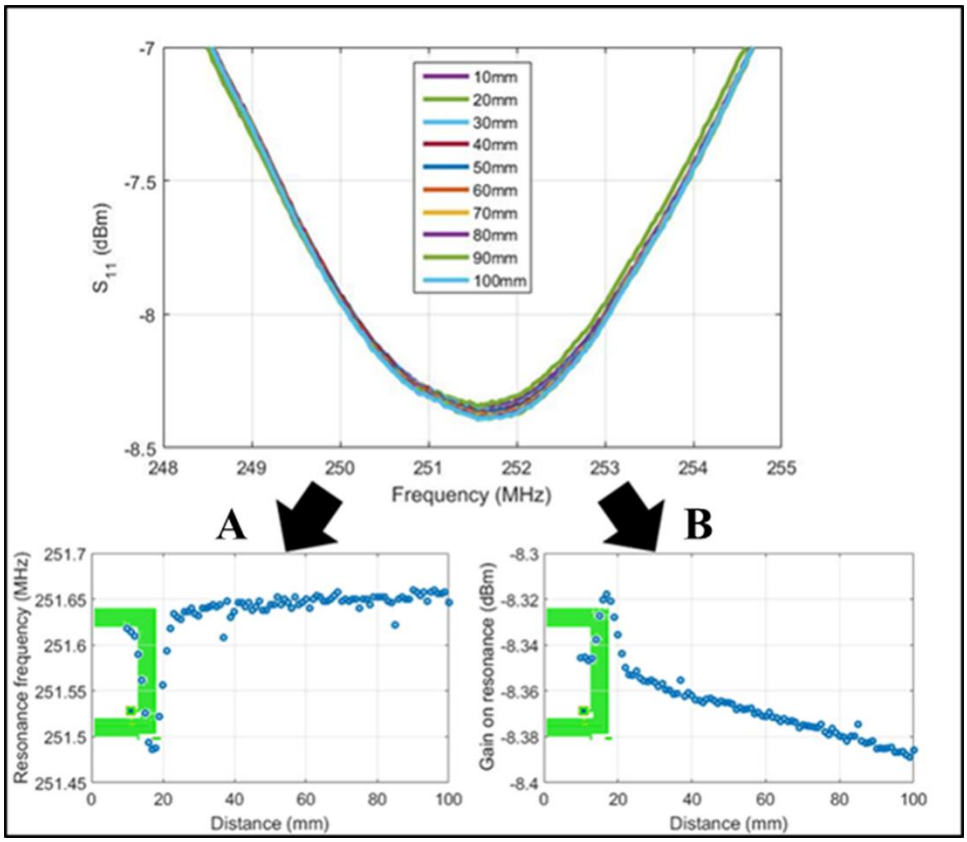

Figure A.2: S11 spectra (A) and gain (B) for sensor induced cross talk of a prototype antenna design (v2_f3).

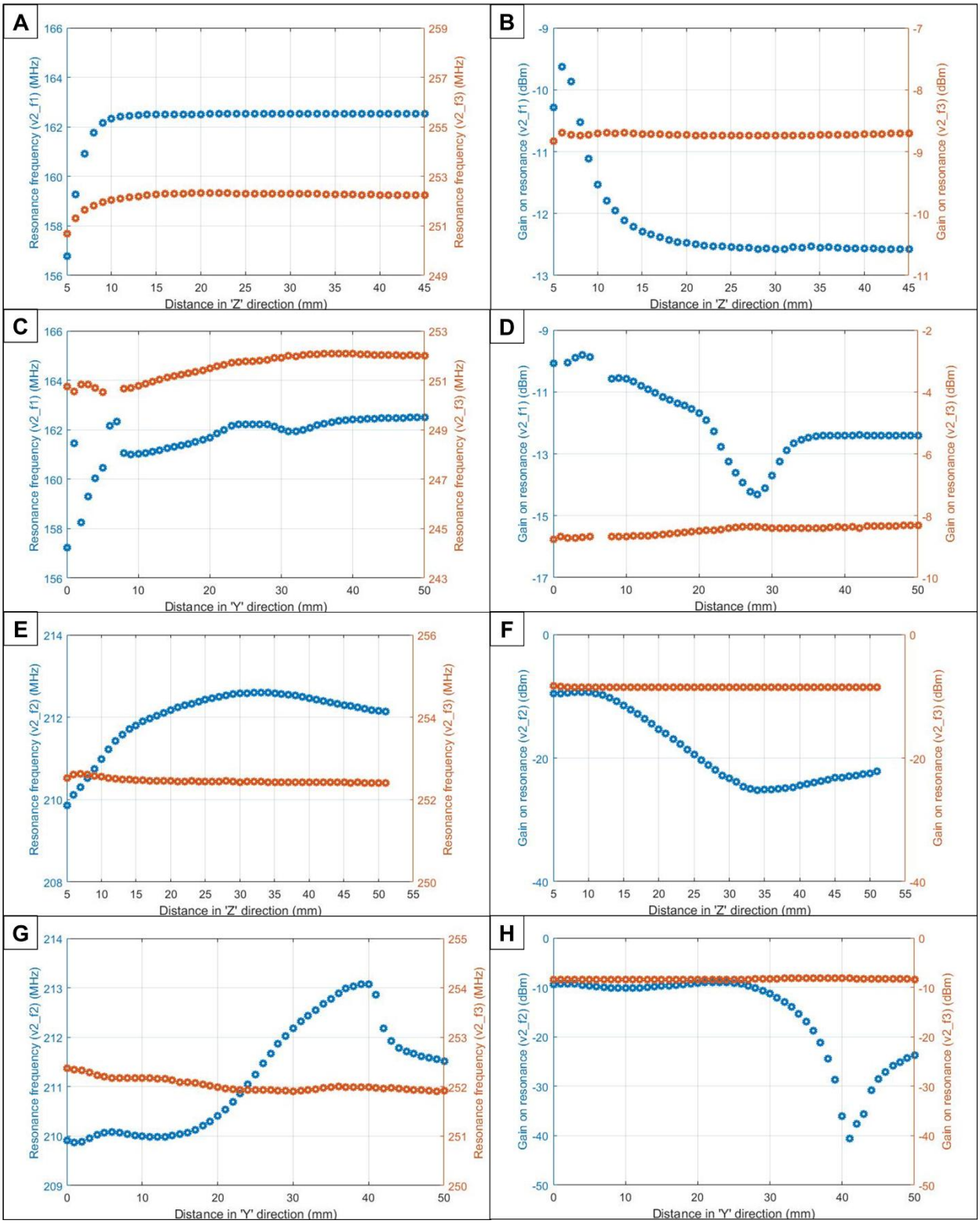

Figure A.3: S11 associated with cross-talk between the v2_f1 and v2_f3 antennae in the Z (A, B) and Y (C, D) directions and between the v2_f2 and v2_f3antennae in the Z (E, F) and Y (G, H) directions.

APPENDIX B: VIVALDI ANTENNA CROSS-TALK

B.1 Introduction

The development of novel Vivaldi antennas for use as DEC diagnostic sensors is detailed in Chapter 5. The contents of Chapter 5 established the efficacy of the miniaturized Vivaldi antenna design, but did not explore the simultaneous use of multiple antennas for characterizing implant deflections in complex fracture types, and for mitigation of limb rigid body displacements. Additional discussion of the motivation and advantages of multi-location measurements are omitted here for brevity, but are discussed at length in Chapters 3.1.1 & 4.4.

For a multi-location DEC system, a primary interest was the ability of multiple antennas to measure implant deflections at their respective measurement sites, without being influenced by the configuration and signals of the other antennas (i.e., antenna cross-talk). An ideal multi-antenna system would feature zero antenna cross-talk, as characterized by the ability to quantify plate displacements via DEC measurements at a single antenna/location, while eliciting zero response from a second antenna at a secondary adjacent measurement location. When antenna cross-talk is non-zero, antennas no longer perform independently and may consequently predict false / inaccurate implant deflections, thus reducing the diagnostic reliability of the system. The purpose of this supplementary content is to characterize antenna cross-talk while performing multi-location DEC measurements via two miniaturized Vivaldi antenna, similar to the analysis performed for a coiled coaxial DEC antenna design in Chapter 4.2.3.

B.2 Materials & Methods

Antenna sensitivity to metallic plate deflections was determined by incrementally increasing, via linear actuator, the distance between a miniaturized Vivaldi antenna and a stainless steel plate segment. Experimental setup emulated that of Chapter 5.2.4; however, a duplicate antenna and linear-actuator positioned plate segment were implemented (i.e., two identical antennas and two plate segments individually positioned by separate precision linear actuators).

The two linear actuators were positioned such that the plate segments were aligned along their length, similar to the methods depicted in Figure 4.2A. Each antenna was aligned with the center of their respective plate segments (i.e., antenna positions also aligned along the length of the plates, and antenna measurement directions were aligned with the actuator displacement directions). The stationary position of one plate segment was maintained while the other segment was displaced (0 – 10 mm, 0.10 mm increments, $n \approx 5$ data points collected at each position) while change in resonant frequency (resonant frequency shift) for each antenna was measured using a two port VNA following the methods of Chapter 5.2.4.

Tests were repeated with parametric variation to the distance between the stationary plate and its respective antenna (0 – 10 mm, 2 mm increment per test), which antenna-plate segment maintained a constant distance (a.k.a. “stationary antenna”), orientation of the antennas relative to the plate segments (parallel or perpendicular, Figure 5.4A or Figure 5.4B, respectively), and distance between the antenna segments (1, 3, or 5 cm between antenna centerlines; 1 cm permutation was not tested for parallel orientation as antennas would be in direct contact).

B.3 Results

Resonant frequency shifts, as grouped by antenna positioning and stationary antenna, are presented in Figure B.1, where each color corresponds to a different stationary antenna-plate distance. For all testing parameters, the resonant frequency shifts were greater when antennas were positioned parallel, rather than perpendicular, to the plate segments (Figure B.1). The maximum resonant frequency shift of the stationary antenna were normalized and reported as a percentage of the maximum resonant frequency shift of the non-stationary antenna for the same testing parameters (Figure B.2).

B.4 Discussion

Data from Figure B.1 support the findings of Chapter 5, based on antenna sensitivity to metallic deflections decreasing nonlinearly with increasing antenna-plate distance, and antenna sensitivities being greatest when implants cover the greatest portion of the antenna's measurement side (i.e., parallel antenna-plate orientation). While these findings imply that the parallel antenna orientation is optimal for diagnostic measurements (i.e., for maximum antenna sensitivity), the results of the present experiments suggest that this antenna alignment is suboptimal for multi-antenna setups.

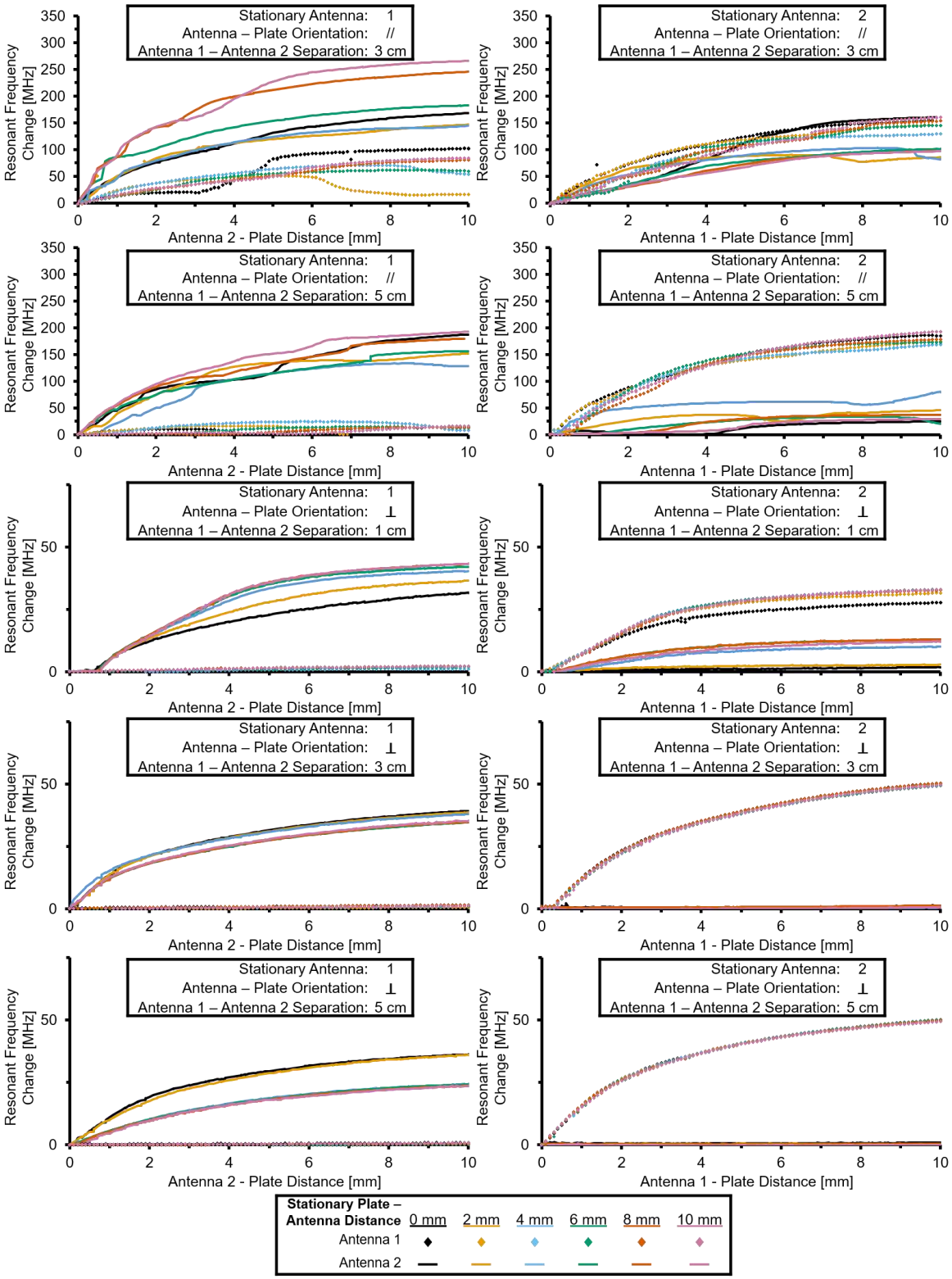

Figure B.1: DEC antenna cross-talk during simultaneous use of two miniaturized Vivaldi antennas. Each plot represents a single experimental permutation of which antenna-plate segment was increased, antenna orientation relative to plate segment (parallel [//] or perpendicular [⊥]), and spacing between each antenna (measured between antenna centerlines).

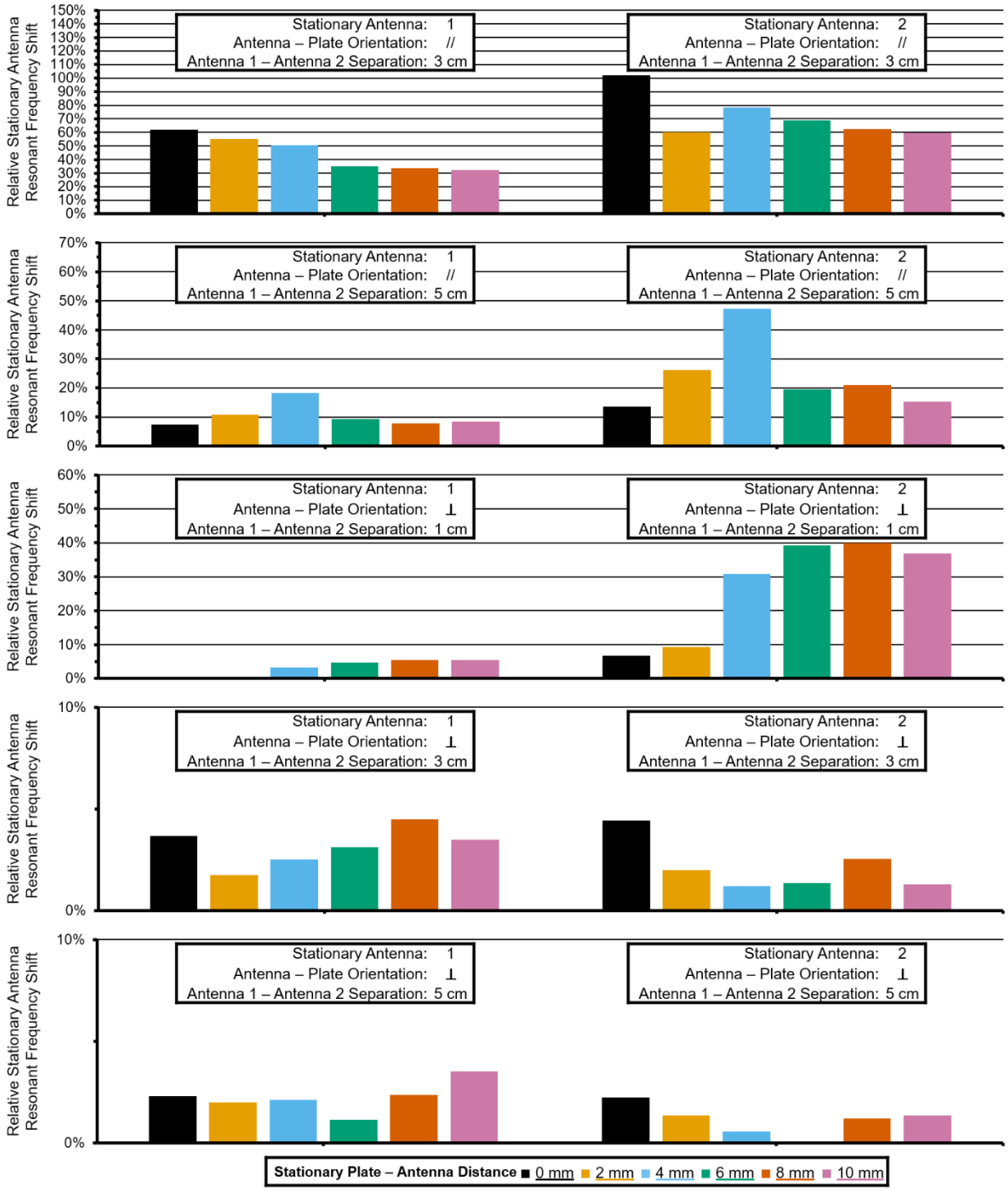

Figure B.2: Maximum resonant frequency shift of the stationary antenna relative to the maximum shift of the non-stationary antenna (reported as a percentage), where shifts are depicted in Figure B.1. Each plot represents a single experimental permutation of which antenna-plate segment was increased, antenna orientation relative to plate segment (parallel [//] or perpendicular [⊥]), and spacing between each antenna (measured between antenna centerlines).

With both antennas aligned parallel to the plate segment, the minimum feasible distance between measurement regions was 3 cm, as any distance less than this value results in direct contact of the two antennas. Despite the stationary antenna being characterized by a constant antenna-plate distance, a large resonant frequency shift was produced in both antennas by displacing the opposite plate segment, thus indicating antenna cross-talk. At 3 cm antenna separation, the stationary antenna exhibited resonant frequency shifts ranging from 32.5% to 102.1% of the shifts observed from the non-stationary antenna (Figure B.2, first row). Antenna cross-talk was reduced by increasing the antenna separation to 5 cm, where the stationary antenna exhibited resonant frequency shifts ranging from 7.4% to 47.3% of the shifts observed from the non-stationary antenna (Figure B.2, second row). Despite this improvement, the cross-talk at both of these distances precludes confident multi-location DEC measurements using this parallel antenna orientation.

Both antenna sensitivity (Figure B.1) and antenna cross-talk (Figure B.2) were reduced in the perpendicular antenna orientation, relative to the parallel orientation. Antenna cross-talk tended to reduce with increased antenna spacing, where maximum stationary antenna resonant frequency shift, as a percentage of the non-stationary antenna shifts, ranged from 0.3% - 39.9%, 1.2% - 4.5%, and 0.1% - 3.5% for antenna spacing of 1-, 3-, and 5-cm; respectively (Figure B.2).

Owing to the limited length of long bones utilized in the translational fracture models throughout this body of work, multi-location DEC measurements in which antenna spacing exceeds 5 cm are not feasible. The data of this chapter therefore suggest that multi-location miniaturized Vivaldi

DEC devices must implement antennas positioned perpendicular to the implant of interest (i.e., the largest face of the planar Vivaldi antennas are parallel rather than coplanar). In this testing setup, minimal antenna cross-talk can be achieved for antenna spacing as small as 1 cm, so long as the initial antenna-implant distance is sufficiently small. Minimization of antenna cross-talk (< 5%, Figure B.2) is achieved by increasing antenna spacing to distances of 3 cm or greater. These distances are sufficiently small for utility in multi-location DEC measurements in both ovine and human long bone fractures. We accordingly conclude that the miniaturized Vivaldi antenna design is feasible for continued development for use in a multi-location DEC device so long as the perpendicular antenna orientation and antenna spacing of $\geq$ 3 cm are implemented.

APPENDIX C: NUMERICAL DISPLACEMENT PREDICTION MODEL DERIVATION

The contents of this supplementary chapter detail the derivation of an Euler-Bernoulli Beam Theory based numerical model for predicting implant displacements during mechanical four-point bending of the fractured bone (i.e., a mechanical configuration comparable to the DEC loading device and FE model used throughout this body of work). The numerical model developed in this chapter is subsequently used for parametric analyses in Appendix D, which serves as partial validation of the FE model in Chapter 6.

To calculate the deflection of the orthopaedic implant-bone-callus composite during four-point bending, the composite was broken into sections with different bending rigidities according to the presence of the orthopaedic plate or fracture callus (Figure C.1).

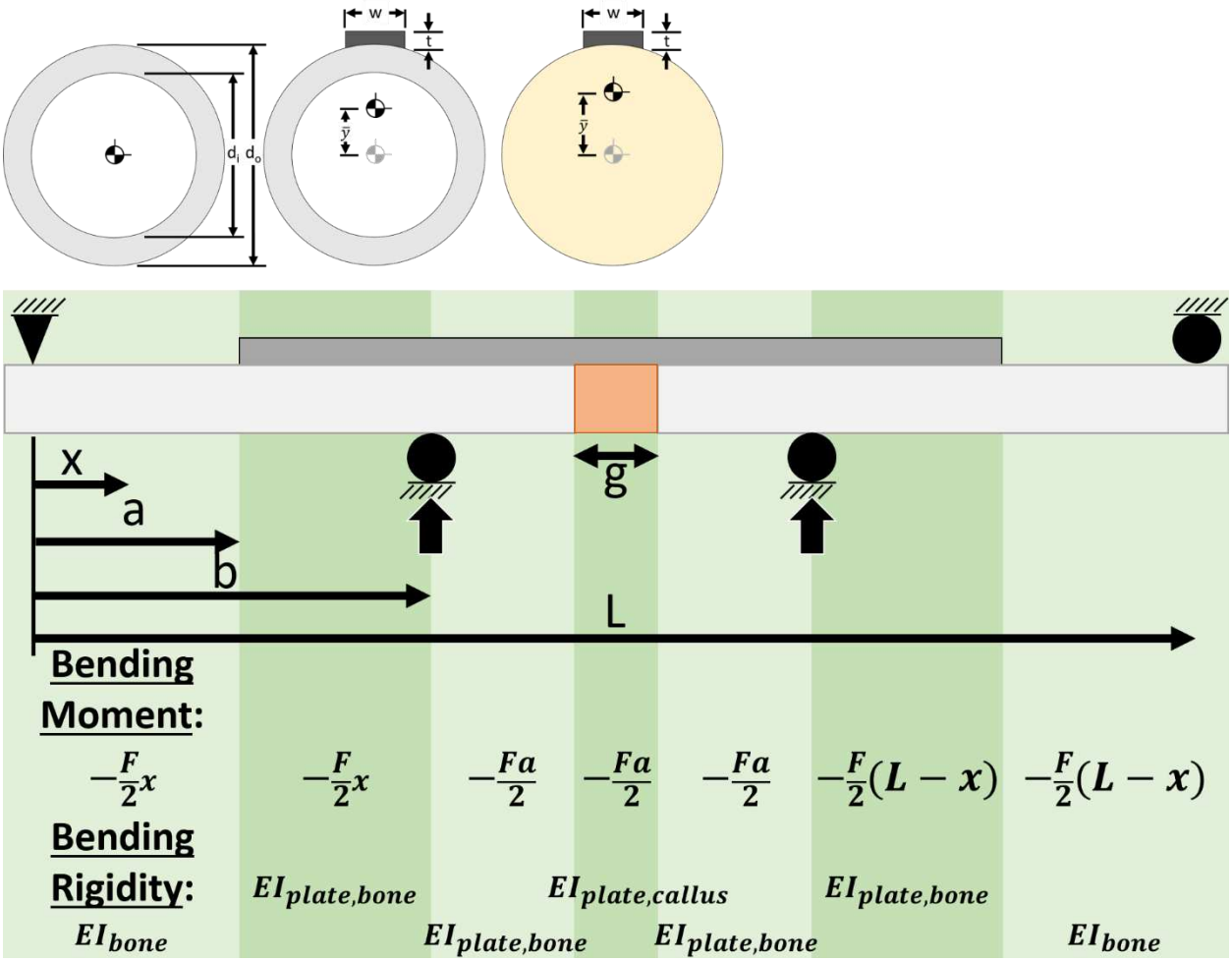

Figure C.1: Geometry used for numerical prediction bone-implant deflections during four-point bending. Bone and plate geometries were simplified to be hollow cylinders and rectangular plates, respectively, with uniform cross-sections. Models with intramedullary nail implant fixation assumed the nail to have a uniform circular cross-section, with the neutral axes of the bone and nail sections being collinear. Implant-bone interface was treated as perfectly bonded so that bending moment and bending rigidity discretely varied along the bending axis.

The bending rigidity of the hardware-free section of cortical bone is obtained assuming a hollow cylindrical cross-section:

$$(EI)_{bone} = \frac{\pi E_{bone}}{64}\left(d_o^4 - d_i^4\right) \qquad (C.1)$$

Differences in the elastic moduli of the bone and plate can be accounted for through transformation of area to adjust the effective width of the orthopaedic plate, then both sections can be treated as having the elastic modulus of bone. The presence of the orthopaedic plate shifts the centroid from the axis of the bone towards the plate by a distance defined by:

$$\bar{y}_{plate,bone} = \frac{E_{plate} wt\left(d_o + t\right)}{2E_{plate} wt + \frac{\pi}{2} E_{bone}\left(d_o^4 - d_i^4\right)} \qquad (C.2)$$

The bending rigidity of the bone-plate composite section is found by applying parallel axis theorem to each section relative to the new centroid location, yielding:

$$\left(EI\right)_{plate,bone} = E_{bone}\left\{\frac{\frac{E_{plate}}{E_{bone}} wt^3}{12} + \frac{E_{plate}}{E_{bone}} wt\left[\frac{d_o + t}{2} - \bar{y}_{plate,bone}\right]^2 + \frac{\pi}{64}\left(d_o^4 - d_i^4\right) + \frac{\pi}{4}\left(d_o^2 - d_i^2\right)\bar{y}_{plate,bone}^{\,2}\right\} \qquad (C.3)$$

Applying similar calculations to the plate-callus cross-section, with the assumption of a solid cylindrical callus cross-section, yields:

$$\bar{y}_{plate,callus} = \frac{E_{plate} wt\left(d_o + t\right)}{2E_{plate} wt + \frac{\pi}{2} E_{callus} d_o^4} \qquad (C.4)$$

$$\left(EI\right)_{plate,callus} = E_{callus}\left[\frac{\frac{E_{plate}}{E_{callus}} wt^3}{12} + \frac{E_{plate}}{E_{callus}} wt\left(\frac{d_o + t}{2} - \bar{y}_{plate,callus}\right)^2 + \frac{\pi}{64} d_o^4 + \frac{\pi}{4}\left(d_o \bar{y}_{plate,callus}\right)^2\right] \qquad (C.5)$$

With the stepwise bending rigidities calculated, the deflection of the orthopaedic plate can be predicted using Euler-Bernoulli Beam Theory:

$$\frac{\partial^2}{\partial x^2}\left(EI\frac{\partial^2 w}{\partial x^2}\right)=q(x) \tag{C.6}$$

$$\frac{\partial}{\partial x}\left(EI\frac{\partial^2 w}{\partial x^2}\right)=V(x) \tag{C.7}$$

$$EI\frac{\partial^2 w}{\partial x^2}=M(x) \tag{C.8}$$

$$\frac{\partial w}{\partial x}(x)=\int_0^x\frac{M}{EI}dx \tag{C.9}$$

$$\delta(x)=\int_0^x\int_0^x\frac{M}{EI}dxdx \tag{C.10}$$

$$\delta_{\max}=\delta\left(x=\frac{L}{2}\right)=\int_0^{L/2}\int_0^{L/2}\frac{M}{EI}dxdx \tag{C.11}$$

Accounting for discrete changes to the bending rigidity and moment as a function of x:

$$\frac{\partial w}{\partial x}(0<x<a)=\int\frac{-Fx}{2(EI)_{bone}}dx=\frac{-Fx^2}{4(EI)_{bone}}+C_1 \tag{C.12}$$

$$\delta(0<x<a)=\int\left[\frac{-Fx^2}{4(EI)_{bone}}+C_1\right]dx=\frac{-Fx^3}{12(EI)_{bone}}+C_1x+C_2 \tag{C.13}$$

$$\frac{\partial w}{\partial x}(a<x<b)=\int\frac{-Fx}{2(EI)_{plate,bone}}dx=\frac{-Fx^2}{4(EI)_{plate,bone}}+D_1 \tag{C.14}$$

$$\delta(a<x<b)=\int\left[\frac{-Fx^2}{4(EI)_{plate,bone}}+D_1\right]dx=\frac{-Fx^3}{12(EI)_{plate,bone}}+D_1x+D_2 \tag{C.15}$$

$$\frac{\partial w}{\partial x}\left(b < x < \frac{L-g}{2}\right) = \int \frac{-Fb}{2(EI)_{plate,bone}}dx = \frac{-Fbx}{2(EI)_{plate,bone}} + G_1 \qquad (C.16)$$

$$\delta\left(b < x < \frac{L-g}{2}\right) = \int\left[\frac{-Fbx}{2(EI)_{plate,bone}} + G_1\right]dx = \frac{-Fbx^2}{4(EI)_{plate,bone}} + G_1x + G_2 \qquad (C.17)$$

$$\frac{\partial w}{\partial x}\left(\frac{L-g}{2} < x < \frac{L}{2}\right) = \int \frac{-Fb}{2(EI)_{plate,callus}}dx = \frac{-Fbx}{2(EI)_{plate,callus}} + H_1 \qquad (C.18)$$

$$\delta\left(\frac{L-g}{2} < x < \frac{L}{2}\right) = \int\left[\frac{-Fbx}{2(EI)_{plate,callus}} + H_1\right]dx = \frac{-Fbx^2}{4(EI)_{plate,callus}} + H_1x + H_2 \qquad (C.19)$$

Applying boundary conditions:

Boundary Condition: zero displacement at stationary pin (x = 0).

$$\delta(x=0) = 0$$

$$\frac{-F(0)^3}{12(EI)_{bone}} + C_1(0) + C_2 = 0 \qquad (C.20)$$

Boundary Condition: Continuous slope at plate boundary (x = a).

$$\frac{\partial w}{\partial x}(x \to a) = \frac{\partial w}{\partial x}(a \leftarrow x)$$

$$\frac{-Fa^2}{4(EI)_{bone}} + C_1 = \frac{-Fa^2}{4(EI)_{plate,bone}} + D_1 \qquad (C.21)$$

Boundary Condition: Continuous displacement at plate boundary (x = a).

$$\delta(x \to a) = \delta(a \leftarrow x)$$

$$\frac{-F(a)^3}{12(EI)_{bone}} + C_1a + C_2 = \frac{-F(a)^3}{12(EI)_{plate,bone}} + D_1a + D_2 \qquad (C.22)$$

Boundary Condition: Continuous slope at load application roller (x = b).

$$\frac{\partial w}{\partial x}(x \to b) = \frac{\partial w}{\partial x}(b \leftarrow x)$$

$$\frac{-Fb^2}{4(EI)_{plate,bone}} + D_1 = \frac{-Fb^2}{2(EI)_{plate,bone}} + G_1 \qquad (C.23)$$

Boundary Condition: Continuous displacement at load application roller (x = b).

$$\delta(x \to b) = \delta(b \leftarrow x)$$

$$\frac{-F(b)^3}{12(EI)_{plate,bone}} + D_1 b + D_2 = \frac{-F(b)^3}{4(EI)_{plate,bone}} + G_1 b + G_2 \qquad (C.24)$$

Boundary Condition: Continuous slope at callus boundary $\left(x = \frac{L-g}{2}\right)$.

$$\frac{\partial w}{\partial x}\left(x \to \frac{L-g}{2}\right) = \frac{\partial w}{\partial x}\left(\frac{L-g}{2} \leftarrow x\right)$$

$$\frac{-Fb\left(\frac{L-g}{2}\right)}{2(EI)_{plate,bone}} + G_1 = \frac{-Fb\left(\frac{L-g}{2}\right)}{2(EI)_{plate,callus}} + H_1 \qquad (C.25)$$

Boundary Condition: Continuous displacement at callus boundary $\left(x = \frac{L-g}{2}\right)$.

$$\delta\left(x \to \frac{L-g}{2}\right) = \delta\left(\frac{L-g}{2} \leftarrow x\right)$$

$$\frac{-Fb\left(\frac{L-g}{2}\right)^2}{4(EI)_{plate,bone}} + G_1\left(\frac{L-g}{2}\right) + G_2 = \frac{-Fb\left(\frac{L-g}{2}\right)^2}{4(EI)_{plate,callus}} + H_1\left(\frac{L-g}{2}\right) + H_2 \qquad (C.26)$$

Boundary Condition: Symmetry at plate midspan

$$\frac{\partial w}{\partial x}\left(x = \frac{L}{2}\right) = 0$$

$$\frac{-Fb\left(\frac{L}{2}\right)}{2(EI)_{plate,callus}} + H_1 = 0 \qquad (C.27)$$

Simultaneously solving the system of equations (Equations C.20 – C.27) determines the constants of integration, which can then be used to solve the displacement field over the length of the bone-plate composite, including the maximum plate midspan deflection using Equation C.19.

$$\begin{bmatrix} 0 & 1 & 0 & 0 & 0 & 0 & 0 & 0 \\ 1 & 0 & -1 & 0 & 0 & 0 & 0 & 0 \\ a & 1 & -a & -1 & 0 & 0 & 0 & 0 \\ 0 & 0 & 1 & 0 & -1 & 0 & 0 & 0 \\ 0 & 0 & b & 1 & -b & -1 & 0 & 0 \\ 0 & 0 & 0 & 0 & 1 & 0 & -1 & 0 \\ 0 & 0 & 0 & 0 & \frac{L-g}{2} & 1 & \frac{-(L-g)}{2} & -1 \\ 0 & 0 & 0 & 0 & 0 & 0 & 1 & 0 \end{bmatrix} \begin{Bmatrix} C_1 \\ C_2 \\ D_1 \\ D_2 \\ G_1 \\ G_2 \\ H_1 \\ H_2 \end{Bmatrix} = \begin{Bmatrix} 0 \\ \frac{Fa^2}{4}\left[\frac{1}{(EI)_{bone}} - \frac{1}{(EI)_{plate,bone}}\right] \\ \frac{Fa^3}{12}\left[\frac{1}{(EI)_{bone}} - \frac{1}{(EI)_{plate,bone}}\right] \\ \frac{-Fb^2}{4(EI)_{plate,bone}} \\ \frac{-Fb^3}{6(EI)_{plate,bone}} \\ \frac{Fb(L-g)}{4}\left[\frac{1}{(EI)_{plate,bone}} - \frac{1}{(EI)_{plate,callus}}\right] \\ \frac{Fb(L-g)^2}{16}\left[\frac{1}{(EI)_{plate,bone}} - \frac{1}{(EI)_{plate,callus}}\right] \\ \frac{FbL}{4(EI)_{plate,callus}} \end{Bmatrix}$$

The preceding derivations were shown for plated fixation of the fracture site, as this model is more complex than intramedullary nailing due to centroids of the plate and bone being at different locations (nail and bone are assumed to be concentric cylinders). Modelling of IMN fracture fixation are identical to the above steps, with exception to the following:

The nail and cortical bone are collinear cylindrical sections; thus, parallel axis theorem is not necessary:

$$\bar{y}_{nail,bone} = 0 \qquad (C.28)$$

$$\bar{y}_{nail,callus} = 0 \qquad (C.29)$$

The bending rigidity of the bone-nail composite section is found from the combined rigidity of the nail and cortical sections. After performing area adjustments to the nail to account for differences in elastic modulus of the two sections, we obtain the following relationship:

$$\left(EI\right)_{nail,bone} = \frac{\pi E_{bone}}{64}\left\{\frac{E_{nail}}{E_{bone}} d_{nail}^4 + \left(d_o^4 - d_i^4\right)\right\} \qquad (C.30)$$

$$\left(EI\right)_{nail,callus} = \frac{\pi E_{callus}}{64}\left\{\frac{E_{nail}}{E_{callus}} d_{nail}^4 + d_o^4\right\} \qquad (C.31)$$

All other calculations follow the same procedure as the plated fracture model, yielding the following system of equations. Solving this system yields the integration constants necessary for predicting the maximum snail midspan deflection using the IMN equivalent of Equation C.19.

$$\begin{bmatrix} 0 & 1 & 0 & 0 & 0 & 0 & 0 & 0 \\ 1 & 0 & -1 & 0 & 0 & 0 & 0 & 0 \\ a & 1 & -a & -1 & 0 & 0 & 0 & 0 \\ 0 & 0 & 1 & 0 & -1 & 0 & 0 & 0 \\ 0 & 0 & b & 1 & -b & -1 & 0 & 0 \\ 0 & 0 & 0 & 0 & 1 & 0 & -1 & 0 \\ 0 & 0 & 0 & 0 & \frac{L-g}{2} & 1 & \frac{-(L-g)}{2} & -1 \\ 0 & 0 & 0 & 0 & 0 & 0 & 1 & 0 \end{bmatrix} \begin{Bmatrix} C_1 \\ C_2 \\ D_1 \\ D_2 \\ G_1 \\ G_2 \\ H_1 \\ H_2 \end{Bmatrix} = \begin{Bmatrix} 0 \\ \frac{Fa^2}{4}\left[\frac{1}{(EI)_{bone}} - \frac{1}{(EI)_{nail,bone}}\right] \\ \frac{Fa^3}{12}\left[\frac{1}{(EI)_{bone}} - \frac{1}{(EI)_{nail,bone}}\right] \\ \frac{-Fb^2}{4(EI)_{nail,bone}} \\ \frac{-Fb^3}{6(EI)_{nail,bone}} \\ \frac{Fb(L-g)}{4}\left[\frac{1}{(EI)_{nail,bone}} - \frac{1}{(EI)_{nail,callus}}\right] \\ \frac{Fb(L-g)^2}{16}\left[\frac{1}{(EI)_{nail,bone}} - \frac{1}{(EI)_{nail,callus}}\right] \\ \frac{FbL}{4(EI)_{nail,callus}} \end{Bmatrix}$$

APPENDIX D: NUMERICAL PREDICTIONS OF BENDING INDUCED IMPLANT DEFLECTIONS

D.1 Materials & Methods

Numerical predictions of maximum orthopaedic implant displacement during four-point bending were calculated to predict the effect of implant design and fracture size on implant deflections throughout the healing cascade, and serve as a means of validating the subsequent FE model. For these calculations, the fractured bone with orthopaedic fixation was modeled as a composite beam with three discrete and distinct bending rigidities along the composite's length due to differences in sectional areas and material properties (Figure C.1); model derivation is detailed in Appendix C.

Calculations were simplified by assuming the orthopaedic hardware (i.e. plate or IMN fixation) and metatarsal diaphysis to be bonded and to have simplified geometry: rectangular plate cross-section (13.5 x 4.5 x 120 mm; width x thickness x length), cylindrical IMN section (7 mm diameter), and hollow cylindrical bone (17 mm outer diameter, 10 mm inner diameter). The fracture callus was assumed to be of solid cylindrical geometry with a callus index of 1.0 (i.e., callus diameter equal to outer cortical diameter). The elastic moduli of the orthopaedic hardware (SS = 193 GPa or Ti = 110 GPa) and metatarsal (22 GPa [166]) were assumed to be isotropic. The bone-implant-callus assembly was assumed to be loaded in 4-point bending with a load magnitude (2 N-m maximum bending moment) and configuration equivalent to the in vivo DEC-loading fixture.

To capture temporal fracture healing for different osteotomy sizes, the orthopaedic implant maximum deflection was parametrically solved for a range of fracture gap heights relevant to the *in vivo* ovine fracture model (0 – 8 mm, in 1 mm increments) and callus elastic moduli (0.1 – 100% of cortical bone, in 0.1% increments). Implant design was parametrically modeled with regards to implant type (LCP or IMN), implant material (SS or Ti), and implant structure (second moment of area modified by +50%, +0%, and -50%).

D.2 Results

Predicted orthopaedic plate midspan displacements increased with increasing osteotomy height and decreasing callus elastic moduli. As callus elastic modulus increased from 0.01% to 100% of cortical bone (i.e., mechanical progression from initial fracture to completely healed states), predictions for all fracture heights converged to a common value, depending on the treatment permutation (Figure D.1). For all treatment permutations, initial plate displacement (callus elastic modulus of 0.01% of cortical bone) increased with increasing fracture height.

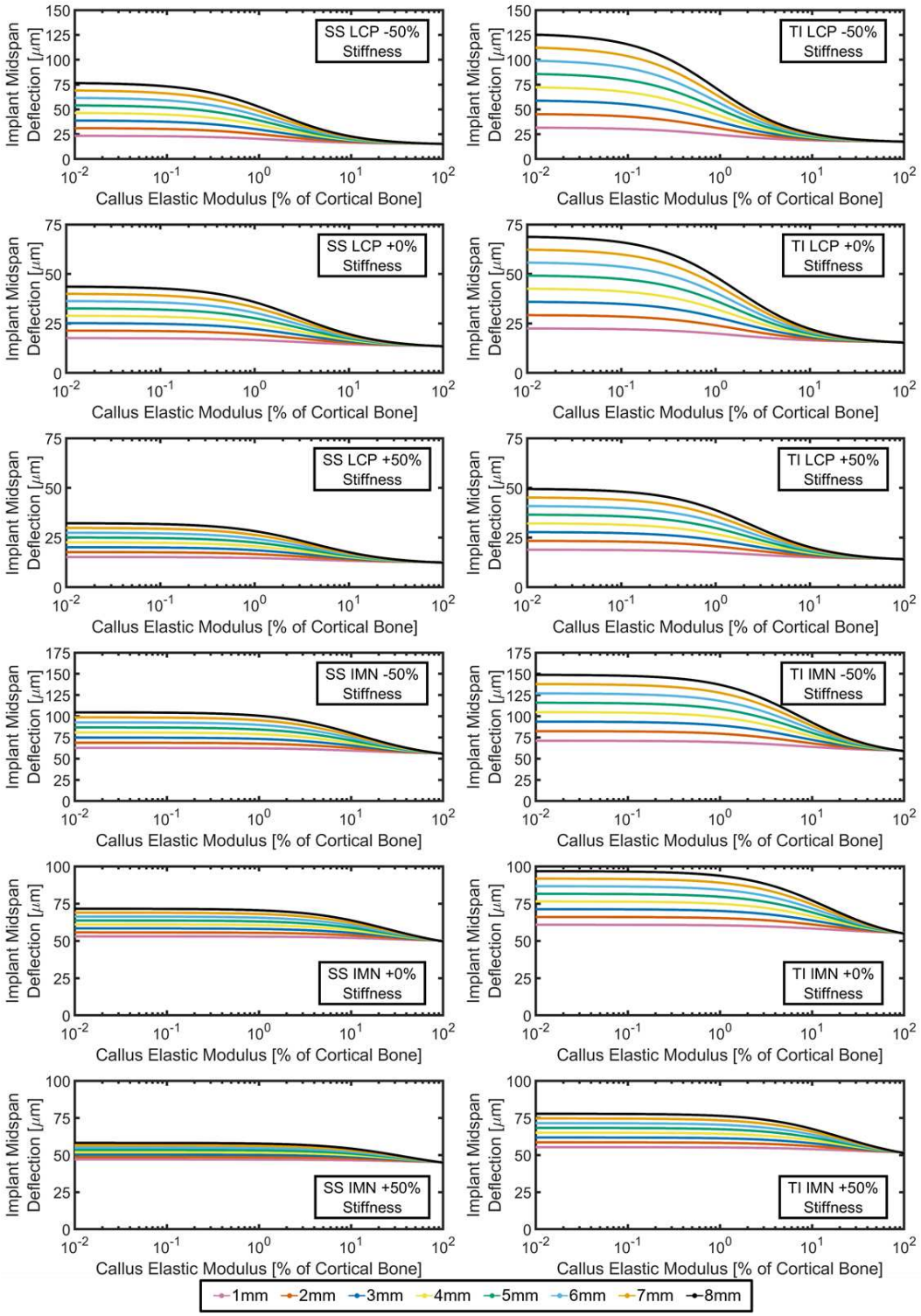

Figure D.1: Numerical prediction of maximum bending deflection of an ovine fractured metatarsal treated by orthopaedic plating when subjected to 2.0 N-m of four-point bending. Each chart corresponds to a unique permutation of fracture fixation type (i.e., SS or Ti implant material, LCP or IMN, & implant stiffness altered via modification to cross-sectional geometry). Colors correspond to results from different fracture heights.

D.3 Discussion

The numerical model presented in this study predicts initial fracture displacement to increase appreciably with fracture height (Figure D.1), however these results do not directly agree with FE predictions. Discrepancies in these two data sets can ostensibly be attributed to the assumption of perfect bonding between the bone and implant in the numerical model, which neglects the importance of screws / bolts for facilitating mechanical load transfer. These effects are present for both the LCP and IMN models, but is most easily visualized for the LCP scenario.

In order to improve angular stability, and mitigate the bone-plate contact forces associated with impedance of periosteal blood flow and callus formation, locking compression plating utilizes specialized screws to serve as the exclusive source of bone-implant load transfer resulting from the screws ability to lock into both the bone and LCP [167]. The absence of callus tissue at initial fracture precludes direct transfer of load between the two bone fragments, thus ensuring that load must be carried exclusively within the plate working length (i.e. the span between the first screw on each side of the fracture), with exception to cases where sufficient deformation facilitates direct contact of the bone fragments [148]. The assumption of perfect bone-plate bonding in the numerical model incorrectly allows the bone fragments within the working length to contribute to the structure, thus artificially reducing the implant working length, resulting in the prediction of decreasing initial plate displacement for decreasing fracture gap height. This assumption becomes less detrimental to the predicted results as the callus elastic modulus is increased.

The results of the numerical and FE models exhibit analogous trends after accounting for discrepancies in initial displacement predictions, with differences in predicted displacement magnitudes being reasonably attributable to the geometric and structural simplifications of the numerical model. Both models predict a highly non-linear relationship between callus elastic modulus and plate midspan deflection. The nonlinear relationship between bending induced implant displacements, as a function of callus elastic modulus, were present in both computational and FE models, and are characterized by three distinct phases:

Phase 1 – Low Callus Moduli ($E \approx 10^{-2}$ % - 10^{-1} %):

Implant displacements are relatively invariant to logarithmic increases to callus elastic modulus. This behavior results from the large disparity in the elastic modulus of the implant hardware relative to the callus tissues. The stiffness of the callus-implant composite is dominated by contributions from the implant; accordingly, changes in callus stiffness produce inconsequential changes to the overall stiffness of the composite.

Phase 2 – Intermediate Callus Moduli ($E \approx 10^{0}$ % - 10^{1} %, depending on treatment type):

Implant displacements decrease rapidly with logarithmic increases to callus elastic modulus. Behavior of implant deflection (δ), as a function of callus modulus (E) is highly reminiscent of the following function, were C_1 and C_2 represent arbitrary constants.

$$\delta(E) = \frac{C_1}{E} + C_2 \qquad (D.1)$$

For a uniform beam, maximum midspan deflection during symmetric four-point bending is calculated by the following equation, where I, F, L, and a correspond to the beam

section's second moment of area, applied bending load, beam length, and bending load spacing; respectively (Figure C.1).

$$\delta = \frac{1}{E} * \frac{Fa\left(3L^2 - 4a^2\right)}{24I} \qquad (D.2)$$

For the case of the healing fracture callus, E is the only non-constant parameter, thus Equation D.2 reduces to be equivalent to Equation D.1. Thus, it is evident that implant deflection and callus elastic modulus are inversely related in Phase 2, which suggests that callus elastic modulus has increased to the point where stiffness of the callus-implant composite is no longer dominated by contributions from the implant. Second moment of area for the callus section is substantially larger than that of the implant hardware, and therefore small increases in callus modulus produce large increases in stiffness; thus, Phase 2 can begin for callus elastic moduli far below that of the implant hardware.

Phase 3 – High Callus Moduli ($E \approx 10^2$ %):

Implant displacements converge to a constant value, despite continues logarithmic increases to callus elastic modulus. Equations D.1 and D.2 suggests that implant deflections within the callus region of the beam (i.e., within g of Figure C.1) will reduce to zero with increasing callus elastic modulus. Deflection contributions from regions away from the callus remain invariant and nonzero, thus midspan implant deflection values converge to a non-zero value as callus modulus increases.

The 3-phase pattern of implant deflections as a function of fracture healing have intriguing implications for the application of DEC diagnostic measurements. DEC measurements are best

suited to Phase 2, where changes in implant deflection are highly sensitive to small changes in callus elastic moduli, thus indicating healing. As implant stiffness is increased, increasing callus elastic modulus is required to overcome the implant's dominance of bending properties (i.e., the start of Phase 2 is shifted to higher callus elastic moduli). The practical implication is that meaningful DEC measurements cannot be made until later stages of healing when highly stiff implants are used.

These findings further imply callus dominates the composite's bending properties in Phase 3. Within a given treatment type (i.e., LCP or IMN), implant deflections for callus elastic modulus at full healing (callus modulus = 100% of cortical bone) were highly similar for all variations in implant stiffness / material, despite being highly varied at initial fracture (callus modulus = 0.01% of cortical bone, Figure D.2). Practically, this indicates that minimum implant deflections are primarily impacted by bone geometry, and secondarily impacted by fixation strategy (i.e., LCP vs IMN), but minimally affected implant design (i.e., material or structure). Minimum DEC resolution for viability in diagnostic application of a given fracture type can thus be known with confidence, regardless of the selected treatment hardware. However, it should be noted that total reduction in implant deflection, throughout the course of healing, is highly sensitive to implant design. Decreasing implant stiffness, through either structural or material choices, results in increases to the total implant deflection reduction (Figure D.2). As discussed previously, DEC is best suited for cases in which minor callus progression yield substantial reductions in implant deflections. Data from both FE and numerical studies therefore support the conclusion that DEC is best suited for cases in which fractures are not treated by highly rigid fixation hardware.

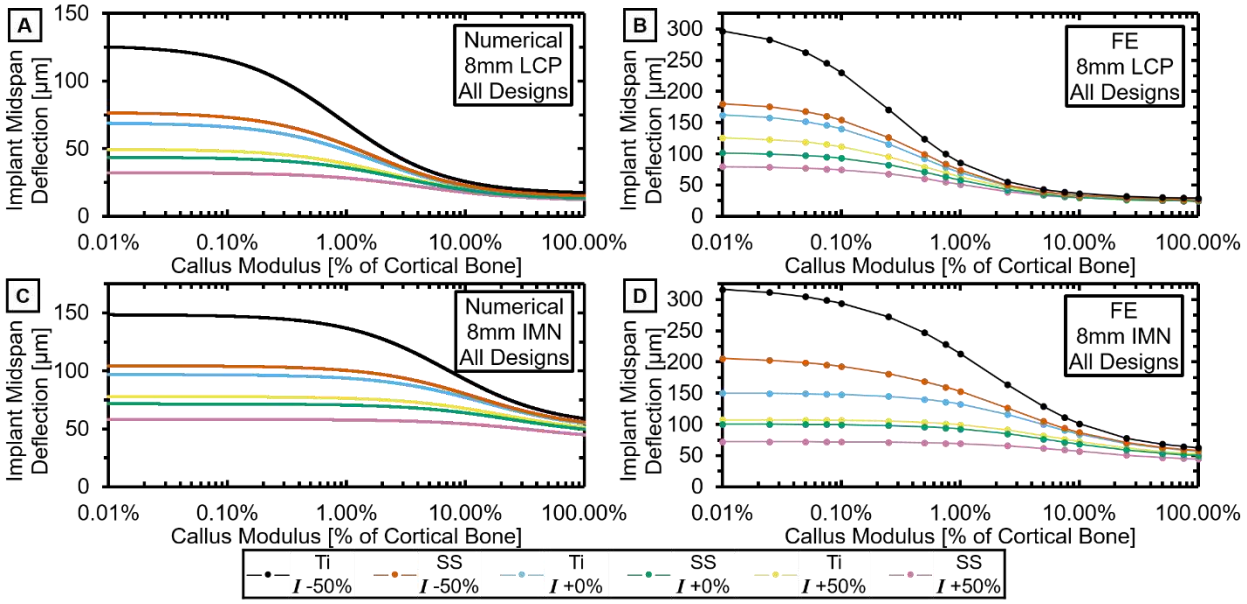

Figure D.2: Numerical and FE predictions of implant midspan deflection for an 8 mm metatarsal ostectomy fracture treated by LCP (A & B, respectively) or IMN (C & D, respectively) fixation. Simulation results are shown for all treatment permutations (i.e., Ti or SS implant material and altered implant structural stiffness).